OPTICALLY μ-PRINTED POLYMER MICROPHOTONIC SENSORS

WU JUSHUAI

PhD

The Hong Kong Polytechnic University

2018

The Hong Kong Polytechnic University

Department of Electrical Engineering

Optically μ-Printed Polymer Microphotonic Sensors

WU Jushuai

A thesis submitted in partial fulfillment of the requirements for the degree of Doctor of Philosophy

November 2017

CERTIFICATE OF ORIGINALITY

I hereby declare that this thesis is my own work and that, to the best of my knowledge and belief, it reproduces no material previously published or written, nor material that has been accepted for the award of any other degree or diploma, except where due acknowledgement has been made in the text.

_____ (Signed)

WU Jushuai (Name of student)

Abstract

With the advance of micro/nano fabrication technologies, microphotonic devices, such as optical microresonators and microinterferometers, have drawn intensive attention in various areas ranging from optical sensors to nonlinear optics. Although inorganic materials are widely used in microphotonic sensors, polymer materials attract more and more attention owing to their advantages including low cost, easy processability, mechanical and optical diversity, and biocompatibility. In this thesis, three kinds of polymer microphotonic devices were fabricated and systematically investigated for sensing applications.

Firstly, polymer optical whispering-gallery mode (WGM) resonators were fabricated by using an own-developed 3D μ-printing technology based on optical maskless exposure approach. Suspended-disk polymer WGM resonators with the radiuses of 230 and 160 μm were successfully fabricated. Optical fiber tapers with the minimum diameter of 2 μm were used to couple light into and out the polymer WGM resonators. The quality factor of the fabricated resonators was measured to be around 6×10^3. Numerical simulations using software COMSOL have been carried out to analyze the optical WGM resonators and compare with the measured results. The fabricated polymer WGM resonators are appealing for

refractive index sensing and biosensors.

Secondly, optical fiber-tip pressure sensors were fabricated by using an own-developed in situ μ-printing technology. SU-8 Fabry-Perot (FP) interferometers with sealed air cavities were fabricated on the end face of a standard optical fiber for development of pressure microsensors. SU-8 suspended diaphragms were directly printed by using a dynamic optical exposure technology and then were further constructed by a followed printing process to form sealed air cavities. Multi-beam FP interferometric fringes of reflection spectra were measured for pressure measurement. The sensing performance of the optical fiber-tip pressure microsensor was tested in the experiments. For a fiber-tip pressure sensor with the air cavity length of 93 μm and SU-8 diaphragm thickness of 11 μm, the measured pressure sensitivity was 2.93 nm/MPa. Numerical simulations of a 3D structural model have been performed by using commercial software COMSOL, and the simulated results agree well with the measured data.

Lastly, novel optical fiber-tip CO_2 sensors were developed by in-situ μ-printing of a functional polymer material, i.e. poly (1-allyl-3-vinylimidazolium bromide) (PAVB), on the end faces of single-core/multicore fibers to form micrometer scale FP interferometers. The PAVB FP interferometer can absorb CO_2 molecules, both physically and chemically, which results in an increase of the effective RI of PAVB polymer

and a red shift of the resonant wavelength in the reflection spectrum. As such FP interferometers are also sensitive to the temperature of the surrounding environment, another FP interferometer made of SU-8 was fabricated on the end face of the same fiber as a reference temperature sensor. The measured spectra were analyzed by using fast Fourier transformation to calculate the length of the polymer FP cavities. The fiber-tip CO_2 sensors show a linear response to the change of CO_2 concentration with the sensitivity of 34.92 pm/vol% in the range from 0 vol% to 75 vol%. The temperature sensitivity of the PAVB FP interferometer is 0.704 nm/°C, whose cross sensitivity effect can be compensated by the SU-8 FP interferometer with the temperature sensitivity of 0.059 nm/°C. The rise and fall times of the dynamic response of the fiber-tip CO_2 sensors were measured to be 6.1 and 8.0 min, respectively.

List of Publications

Journal papers:

1. **J. Wu**, X. Guo, A. P. Zhang, and H.-Y. Tam, "Rapid 3D μ-printing of polymer optical whispering-gallery mode resonators," *Optics Express* **23**, 29708-29714 (2015).
2. **J. Wu**, M.-j. Yin, K. Seefeldt, A. Dani, R. Guterman, J. Yuan, A. P. Zhang, and H.-Y. Tam, "In situ μ-printed optical fiber-tip CO 2 sensor using a photocrosslinkable poly (ionic liquid)," *Sensors and Actuators B: Chemical* **259**, 833-839 (2018).
3. **J. Wu**, M. Yao, F. Xiong, A. P. Zhang, H.-Y. Tam and P. K. A. Wai. " Optical fiber-tip Fabry-Pérot interferometric pressure sensor with an in-situ μ-printed air cavity " (accepted for publication in *Journal of Lightwave Technology*).
4. M. Yao, **J. Wu**, A. P. Zhang, H.-Y. Tam, and P. K. A. Wai, "Optically 3D μ-Printed Ferrule-Top Polymer Suspended-Mirror Devices," *IEEE Sensors Journal* **17,** 7257-7261 (2017).
5. X. Ouyang, K. Zhang, **J. Wu**, D. S.-H. Wong, Q. Feng, L. Bian, and A. P. Zhang, "Optical μ-Printing of Cellular-Scale Microscaffold Arrays for 3D Cell Culture," *Scientific Reports* **7**, 8880 (2017).
6. M. Yao, X. Ouyang, **J. Wu**, A.P. Zhang, H.-Y. Tam, and P. K. A. Wai, “Optical Fiber-Tip Sensors Based on In-Situ μ-Printed Polymer

Suspended-Microbeams," (accepted for publication in *Sensors*).

Conference papers:

1. **J. Wu**, X. Guo, A. P. Zhang, and H.-Y. Tam, "Rapid 3D micro-printing of optical whispering-gallery mode resonators," in *Nanotechnology (IEEE-NANO), 2015 IEEE 15th International Conference on*(IEEE, 2015), pp. 1271-1273.
2. **J. Wu**, M.-J. Yin, K. Taeuber, A. Dani, R. Guterman, J. Y. Yuan, A. P. Zhang, H.-Y. Tam. "Optical fiber-top microcavity sensor for CO_2 detection." In 2*017 TechConnect World Innovation Conference*, *2017*, *TechConnect*(TechConnect, 2017), pp.235-238.
3. M. Yao, P. Wai, **J. Wu**, A. P. Zhang, and H.-Y. Tam, "Optical 3D μ-printing of ferrule-top polymer suspended-mirror devices," in *SENSORS, 2016 IEEE*(IEEE, 2016), pp. 1-3.
4. M. Yao, **J. Wu**, A. P. Zhang, H.-Y. Tam, and P. Wai, "Optical fiber end-facet polymer suspended-mirror devices," in *Optical Fiber Sensors Conference (OFS), 2017 25th*(IEEE, 2017), pp. 1-4.
5. X. Ouyang, Z. Yin, **J. Wu**, A. P. Zhang, and C. Zhou, "Fabrication of Dual-Focus Microlens Array by Using Dynamic Optical Projection Stereolithography", submitted to *The 13th Pacific Rim Conference on Lasers and Electro-Optic (CLEO-PR 2018*), Hong Kong.

Acknowledgements

I would like to appreciate everyone who provided me with help during the pursuing of my Ph.D degree in the Hong Kong Polytechnic University.

First of all, I would like to express my sincerest gratitude to my chief supervisor, Dr. A. Ping Zhang, for his patient and kindly guidance. His profound knowledge and constructive suggestions help me a lot in my Ph.D period. And his passion, meticulosity and enthusiasm on research set me a good example and will influence me in the following days.

I also would like to thank Prof. Hwa-yaw Tam, my co-supervisor, for providing me with the first-class equipment and environment to do research. I am grateful for his suggestive advice and efforts on revising my writings.

I wish to thank Dr. Mingjie Yin for his help in material preparation, experiment design and data processing. I am very grateful to Dr. Xin Guo and Dr. Shaorui Gao for their support in the setup of experimental platform and optical design. Besides I appreciate Dr. Zhengyong Liu, Dr. Bin Zhou, Dr. Yangxi Zhang, Miss. Yaxi Yan, Mr. Mian Yao, Mr. Xia Ouyang, Mr. Feng Xiong, Mr. Gang Yang, Mr. Xin Cheng, Mr. Julien Bonefacino, Mr. Bobo Huang and Mr. Tianhao Yuan for their help and useful discussions on my experiments.

I wish to acknowledge Dr. Ming-Leung Vincent Tse, Dr. Chi-Fung Jeff Pun and Dr. Shun-Yee Michael Liu for their kindly technical help. I also

wish to express my gratitude to everyone in the Photonics Research Centre and my friends in Hong Kong for their help in my study and life. I really appreciate the four-year wonderful life in Hong Kong, and it will be a great treasure in my life.

Finally, I want to express my gratitude to my parents and my elder sister, for their unselfish dedication and support. This thesis is dedicated to them to express my deepest love and gratitude!

Table of Contents

Pages

Chapter 4

Chapter 5

List of Figures

List of Tables

List of Acronyms

Acronyms	Description
AFM	Atomic force microscope
ASE	Amplified spontaneous emission
BiMW	Bimodal waveguide interferometer
CCD	Charge-coupled device
DMD	Digital-micromirror device
FBG	Fiber Bragg grating
FEM	Finite element method
FFT	Fast Fourier transformation
FP	Fabry–Pérot
FPI	Fabry–Pérot interferometer
FSR	Free spectral range
FWHM	Full width at half maximum
LCD	Liquid crystal display
LOD	Limit of detection
LPG	Long period grating
MEMS	Microelectromechanical systems

MZI	Mach-Zehnder interferometer
NA	Numerical aperture
OMsL	Optical maskless stereolithography
OPPI	Octoxyphenylphenyliodonium hexafluoroantimonate
OSA	Optical spectrum analyzer
PGMEA	Propyleneglycol monomethylether acetate
PIL	Poly(ionic fluid)
PAVB	Poly(1-allyl-3-vinylimidazolium bromide)
PDMS	Polydimethylsiloxane
PMMA	Polymethyl methacrylate
QED	Quantum electrodynamics
RI	Refractive index
RIU	Refractive index units
SEM	Scanning electron microscope
SLM	Spatial light modulator
SMF	Single mode fiber
SOI	Silicon on insulator
SWCNT	Single-walled carbon nanotube
TBA	Tributylamine
WGM	Whispering-gallery mode
ZPAL	Zone-plate-array photolithography

Chapter 1

Introduction

1.1 Background

Photonics has become one of essential technologies in our daily life and has been widely used for lighting, projectors and smartphones. Microphotonics is the science and technology exploiting photonics on micrometer scale. With the emergence of novel micro/nano fabrication technologies, microphotonic devices, such as optical waveguides [4, 5], microresonators [6], gratings and interferometers [7-9], have been intensively investigated in the areas of nonlinear optics [10], low-threshold lasers and dynamic filters [11]. Especially, owing to the small size and high energy density in microphotonic devices, microphotonic technologies are very appealing for high-sensitivity sensing [12-17].

Sensors are devices for acquiring quantitative information such as pressure, temperature, and force from a target position or object. In recent years, microphotonic sensors have drawn a lot of attention owing to their small size and high sensitivity. For instances, different kinds of optical microcavities have been demonstrated as high-performance microphotonic

sensors. When the geometric parameters or optical properties of an optical microcavity are changed, the variation will be transferred to a change of the optical responses of the microcavity, for example, a shift of its resonant wavelength.

In addition to optical microcavities, fiber-based devices are another remarkable kind of microphotonic sensors. With the advantages of optical fibers, such as small size, biocompatibility, distributed detection capabilities and low cost, many kinds of photonic sensors including fiber Bragg gratings, long-period gratings, thin-core-fiber modal interferometers, and fiber-based Fabry-Pérot cavities have been used to develop temperature, pressure, refractive index and even chemical and biological sensors. A number of reviews can be found regarding to the fields of fiber optic biosensors [18, 19].

To fabricate microphotonic sensors, different kinds of microfabrication technologies have been established. In particular, in order to overcome the limitations of conventional photomask-based photolithography, whose fabrication cost is usually high and lead time is commonly long, more and more maskless exposure technologies have been developed to fabricate microphotonic sensors. Typical maskless lithography technologies mainly include two kinds: (1) charged particles based maskless exposure technologies, such as focused ion beam and electron

beam lithography; (2) optical maskless exposure techniques, such as digital photolithography based on spatial light modulators (SLM), interference lithography and two-photon polymerization technology. Maskless exposure technologies have been widely used in the fields of microoptics, microelectromechanical systems and printed circuit boards.

The materials of microphotonic devices can be divided into two catalogues, inorganic materials and organic materials. Although inorganic materials have been widely used in the fabrication of microphotonic sensors, polymer materials, a major part of organic materials, attracted great attention in recent years. Compared to the inorganic counterparts, polymers exhibit many advantages such as low cost, mechanical and optical diversity, easy processibility, biocompatibility and functionality, which make them very promising for microphotonic sensors.

1.2 Motivations and Contributions of Research

Though microphotonic sensors have been intensively investigated in the past decades, most of them are made of inorganic materials and the fabrication process is relative complex and time-consuming. By using maskless exposure technology, novel polymer microphotonic sensors can be developed. In particular, specialized types of microphotonic sensors can be developed using different kinds of responsive polymers for emerging

chemical and biological sensing as well as multi-parameter and remote sensing applications.

In this thesis, three different kinds of polymer microphotonic sensors are developed by using the own-established optical μ-printing technologies based on maskless exposure approaches. Firstly, polymer whispering gallery mode resonators were demonstrated by using a novel optical maskless exposure technology, called optical 3D μ-printing. Secondly, polymer Fabry-Pérot interferometers with sealed air cavities were in situ μ-printed on the end face of a single-mode optical fiber for pressure sensing. The fabricated miniature fiber-based pressure sensors showed high sensitivity and fast dynamic response. Lastly, a functional polymer material with selective CO_2 sorption ability was in situ μ-printed on the end face of a multi-core optical fiber to achieve fiber-top multisensory integration for simultaneous measurement of temperature and CO_2 concentration. The fabricated sensors showed a linear response to the change of CO_2 concentration in the range of 0 vol% to 75 vol%.

1.3 Outline of Thesis

The chapters of the thesis are organized as below:

Chapter 1: Introduction. In this chapter, the background of microphotonic sensors is reviewed. The objectives of the research project

are described, and the outline of the thesis is presented.

Chapter 2: Overview of polymer microphotonic sensors. In this chapter, different kinds of polymer microphotonic sensors including free-standing polymer whispering-gallery-mode resonator sensors, fiber-based polymer microphotonic sensors, and waveguide-based polymer microphotonic sensors are summarized. The sensing mechanisms and structures of polymer microphotonic sensors are discussed.

Chapter 3: Optical μ-printing based on maskless exposure technology. In this chapter, optical μ-printing technologies using DMD-based maskless exposure approach are introduced. The components of the system including light source, DMD chip, illumination optics and projection optics and the imaging analysis of the projection optics are discussed in detail.

Chapter 4: Optically 3D μ-printed polymer whispering-gallery-mode resonators. In this chapter, polymer optical whispering-gallery mode resonators fabricated by an own-developed optical 3D μ-printing technology are presented. The fabrication and characterization of polymer whispering-gallery mode resonators are described and compared with numerical simulation results.

Chapter 5: Optical fiber-tip pressure sensors with in situ μ-printed air cavities. In this chapter, polymer Fabry-Pérot interferometer pressure sensors fabricated by an own-developed optical in situ μ-printing

technology are presented. The design and fabrication of the polymer Fabry-Pérot interferometer pressure sensors are described in detail. Finally, the simulation results using COMSOL software are provided to compare with experimental results.

Chapter 6: Optical fiber-tip CO_2 sensors using a photocrosslinkable poly(ionic liquid). In the chapter, optical fiber-tip carbon dioxide sensors are presented using polymer Fabry-Pérot interferometers. The fabrication process and testing of the optical fiber-tip carbon dioxide sensors are described at length. The working mechanism of the sensor and the solution to compensate its cross sensitivity to temperature are presented.

Chapter 7: Conclusions and future outlook. In this chapter, a summary of the research results is presented and future outlook of the project is discussed.

Chapter 2

Overview of Polymer Microphotonic Sensors

2.1 Introduction

With the advance of micro/nano fabrication technologies, different kinds of polymer microphotonic sensors have been developed. Typical polymer microphotonic sensors include free-standing polymer whispering-gallery-mode (WGM) resonator sensors, fiber-based polymer microphotonic sensors, and waveguide-based polymer microphotonic sensors.

2.2 Free-standing polymer WGM resonator sensors

2.2.1 Fundamentals of WGM resonators

Whispering gallery modes (WGMs) are a kind of resonance caused by total internal reflection around the boundary of a circular interface [20-23]. When the light propagating along the inner surface of the resonator is in phase after each trip, it will generate a constructive interference and thus form resonant features. The spectral properties and linewidth of the resonance are determined by the geometries of the resonators and the

refractive index (RI) of the resonators and surrounding media. By virtue of low loss and small mode volume, optical WGM resonators can gain ultrahigh quality factor and high optical density. All these properties make WGM resonators an optimum platform to delve into the world of advanced photonics from low-threshold lasing, nonlinear optics to cavity optomechanics.

WGMs were first proposed by Lord Rayleigh in 1910-1912 and studied in acoustic phenomena in St. Paul's Cathedral. As shown in **Figure 2.1(a)**, a whisper can be heard anywhere along the border of the round room in St. Paul's Cathedral. The acoustic wave propagates along a thin layer near the curved wall by repeated reflection, which results in the whispering gallery phenomenon. Similar propagation modes also exist in the optical domain. Richtmyer demonstrated that microspheres could support optical WGMs in 1939 [24]. Since then, various structures have been developed to sustain optical WGMs, such as microspheres, microcapillaries, microtoroids, optical fibers, microbottles and microbubbles (as shown in **Figures 2.1(b)–(g)**).

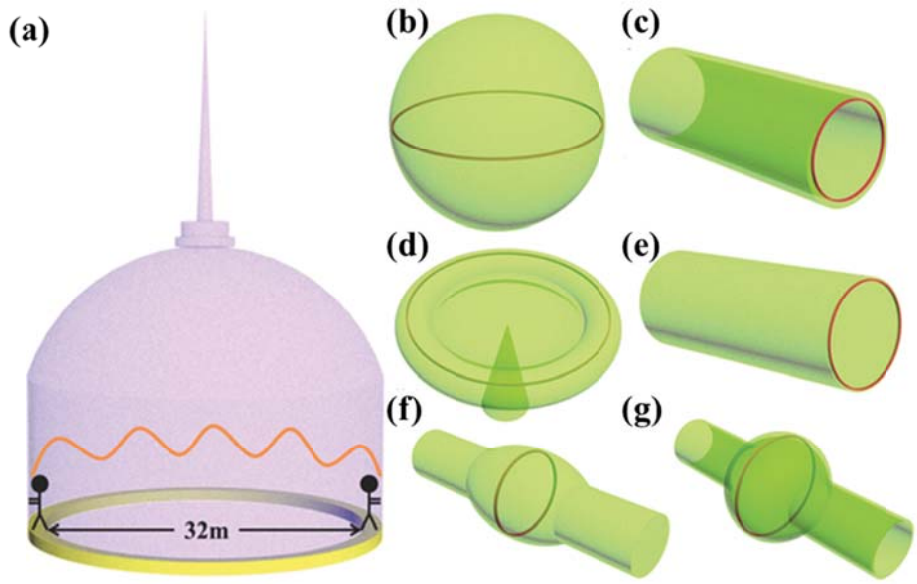

Figure 2.1 (a) Schematic illustration of the dome of the St. Paul's Cathedral in London. WGM resonators of different geometries including (b) microsphere, (c) microcapillary, (d) microtoroid, (e) optical fiber, (f) microbottle and (g) microbubble. The red line indicates the main optical path in the resonator. Adapted from Ref [23].

The mostly studied WGM resonators are made of glass material [25-27]. However, the glass WGM resonators are hard to be further mixed with other functional materials, which thus limit their applications in sensor development. So glass WGM resonators coated with sensing polymer or even polymer WGM resonators are deeply investigated to explore different kinds of microphotonic sensors [28-30]. Compared with the glass counterparts, polymer WGM resonators have the advantages of easy processibility, diversity in physical and chemical properties, low cost and biocompatibility.

2.2.2 Sensing principles

In general, the operating principles of the WGM sensors are to monitor the spectral response of the WGM resonators with respect to physical stimuli from surrounding environment.

a) Frequency shifts

Shift of the resonant frequency is the mostly applied demodulation method in WGM resonators, which might be caused by the change of the RI of the surrounding medium as well as the change of the RI and the size of the resonator. This relation can be expressed by [31]

$$\frac{\Delta\lambda}{\lambda_0}=\frac{\Delta n_h}{n_h}F+\frac{\Delta n_r}{n_r}(1-F)+\frac{\Delta R}{R}, \tag{2.1}$$

where F is a sensitivity function indicating the gradient of the phase jump upon reflection at the resonator surface, n_r and n_h are the refractive indices of the WGM resonator and host medium, respectively, and R is the radius of the WGM resonator. Refractometers, a basic type of WGM resonators based polymer microphotonic sensors, directly monitor the changes in the bulk RI of the surrounding medium. According to Ref. [32], smaller resonators and lower RI contrast between the resonators and the surrounding medium can result in high RI sensitivity. Substantially, this phenomenon results from the further extending of the evanescent wave of the WGM resonators to the surrounding medium, which will increase the

influence of the surrounding medium in determining the effective RI and resonant wavelength of the WGM resonators.

b) Line broadening

The adhesion of small particles or analytes on a WGM cavity can also induce changes in the linewidth of the resonance, resulting degradation of the Q factors of the WGM resonators. In the perturbation process, additional scattering and absorption losses will be introduced. The change in resonant linewidth caused by additional absorption losses of a bound nanoparticle can be expressed as [33]

$$\frac{\delta\gamma_{abs}}{\omega_0} \approx \mathrm{Im}[\alpha]\frac{|\mathbf{E}(\mathbf{r}_p)|^2}{\int_V \varepsilon(\mathbf{r})\,|\,\mathbf{E}(\mathbf{r})\,|^2\,d\mathbf{r}}, \tag{2.2}$$

where V and $\mathbf{E}$ are the volume of the all space and the unperturbed mode distribution, respectively. $\varepsilon(\mathbf{r})$ and α denote the original permittivity distribution and the polarizability of the particle, respectively. Meanwhile the change of resonant linewidth induced by scattering losses of nanoparticles can be solved using a rigorous operator method [34].

c) **Multi-peak sensing**

The sensing principles described above only consider the changes of single resonant property using one WGM resonator. Recently many techniques have been studied to combine different sensing channels or using multiple WGMs. For instance, owing to its self-reference ability, the frequency

splitting between two coupled WGMs can be used to detect nanoparticles whose radiuses are down to tens of nanometers[35]. When the relative mode splitting induced by single or multiple nanoparticles bound to the WGM cavity is stronger than the WGM's associated decay rate, a spectral doublet is formed.

2.2.3 Applications of polymer WGM resonator sensors

Polymer WGM resonators have been widely used as platforms for sensing applications. For instance, Dong *et al*. fabricated a temperature sensor by using PDMS microspherical resonators, exhibiting a sensitivity of 0.245 nm K^{-1} [36], which is larger by one order of magnitude than WGM resonators made of pure silica. Wagner *et al.* demonstrated a force sensor with a force sensitivity of 7.664 nm N^{-1} by using a hollow polymethyl methacrylate (PMMA) sphere, with a resolution of $\sim 10^{-5}$ N [37]. Moreover, various biosensors were demonstrated through further functionalizing polymer WGM resonators. More details can be found in Ref. [29, 38-40].

2.3 Fiber-based polymer microphotonic sensors

Owing to the ultralow loss, high capacity and small size, optical fibers have become a promising platform for optical sensing, where light can be easily coupled and transmitted. Typical polymer microphotonic sensors based on fiber technology include polymer micro/nano-fiber sensors and optical

fiber-tip sensors.

2.3.1 Polymer micro/nano-fiber sensors

Polymer micro/nano-fibers usually have diameters ranging from hundreds of nanometers to several micrometers, which can be fabricated by drawing polymer materials at high temperature [41, 42]. Owing to their low optical loss, small size, excellent mechanical flexibility and large ratio of evanescent filed in surrounding medium, polymer micro/nano-fibers are an ideal component to develop high-sensitivity, low-power-consumption and fast-response sensors.

Various kinds of micro/nano-fiber devices can be adopted for sensing applications, such as straight micro/nanofibers, micro/nanofiber gratings, micro/nano-fiber circular cavities. What's more, some functional dopants including quantum dots, dye molecules and metal nanoparticles can be doped into polymer micro/nano-fibers for biochemical and gas sensing [43-46]. In 2008, Gu *et al*. presented a NH_3 sensor with a detection limit of 3 ppm by doping bromothymol blue in poly (methyl methacrylate) micro/nano-fibers [46]. In 2012, Wang *et al*. demonstrated a humidity sensor with low power consumption and fast response through doping gold nanorods into polyacrylamide micro/nano-fibers [47].

2.3.2 Fiber-tip polymer Fabry-Pérot interferometer (FPI) sensors

Because of the tiny size and inherent light collection ability, optical fiber-tip sensors have drawn great attentions recently. In this thesis, we focus on the fiber-tip polymer FPI sensors and their applications.

2.3.2.1 Basic principle

FPIs consist of two reflective surfaces, which can be an optical fiber end face or an elastic diaphragm. The reflected lights interfere after reflections and form interference pattern in the reflection or transmission spectra, as shown in **Figure 2.2.** The total reflection intensity can be expressed as [48]:

$$P_R = P_I \frac{R_1 + R_2\eta - 2\sqrt{R_1 R_2 \eta}\cos(\frac{4\pi nL}{\lambda} + \varphi_0)}{1 + R_1 R_2 \eta - 2\sqrt{R_1 R_2 \eta}\cos(\frac{4\pi nL}{\lambda} + \varphi_0)}, \tag{2.3}$$

where P_R and P_1 are the intensity of the incident and reflected light, respectively, $R_1$and R_2 are the reflectivities of the two reflective surfaces, respectively, n is the RI of the interferometer, L is the length of the interferometer, η is the transmission coefficient of the light traveling forth and back through the interferometer, and φ_0 is a constant phase shift term.

The shape of the reflection or transmission spectra of FPIs is determined by a finesse factor defined as:

$$F = \frac{\pi\sqrt[4]{R_1 R_2}}{1 - \sqrt{R_1 R_2}}, \tag{2.4}$$

where R_1 and R_2 are the reflectivities of the two reflective surfaces.

Assuming there is no transmission loss when light traveling within the cavity (i.e. η=1) and the reflectivities of the two reflective surfaces are the same (R_1=R_2=R), the reflection spectra of the FPIs with different reflectivities are depicted in **Figure 2.3**.

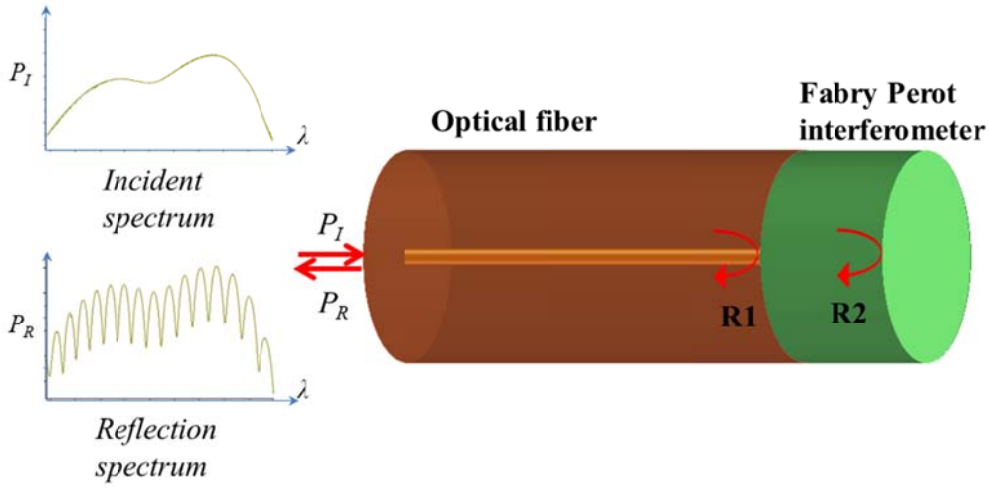

Figure 2.2 Schematic of a fiber-tip Fabry-Pérot interferometer (FPI).

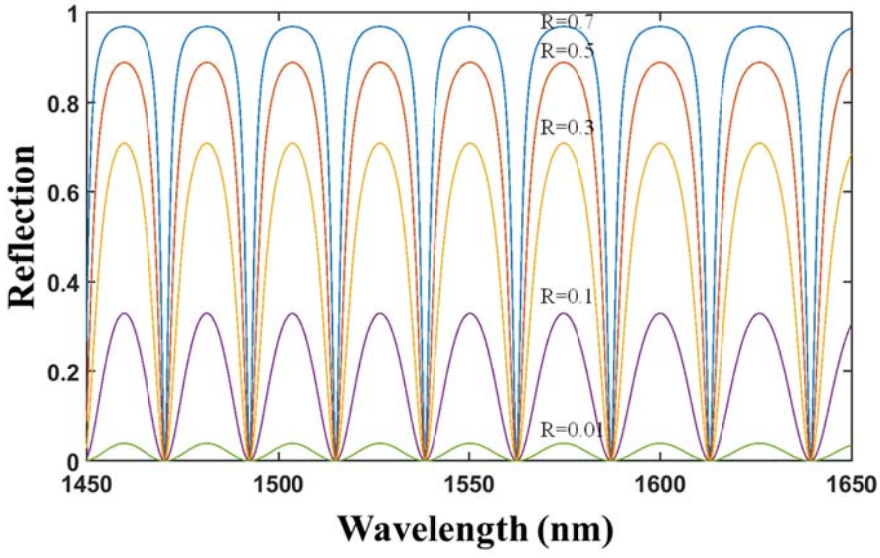

Figure 2.3 Simulated reflection spectra of the FPIs with different reflectivities (R_1=R_2=R). Assuming the cavity length L=50 μm, the refractive index of the cavity n=1.

From Equation 2.4 and Figure 2.3, it can be seen that a higher reflectivity of the reflective surfaces leads to a higher finesse F and a steeper slope of the interference fringes in the reflection spectrum. For FPIs with lower values of R_1 and R_2, the high-order reflected light of each reflective surface can be ignored and then the intensity of the total reflected light can be simplified as a two wave interference spectrum as:

$$P_R \approx P_I \left[R_1 + R_2\eta - 2\sqrt{R_1 R_2 \eta}\cos(\frac{4\pi nL}{\lambda} + \varphi_0) \right]. \quad (2.5)$$

The reflection spectrum of such FPIs, which are often called as low-finesse FPIs, exhibits a simple sinusoidal curve.

If the FPIs are fabricated on the end face of optical fibers, one can obtain a micrometer scale interferometer device for sensing, called optical fiber-tip FPI sensor. For instance, Arregui *et al*. presented a polymer FPI on the end face of an optical fiber by the ionic self-assembly method in 1999 [49]. Thereafter, Li *et al*. demonstrated a fiber-tip SU-8 FPI temperature sensor by the dip-coating method in 2014 [50]. The reflection or transmission spectra of the fiber-tip polymer FPI sensors depend on cavity lengths of the FPIs, so any stimulus that changes the cavity length will be detected in the reflection or transmission spectrum.

2.3.2.2 Signal demodulation methods

Although signal demodulation methods of FPIs can be generally divided

into spectrum-based and intensity-based demodulation approaches, we put our focus on the review of spectrum-based demodulation method in the section.

a) Peak/valley-tracking method

In this method, the shift of the peak/valley wavelength in the reflection spectrum is employed to monitor the phase change in Equation 2.5, which is $\varphi=4\pi nl/\lambda+\varphi_0$. For the peak wavelength in the reflection spectrum, it should satisfy the condition

$$\frac{4\pi nL}{\lambda_m}+\varphi_0=2m\pi+\pi,(\mathrm{m}=1,2,3...) \tag{2.6}$$

where λ_m is the peak wavelength and m is the order of the interference. Using the shift of the peak wavelength $\Delta\lambda_m$, the change of the cavity length (ΔL) can be calculated as:

$$\Delta L=\frac{\Delta\lambda_m}{\lambda_m}L. \tag{2.7}$$

Though peak/valley-tracking method can achieve high resolution, the absolute value of the cavity length cannot be determined by this method. Besides, the detection range of this method is limited by the free spectral range of the reflection spectrum.

b) Two adjacent peaks/valleys method

The cavity length of the FPIs can be determined by using two adjacent peak or valley wavelengths in the reflection spectrum. If λ_m and λ_{m+1} are used to

denote two adjacent peak wavelengths in the refection spectrum, they satisfy

$$\begin{aligned} \frac{4\pi nL}{\lambda_m} + \varphi_0 &= 2m\pi + \pi \\ \frac{4\pi nL}{\lambda_{m+1}} + \varphi_0 &= 2(m+1)\pi + \pi, (\mathrm{m} = 1, 2, 3...). \end{aligned} \tag{2.8}$$

Then, the cavity length can be deduced as,

$$L = \frac{\lambda_m \lambda_{m+1}}{2n(\lambda_{m+1} - \lambda_m)}. \tag{2.9}$$

If the wavelength spacing between two adjacent peaks or valleys is much smaller than the absolute values of the peak or valley wavelengths, Equation 2.9 can be expressed as,

$$L = \frac{\lambda_m^2}{2nFSR}. \tag{2.10}$$

where FSR is the free spectral range of the reflection spectrum around λ_m. The traceable resolution of the change of cavity length can be expressed as,

$$\frac{\Delta L}{L} = \frac{\sqrt{2}\lambda_{m+1}}{\lambda_m - \lambda_{m+1}} \cdot \frac{\Delta\lambda_m}{\lambda_m}. \tag{2.11}$$

Compared with peak/valley-tracking method, the relative error is magnified by $1.414\lambda_m/(\lambda_m-\lambda_{m+1})$ times.

c) Fourier transform method

Equation 2.5 can be rewrite as,

$$P_R \approx P_I\left[R_1 + R_2\eta - 2\sqrt{R_1 R_2 \eta}\cos(4\pi nkL + \varphi_0)\right]. \quad (2.12)$$

where the intensity of the reflected light is a cosine function of the wavenumber k=1/λ. The period of the cosine function depends on the cavity length L, which can be obtained from the peak position in "frequency" domain by taking Fourier transform [51]. Theoretically, Fourier transform method is an absolute and wide-range method. However, owing to the limitations of the spectral width of the light source and the spectral range and resolution of optical spectrum analyzer, the resolution of Fourier transform method is usually not high. The resolution of Fourier transform method for spectrum demodulation can be approximated as

$$\delta L \propto \frac{1}{\lambda_0 - \lambda_1} \quad (2.13)$$

where λ_0 and λ_1 are the starting and stop wavelengths of the light source. In addition to the above mentioned methods, curve fitting method and a combination of the methods mentioned above are widely adopted.

2.3.2.3 Applications

Fiber-tip polymer Fabry-Pérot sensors can be applied in different areas such as pressure, temperature, humidity, pH, RI, and numerous kinds of gases sensing. In 1996, Beard et al. fabricated a polymer FPI using a slim transparent polymer film for ultrasound sensing [52]. It is noteworthy that they used a sealed water cavity to improve the fringe visibility of the

interference pattern. Ionic self-assembly technology was also proposed by Arregui *et al* to fabricate polymer FPI on fiber end for humidity sensing in 1999 [49]. With the advance of micro/nano fabrication technology, polymer FPI can be fabricated separately and then integrated with optical fiber. In 2007, Hill *et al*. presented a pressure sensor by fabricating an SU-8 cap and then assembled it on the end face of an optical fiber [53]. The fabricated device showed a linear response in the range of 0 to 125 mmHg with a resolution of 1~2 mmHg. In addition, Chen *et al*. developed a method to fabricate fiber-tip polymer FPI pressure sensor. A fiber-end air cavity was formed by wet etching process, and then UV adhesive (Norland, NOA68) was dipped and cured on the fiber end face to form a miniature FPI sensor [54]. The sensor showed a pressure sensitivity of −40.94 nm MPa^{-1}.

2.4 Polymer waveguide-based microphotonic sensors

Another typical kind of microphotonic sensors is optical waveguide devices. In this section, two kinds of polymer waveguide-based microphotonic sensors, including polymer waveguide-based microring-resonator sensors and polymer waveguide-baser interferometer sensors, are discussed.

2.4.1 Polymer waveguide-based microring-resonator sensors

A waveguide-based microring resonator is composed of an input/output bus waveguide and a microring (with a typical 1-μm gap away from the bus

waveguide), as shown in **Figure 2.4**. Light wave of the bus waveguide will be evanescently coupled to the microring and then propagates along the ring. If the phase change of the light propagating one trip along the ring is multiple times of 2π, a constructive interference occurs in the form of WGM. The resonance wavelength λ satisfies the condition

$$\lambda = 2\pi r \frac{n_{eff}}{m}, \tag{2.14}$$

where r and n_{eff} are the radius and the effective RI of WGM, respectively, and m is an integer number. The resonant wavelength of the WMG shows as a dip in the transmission spectrum. If there is an induced change in the effective RI of the WGM, the resonant wavelength will shift according to Equation 2.14, which can be used as a RI sensor or biochemical sensor.

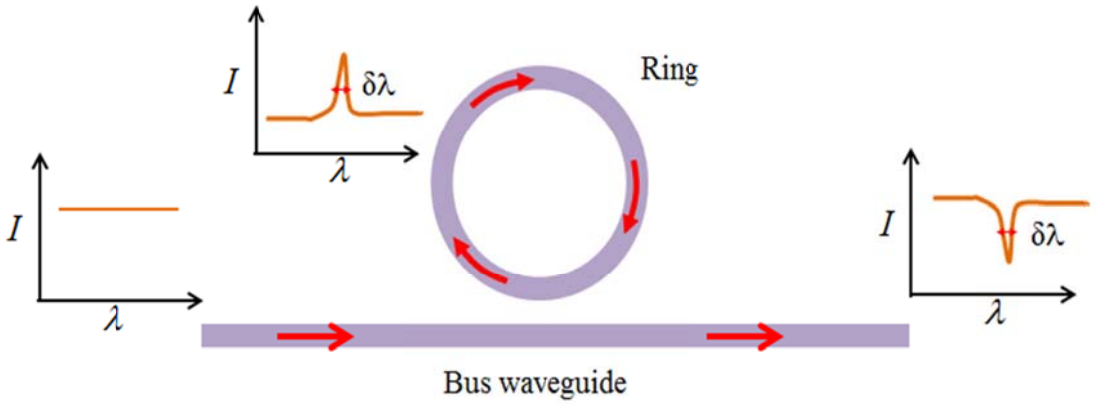

Figure 2.4 Working principle of polymer waveguide-based microring-resonator sensors.

The light-matter interaction length of waveguide-based microring-resonator sensors can be much longer than the physical perimeter

of microrings. The effective interaction length L_{eff} of the microring resonator can be expressed by:

$$L_{eff} = Q\frac{\lambda}{2\pi n_{eff}}, \tag{2.15}$$

The Q factor depends on the optical loss of the resonator and describes the lifetime of the photon existing in the resonator. Typical Q factors of microring resonators range from 10^3 to 10^8.

Polymer microring resonators have drawn a lot attention in RI and biosensing applications recently. In 2006, Chao *et al.* fabricated polystyrene microring resonator sensors, whose RI detection limit is 10^{-7} refractive index unit (RIU) and a biomolecular detection limit is ~250 pg mm^{-2} (detecting streptavidin molecules) [55]. In 2012, using a thermal reflow process, Wang *et al.* demonstrated a polymer microring resonator with a Q factor of 5×10^4, and achieved a bulk RI sensitivity of 49.75 nm/RIU, which was comparable with the silicon-on-insulator based microring resonators [56]. Owing to the advantages of low cost and easy fabrication, polymer microring resonators are very promising in vast applications, such as disease diagnosis, environment monitoring, and food safety control.

2.4.2 Polymer waveguide-based interferometer sensors

2.4.2.1 Integrated Mach-Zehnder interferometer sensors

As shown in **Figure 2.5(a),** an integrated Mach-Zehnder interferometer

(MZI) usually consists of an input waveguide, two Y branches, two arms, and an output waveguide. The coherent light from a laser source enters the input waveguide and equally splits at the Y branch. The sensing arm with a window allows the evanescent optical field to interact with the measurand, which induces a phase change of the light wave, while the reference arm is isolated by a cladding layer. Interference appears when the light waves from the two arms recombine at the output waveguide. In order to depress multimode and cross-polarization interference, single-mode and single-polarization waveguides are typically used in MZI-based sensors.

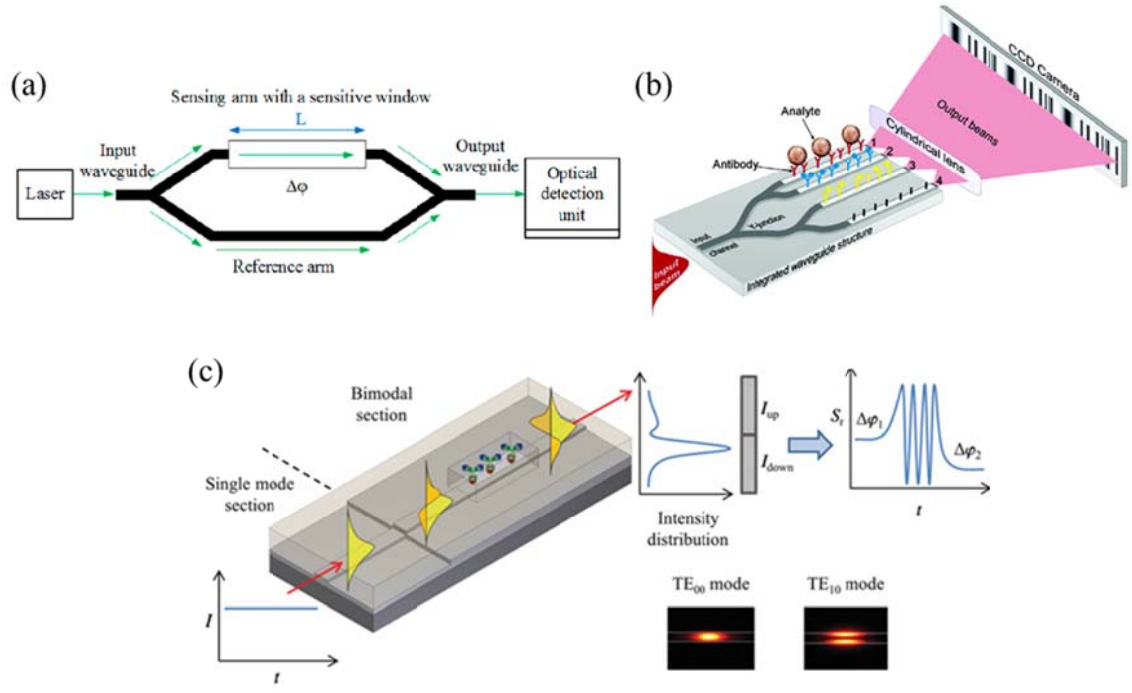

Figure 2.5 Schematic illustrations of: (a) integrated Mach-Zehnder interferometer sensor, (b) integrated Young's interferometer sensor, (c) bimodal waveguide interferometer sensor. Adapted from Ref. [1-3]

It is known that the optical intensity at the output can be expressed as:

$$I_T = I_S + I_R + 2\sqrt{I_S I_R}\cos\Delta\varphi, \quad (2.16)$$

where I_S and I_R are the intensity of the optical modes in the sensing and reference arms of the MZI, respectively, and $\Delta\varphi$ is the phase difference between the light waves travelling in sensing and reference arm. So the phase difference caused by the change of the RI surrounding the sensing arm will result in a variation of the optical intensity detected by the photo detector in the output port. In general, increasing the length of the sensing arm will enlarge the sense signal. However, due to the nature of the cosine function of the output intensity, an integrated MZI sensor has limited linear response range, which is a common disadvantage of MZI-based sensors.

Owing to the advantages of easy processibility, biocompatibility and versatility, polymer MZIs have attracted much attention in the past decades. Although polymer MZI was first proposed by Girton *et al.* in 1991 [57], it was not until 2005 when Shew *et al.* presented the first integrated polymer MZI sensor using SU-8 and achieved a detection limit of 10^{-9} g l^{-1} (dilute NaCl solution) [58]. The polymer MZIs can also be used as biosensors, for example, Shew *et al*. fabricated a SU-8 MZI to detect rabbit IgG with an maximum sensitivity of 1 ng ml^{-1}[59]. In addition, Lapsley *et al.* exhibited an optofluidic MZI made of PDMS, and showed a RI detection limit of 1.24×10^{-4} RIU [60].

2.4.2.2 Integrated Young's interferometer sensors

Besides MZIs, Young's interferometers (YI) can also be integrated on a chip for sensing applications. As shown in **Figure 2.5(b)**, a coherent laser light is coupled into the input waveguide and then split into a sensing arm and a reference arm using a Y branch. The light waves from the two arms are then projected onto a charge-coupled device (CCD) camera, which forms an interference pattern. The optical intensity distribution, *I(x)*, on the CCD screen can be expressed as [61]:

$$I(\mathrm{x}) = 1 + \cos\left(\frac{2\pi nd}{\lambda_0 f}\mathrm{x} - \delta\right), \tag{2.16}$$

where d is the distance between the sensing arm and reference arm, f is the gap between the output of the YI and the CCD, λ_0 is wavelength in vacuum, n is the effective RI, and δ is the phase shift caused by a RI change. The equation shows that by means of monitoring the changes of interference pattern in the CCD camera, the phase changes of the light in the sensing arm can be measured.

Integrated polymer YI sensor was presented in 2012 by Wang *et al.* with a detection limit of 1.2×10^{-5} RIU [62]. Although its detection limit is lower than the silicon-based devices, polymer YI-based sensor has advantages of easy fabrication and low cost and thus is promising for disposable devices.

2.4.2.3 Other interferometer-type waveguide sensors

Besides MZIs and YIs, many other types of interferometers, such as Hartman interferometer, dual-polarized interferometer, and bimodal waveguide (BiMW) interferometer, can also be used as polymer waveguide sensors. In the BiMW interferometer, two guide modes of the same polarization (TE_{00} and TE_{10} mode) interfere within a straight waveguide, as shown in **Figure 2.5(c)** [63]. For instance, Zinoviev *et al*. fabricated a BiMW interferometer sensor and achieved a sensitivity of 2.5×10^{-7} RIU.

2.5 Summary

In summary, different kinds of polymer microphotonic sensors including free-standing polymer WGM resonator sensors, fiber-based polymer microphotonic sensors and polymer waveguide-based microphotonic sensors are reviewed in this chapter. Although different polymer microphotonic sensors are with different structures, they are commonly based on interaction between the optical field and the stimulus, which induces a variation on spectra response such as shift of the resonant wavelength (frequency), broadening of the resonant peak, and change the intensity of the peak or dip in the spectrum. With the advance of micro/nano technology and the emergence of new functional polymers, polymer microphotonic sensors are under massive development and have

great potentials in biochemical sensing, environment monitoring, and food safety control.

Chapter 3

Optical μ-Printing Based on Maskless Exposure Technology

3.1 Introduction

Photolithography is not only the key step in large-scale integrated circuits manufacturing, but also plays an important role in the development of various micro/nano-photonic devices. In typical photolithography processes, the patterns on the photomask are transferred to the photoresist on the substrate in three steps: photoresist coating, exposing after alignment, and development [64]. To overcome the mask contamination problem in contact exposure, proximity exposure and projection exposure technologies are developed, as shown in **Figure 3.1**.

The photomasks used in lithography are usually expensive and the design and fabrication of a new mask is time consuming. Therefore, maskless exposure technology is highly demanded in the areas that photomask need frequently revised, such as prototyping[65]. Typical maskless lithography technologies can be divided into two kinds: (1) charged particles based maskless exposure technologies, such as electron

beam exposure technology and focused ion beam technology; (2) optical maskless exposure technologies, such as maskless photolithography based on spatial light modulators (SLM), interference lithography and two-photon polymerization. Here we mainly focus on the DMD-based optical maskless exposure technology.

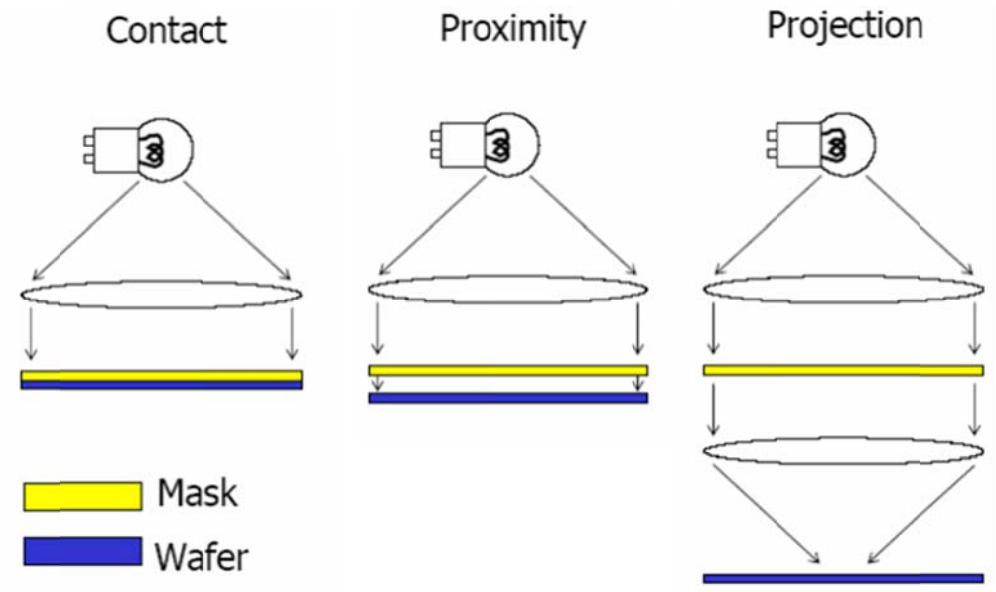

Figure 3.1 Schematics of contact, proximity and projection exposure technologies.

3.2 Optical maskless lithography technology

Figure 3.2(a) shows the schematic diagram of a DMD-based maskless exposure system. An UV light beam passes through the illumination optics and reaches the DMD chip. After the light beam is modulated by the DMD, the image on the DMD chip is then projected onto the photoresist on a

substrate through projection optics. The main components of the whole system, including the illumination optics, DMD chip, and projection optics, are discussed in detail in the following sections.

3.2.1 UV light source

The maskless lithography technologies generally use UV light sources. UV light sources can be divided into coherent light sources (e.g. UV lasers), non-coherent light sources (e.g. high-pressure mercury lamps) and partly coherent light sources (e.g. UV LEDs).

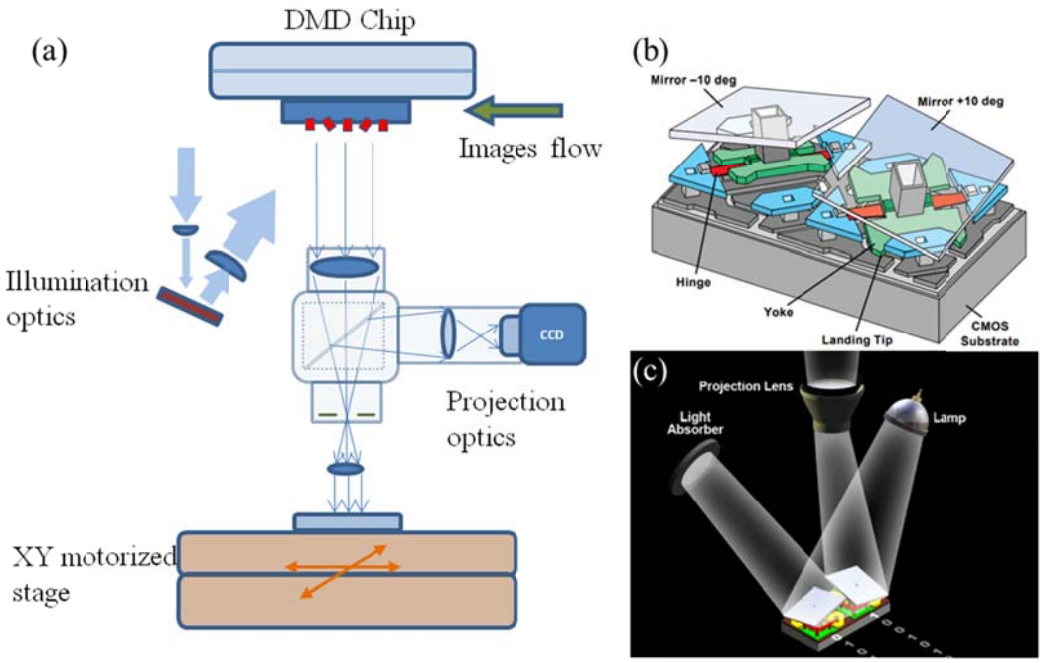

Figure 3.2 (a) Schematic of the DMD based maskless exposure system. (b) and (c) Schematic of the pixel of DMD chip in "on" and "off" states. Reprinted from Ref. [66, 67]

a) High-pressure mercury lamps

High-pressure mercury lamp is one of the widely used non-coherent light

sources, and it has multiple peaks in the UV and visible ranges. In one of our platforms, we use a high-pressure mercury lamp, OmniCure® S2000, from Lumen Dynamics. The wavelength of the emission light is mainly in the UV (190 nm ~380 nm) and visible (380 nm ~770 nm) bands. By using optical filters, the emission light of different bands can be selected accordingly. A high-power fiber light guide is used to guild the light from the mercury lamp to the illumination optics.

b) UV LEDs

Because of the advantages of long lifetime and low power consumption, LEDs have been widely used in not only daily light but also optical manufacturing. By the recombination of the electrons and holes generated in AlGaInN material, blue light and UV light can be generated. Since the light emitted by the UV LED is partly coherent, the interference speckle effect of UV LED is not as severe as laser source. In one of our platforms at the lab, the UV LED from Hamamatsu Photonics (Model No.: LC-C2) is used.

3.2.2 Digital micromirror devices

The spatial light modulator (SLM) is the core part for generation of optical patterns in an optical maskless exposure system. Through liquid crystal display (LCD) was first used as SLM in maskless exposure system [68, 69]. However, it has some disadvantages including large pixel size, low filling

rate, long response time and strong absorption in UV band. These shortcomings limit its application in lithography applications. In 1987, Dr. Larry J. Hornbeck of Texas Instruments, USA invented a reflective SLM called DMD. Because of its small size, high speed and high reflectivity in UV range, DMDs have been widely used in projectors and maskless exposure system for optical image generation.

As shown in **Figure 3.1(b)** and (c), the DMD chip is an array of micron-sized micromirror, protected by a glass window [66, 67]. Typical pixels of DMD chips include 640 × 480, 800 × 600, 1024 × 768, 1280 × 1024 and 1920 × 1080. Those micromirrors are arranged in rows and columns, with a fill rate of more than 90%. Each micromirror represents one DMD pixel and is controlled by the corresponding memory cell. Each micromirror has three possible states, namely, on, off, and reset, which are controlled by the binary signal input to the address electrode. When there is no binary signal, the micromirror is in the “reset” state; if the binary signal is 1, the micromirror is in the “on” state and rotates about 12° from the axis. The irradiated light beam is then reflected to the projection optics; if the binary signal is 0, the mirror element will be in the “off” state and rotate around -12° from the axis. The irradiated light beam is then reflected outside the aperture of the projection optics and absorbed by the absorber. DMD chip can control each micromirror individually to generate any

user-defined patterns.

To conclude, DMD chips have the following advantages:

1) High resolution

Owing to its small pixel size and unique manufacturing process, DMD can attain a very high resolution. The commercial DMD chips have different pixel sizes including 10.8 μm, 13.68 μm and 17 μm. Because of its small pixel size and high resolution, DMD chip can be used to accurately display small features of patterns.

2) High efficiency

DMD chips are commonly with fast response, high filling factor and high reflectivity. In general, owing to the light weight and thus small inertia of micromirrors, the response time of switching is short. Compared with other SLMs, the filling factor of DMD is very high, which can reach 98%, while it is only 56% for LCD. Thus, DMD chips have high optical efficiency and can decrease the power consumption for maskless lithography applications.

3) High contrast ratio

The contrast ratio of DMD chips can reach as high as 2000: 1, while that of LCD SLMs is commonly lower than 700: 1.

3.2.3 Illumination and projection optics

a) Illumination optics

The illumination optics of optical maskless exposure systems is used to provide uniform light beam, which mainly includes a beam homogenizer and expanding optics. Traditional illumination approaches include critical illumination and Kohler illumination. With the advance of modern lithography, the requirement of uniformity of illumination optics greatly increased to exceed the performance of those two traditional illumination approaches. Therefore, overlapping illumination approaches based on light pipes and microlens array have been widely used. In these approaches, the input light beams are divided into a large number of beamlets, and all those beamlets will recombine around the output to form a homogeneous light beam.

If light pipes were used to homogenize the light beam, the light beam reflects many times on the inner surface of the light pipes and then redistributes among abundant optical modes of the light pipe. The output spot is the combined light beam of all those optical modes, which is usually uniform because of the huge number of modes. The light pipes are commonly divided into two types: solid-core and hollow-core light pipes. Solid-core light pipes are based on total internal reflection principle, which has advantages like high reflectivity, easy processing and low cost. Hollow-core light pipes rely on the inner metallic surface to achieve high reflection. Though the reflectivity of the hollow-core type light pipes is

lower than that of solid-core type, it has no loss caused by the material absorption and the reflection loss at the input and output surfaces. Moreover, the propagation angle of light in hollow-core light pipes is larger than that in solid-core light pipes. Therefore, one can use shorter length of light pipes to achieve the same illumination homogeneity if hollow-core light pipe is used.

By using light tracing method, the homogenizing effect of the light pipes can be simulated. **Figures 3.3(a) and (b)** show a layout of illumination optics using solid-core light pipe. The simulation results of the illumination optics are given in **Figure 3.4**. It can be seen from Figure 3.4 (a) that the optical intensity of output light beam is very homogenous and

(a)

	Object Type	Comment	Ref Object	Y Position	Z Position
1	Source Ga..		0	0.000	0.000
2	Standard ..		0	0.000	10.000
3	Rectangul..		0	0.000	28.000
4	Detector ..	Input	3	0.000	-10.000
5	Detector ..	Output	3	0.000	27.500
6	Standard ..		0	0.000	85.000
7	Standard ..		0	0.000	170.000
8	Detector ..	test	3	0.000	270.000

(b)

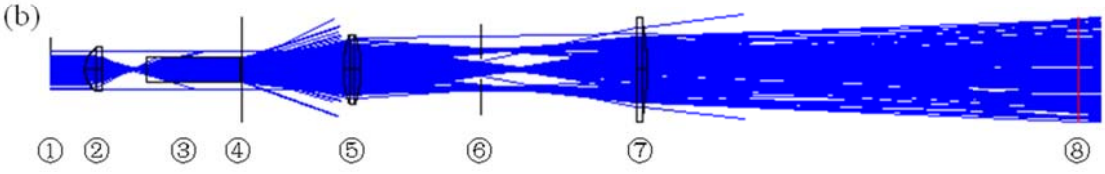

Figure 3.3 (a) table of the optical elements used in the illumination optics; (b) the layout of the illumination optics. ① optical source; ② convergent lens; ③ rectangle light pipe; ④ detector; ⑤ and ⑦ magnifying lens; ⑥ and ⑧detector.

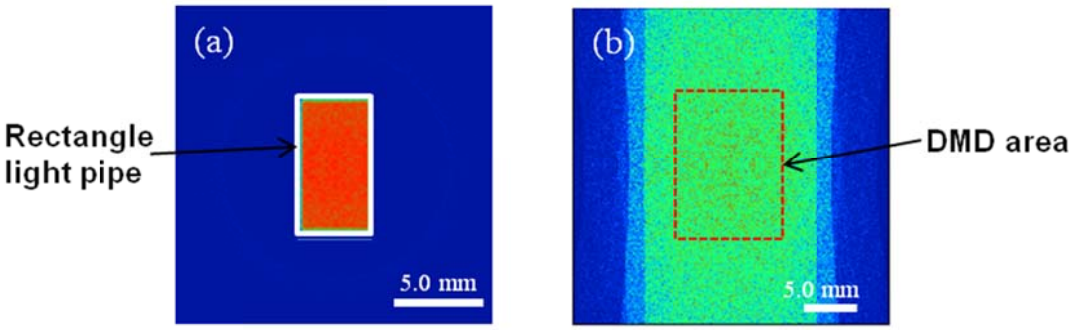

Figure 3.4 (a) and (b) are the intensity distributions at the output of the light pipe and the DMD surface, respectively. The areas of the light pipe's cross-section and DMD surface are 7.7 × 4.1mm^2 and 14 × 10.5mm^2, respectively.

its intensity uniformity is ± 8.6%. Figure 3.4(b) shows that the light distribution projected on the DMD surface is still very homogenous over a rectangular area of 14 × 10.5 mm^2.

b) Projection optics

Projection optics is used to project the image displayed on the DMD precisely on the photoresist for patterning process. One of the advantages of the DMD based maskless exposure technology is that the optical resolution of the system is configurable for the requirements of applications. The magnification or reduction of projection optics directly determines the optical resolution of the exposure system. The digital photomask generated by the DMD chip is different from conventional physical photomask, and several effects induced by the digital photomask should be considered in high resolution exposure process. For instance, the DMD chip is a

micromirror array with approximately 1-μm gap between adjacent micromirrors. When the DMD is directly imaged by high-resolution projection optics on the substrate, a grid structure might form and affect the quality of exposure results.

A typical projection optics for DMD based maskless exposure system is double-telecentric lens. The axial magnification of double-telecentric lens depends on the focal length f_1 of the front lens and the focal length f_2 of the rear lens as:

$$\beta = -\frac{f_2}{f_1}. \tag{3.1}$$

Figure 3.5 is a schematic of a double-telecentric lens. Its aperture is at the coincident point of the back focal point F_1' of the front lens G_1 and the front focal point F_2 of the rear lens G_2. Both the entrance pupil and the exit pupil are at infinity. Since both the incident and output chief ray are parallel to the optical axis, even if the object or the image is slightly defocused, the ratio of reduction keeps the same. Thus, double-telecentric lens usually has a long depth of focus.

The reduction of the projection optics depends on the focal length of the front and back lenses. For instance, for a DMD chip with the pixel size of 13.68 μm, a reduction 0.1× of the projection optics results in an optical resolution of 1.34 μm. The aberration of the projection optics can be controlled within 1 μm with careful optimization of the relative positions of

the lenses, as shown in **Figure 3.6**.

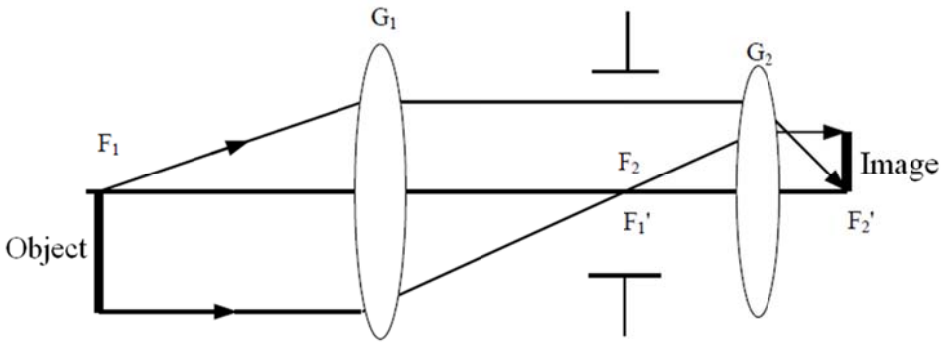

Figure 3.5 Schematic of a double telecentric lens.

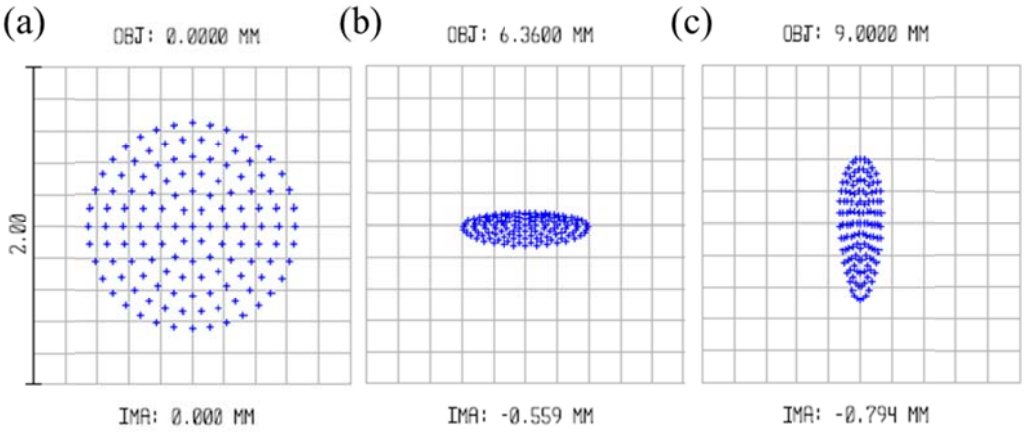

Figure 3.6 Spot diagrams of the projection optics at different positions z=0 mm, z= 6.36 mm and z=9.0 mm, respectively. The corresponding root-mean-square radiuses are 0.498 μm, 0.219 μm and 0.248 μm, respectively.

3.2.4 Imaging model of the projection optics

In order to numerically analyze the optical image created by the projection optics, a partial coherent imaging model is built to simulate the imaging

process. **Figure 3.7** shows the imaging model of the projection optics, where a single micromirror is used to evaluate the performance of the projection optics. The object image is viewed as a combination of individual micromirrors.

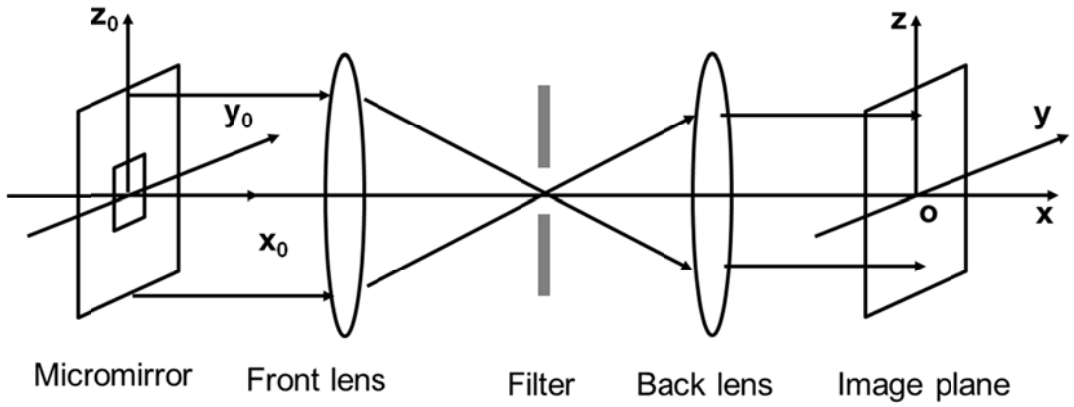

Figure 3.7 Imaging model of the projection optics.

The reflective function of each micromirror can be expressed as:

$$\mathrm{r}(x_0, y_0) = [rect(\frac{x_0}{b}, \frac{y_0}{b}) - rect(\frac{x_0}{c}, \frac{y_0}{c})] \cdot \exp[\frac{j2\pi h}{b\lambda}(x_0 + y_0)], \quad (3.2)$$

where b and c are the width of the edge and center of the reflective micromirror, respectively, and h is the maximum height difference between the tilted micromirror and the flat micromirror. If the above mentioned effect is ignored, the formula can be simplified as:

$$\mathrm{r}(x_0, y_0) = [rect(\frac{x_0}{b}, \frac{y_0}{b}) - rect(\frac{x_0}{c}, \frac{y_0}{c})]. \quad (3.3)$$

By taking a Fourier transform of Equation 3.3, the spatial frequency property of the reflective function can be expressed as:

$$R(\xi,\eta) = F\{r(x_0, y_0)\} = \mathrm{b}^2\mathrm{sinc(b)sinc(b)} - \mathrm{c}^2\mathrm{sinc(c)sinc(c)}, \tag{3.4}$$

where ξ and η indicate the spatial frequency in the direction of x_0 and y_0, respectively. By taking the effect of the filter ($p(\xi, \eta)$) into consideration, the intensity in the image place can be calculated as:

$$h(x,y) = \int_{-\infty}^{+\infty}\int R(\xi,\eta)\cdot p(\xi,\eta)\,\mathrm{e}^{i2\pi(\xi \mathrm{x}+\eta \mathrm{y})}\,d\xi d\eta, \tag{3.5}$$

where $h(x, y)$ is the point extended function of single micromirror. The total intensity distribution on the imaging plane can be calculated by superposing the light energy emitted from each micromirror, which can be expressed as:

$$I_i(x,y) = \sum_{n=1}^{N}\sum_{m=1}^{M}\left\{\begin{array}{l} I_0(n,m)\cdot[\delta(\mathrm{x}-\mathrm{nd},\mathrm{y}-md)*r(x,y)] \\ \cdot \mathrm{rect}(\frac{x}{W},\frac{y}{W})\cdot|\mathrm{h(x-nd,y-nd)}|^2 \end{array}\right\}, \tag{3.6}$$
$$(\mathrm{m}=1,2,3\ldots\mathrm{M};\mathrm{n}=1,2,3\ldots N)$$

where M and N are the number of pixels of the DMD chip in x and y direction, and W denotes the width of the entire DMD array, $I_0(n, m)$ is used to indicate the intensity of the designed pattern in the (n, m) pixel of the DMD chip. The total intensity distribution on the imaging plane can be calculated by the equations mentioned above.

3.2.5 Optical exposure testing

The optical exposure experiments were carried out to test the performance of the own-established maskless lithography setup. The lithography

processes includes the following steps: substrate cleaning, photoresist coating, pre-bake, exposure, post-bake and development. Silica is chosen as the material of the substrate. First, the substrate was ultrasonically cleaned with acetone, DI water and isopropanol sequentially to clean the substrate. A positive photoresist called AZ-5214, which is a commercial photoresist with high resolution and good attachment to silica substrate, was used in the experiments. A thin layer of photoresist was coated on the cleaned substrate through spin coating. The speed of rotation was optimized to ensure that the thickness of photoresist layer was around 1 μm. Thereafter, the samples were prebaked at 105 °C for 2 min to remove solvent. After prebake, the samples were exposed by using the maskless exposure system. The light intensity and exposure time are 33.6 mW cm^{-2} and 40 s, respectively.

Figure 3.8 (a) is the pattern with segments of different linewidths for the testing exposures. **Figure 3.8 (b)** shows the fabricated result, which minimum linewidth is around 1.57 μm. Thus, the estimated minimum feature seize of our maskless exposure platform is able to reach is around 1.57 μm. Besides, the vertical resolution of the μ-printing technology is determined by the minimum expose dose and its corresponding light penetration depth in polymer material. For instance, typical vertical resolution shown in the μ-printing of SU-8 3D microstructures is a few

micrometers, while an ultrahigh vertical resolution of 0.2 μm was achieved in the printing of 2.5D microstructures using poly(acrylic acid).

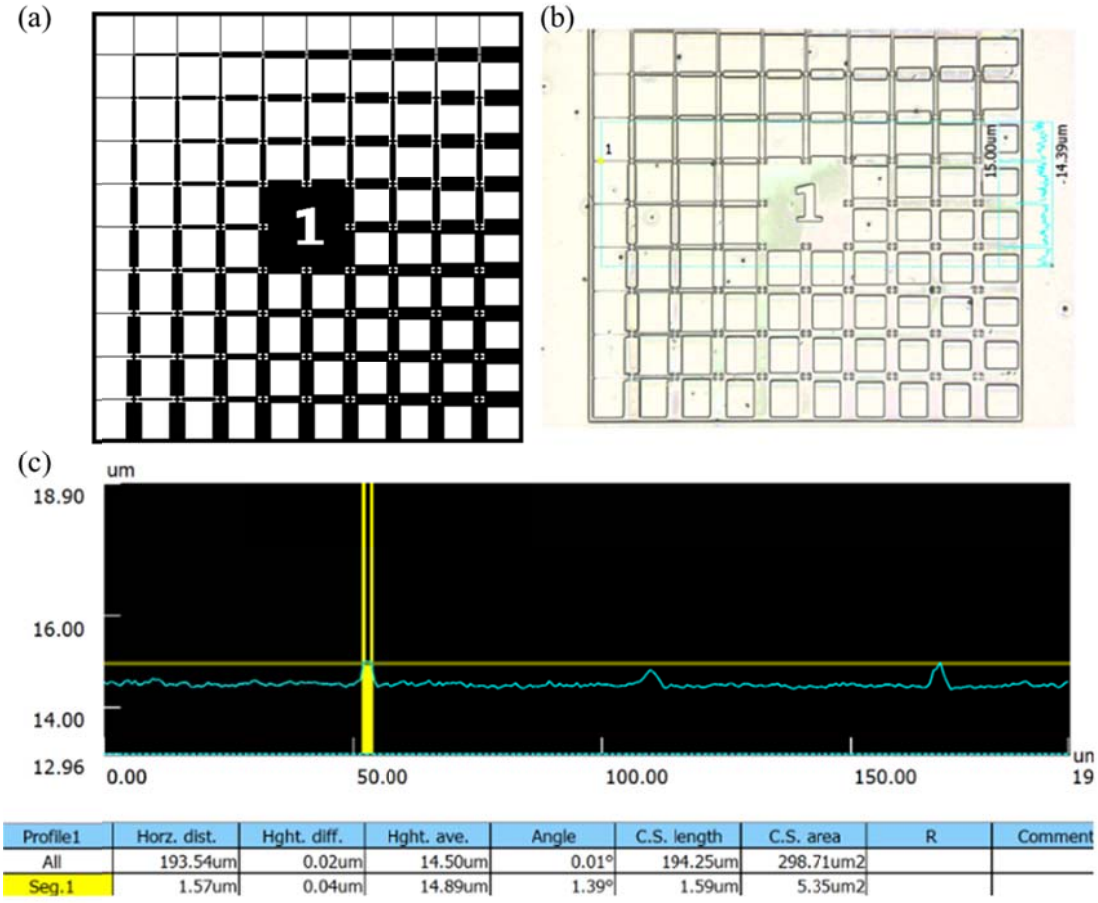

Figure 3.8 (a), (b) and (c) are the testing pattern, preliminary fabrication result and measured minimum linewidth, respectively.

3.3 Optical μ-printing technology

Such a DMD-based optical maskless exposure technology is an ideal

technique for processing functional materials for direct fabrication of microdevices, which is usually called as optical μ-printing technology. Compared with other optical printing technologies, this technology has the advantages of high speed and high flexibility.

For instance, with a DMD-based maskless exposure setup, Shaochen Chen's group demonstrated a polymer (1,6-hexanediol diacrylate) microlens array with a diameter of 230 μm for optoelectronics and integrated optics application [70]. In their work, grayscale images were prepared according to the design of microlens and then were used to create dynamic photomasks so as to control the cured depth of each pixel to achieve the designed microlens, which are one of typical 2.5D structures. Other types of polymer microoptic devices such as Fresnel microlens, Fresnel zone plates and diffraction gratings have been also demonstrated [71, 72].

Optical μ-printing technology is also an ideal technology to process polymer functional materials. For instance, Zhang *et al*. developed a DMD-based optical bioprinting technology to process biomaterials like polyethylene glycol diacrylate (PEGDA) and gelatin methacrylate. With the developed bioprinting technology, complex 3D extracellular microenvironments can be quickly fabricated in a very short time. Moreover, Soman *et al.* fabricated 3D PEGDA scaffolds to investigate

immigration behavior of cancer cells; Gou et al. fabricated functional polydiacetylene nanoparticles-mixed PEGDA microstructures to investigate a bio-inspired detoxification [73]; Kim et al. developed a 3D piezoelectric devices using barium titanate nanoparticles-incorporated EGDA [74].

In a short, DMD-based optical μ-printing technology provides a new way to flexibly and directly process functional material for abundant applications ranging from micro-optics to tissue engineered scaffolds and microelectromechanical systems.

3.4 Summary

In summary, optical μ-printing technologies based on maskless exposure approaches was introduced in this Chapter. Firstly, the background of maskless exposure technology was introduced. Secondly, different parts of an optical maskless exposure system, including the light source, DMD chip, illumination optics, projection optics and its imaging model were discussed and in detail. Then, the optical exposure testing results were presented. Finally, DMD-based optical μ-printing technology and its applications were introduced.

Chapter 4

Optically 3D μ-Printed Polymer Whispering-Gallery-Mode Resonators

4.1 Introduction

Optical WGMs are resonances of an optical field near the circular ring boundary of a resonator by total internal reflection [75, 76]. Optical WGM resonators are named after the acoustic whispering galleries, where a whisper can be heard anywhere along the border of a round room. The optical properties of optical WGM resonators mainly depend on the geometries of the resonators, including spherical [77-79], microdisk [80-82], microtoroid [21, 83, 84], microbottle [85, 86], microring [87-89] and microbubble [90-92]. As their evanescent fields reaching out to surrounding environment are enormously sensitive to external disturbance, the induced shift or broadening of the resonant peaks or valleys can be used for ultrasensitive detecting, e.g. the identification of a single particle or virus [93-95], and the detecting of various gases [12, 96-98]. Additionally, owing to the low loss and small mode volume, optical WGM resonators can achieve ultrahigh Q values and high energy density [21, 22]. All these

factors make WGM resonators a perfect platform to exploit emerging photonic concepts and phenomena ranging from nonlinear optics [99] and low-threshold lasing [100, 101] to cavity optomechanics [102, 103].

Optical WGM resonators have come into existence for a long time, especially the spherical ones. The most common fabrication method for spherical WGM resonators is thermal or electric-arc melting of silica material [77, 78]. However the fabrication technique for nonspherical optical WGM resonators usually contains four stages: photolithography, pattern transfer, selective etching, and thermal reflow [21, 75, 104]. These procedures are fairly time-consuming and might limit their practical applications, especially for large-scale cases. The aforementioned issues can be addressed by using polymer optical WGM microresonators [105-107]. Compared with microresoantor made of inorganic materials, polymer WGM resonators have the merits of biocompatibility, low cost, and processibility. For example, a replica-molding approach was employed to fabricate toroid-shape PDMS WGM resonators [106]. Granting that the above mentioned strategy is a fast and effective method to fabricated PDMS WGM resonators in a large scale, this approach is limited in shape and material.

In this Chapter, we present an optical 3D μ-printing technique to rapidly fabricate polymer optical WGM resonators and resonator arrays. **Figure 4.1** demonstrates the setup of the optical 3D μ-printing system,

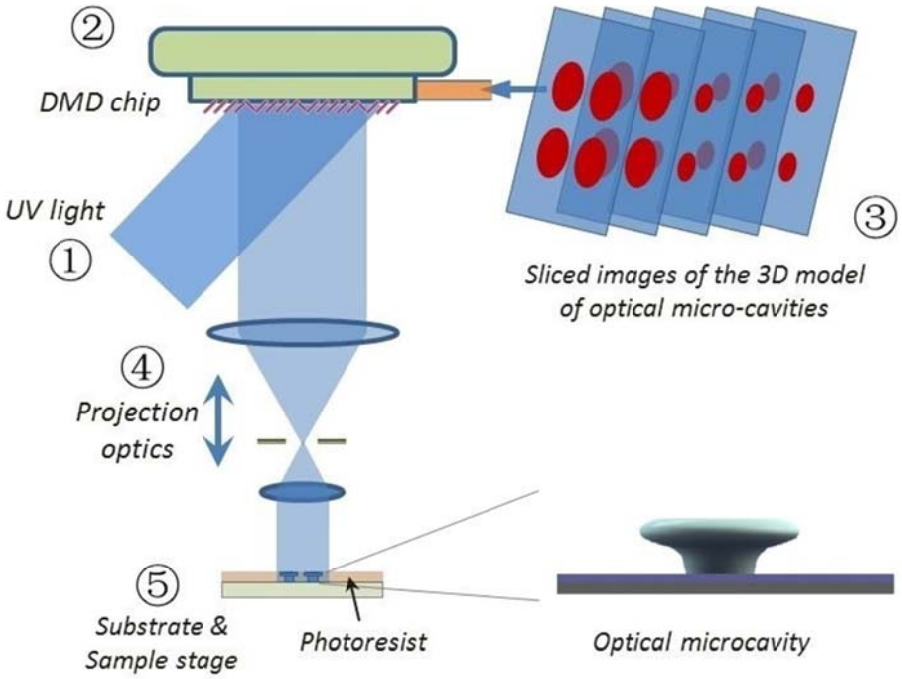

Figure 4.1 Schematic illustration of the 3D μ-Printing technology.

where UV light source (OmniCure 2000 System.) and a high-speed SLM, i.e. DMD (DLi4120 0.7" XGA), are utilized. Thanks to the dynamic-pattern-generation ability of the DMD chip, the UV light reflected by the DMD chip displays 2D optical patterns as indicated by the images sliced from 3D models of the WGM resonators. After passing through a 5× reduction projection optics, the dynamic optical patterns are imaged upon the photoresist spin coated on a glass substrate. Owing to the monotonically additive light absorption property of the photoresist, a predesigned polymer WGM resonator can be fabricated through layer by layer polymerizing [108]. In contrast to previously reported approaches [21, 104-106], this optical 3D μ-printing technology is substantially more adaptable for

fabrication of complex WGM resonators. It is especially reasonable for directly printing of polymer WGM resonators for on-chip integration.

4.2 Fabrication of polymer suspended-disk WGM resonators

A typical epoxy-based negative photoresist SU-8 was utilized to fabricate polymer WGM resonators. Owing to its excellent optical property in both visible and near infrared ranges, good chemical resistance and mechanical property [53, 58, 133], SU-8 is an ideal material for permanent polymer optical micro/nano devices. The SU-8 photoresist used in our experiments is a mixture of epoxy resin, solvent, photoacid generator and inhibitor, where octoxyphenylphenyliodonium hexafluoroantimonate (OPPI) from Hampford Research Inc. and tributylamine from Meryer Chemical Technology Co., Ltd. were utilized as photoacid generator and inhibitor, respectively. These components were dissolved in cyclopentanone in the weight ratio of OPPI/tributylamine/SU-8/cyclopentanone = 2:0.014:100:98. Before the fabrication process of the WGM resonators, a 2-μm thin layer of SU-8 was spin coated and cured to improve the adhesion between SU-8 photoresist and glass substrate. Then, a 100-μm thick layer of SU-8 photoresist was spin coated upon the buffer layer. Thereafter, the substrate was soft baked at 65 °C for 7 min and 95 °C for 20 min in sequence to get rid of the solvent.

Dynamic optical exposure setup, as appeared in **Figure 4.1**, was then employed to exposure the SU-8 photoresist by using a dynamic optical projection method. In order to fabricate a predefined WGM resonator, its 3D model was first designed by using commercial CAD software (Solidworks). The 3D model was then sliced into 200 layers of image data by in-house add-on software. These image data was loaded to the DMD chip in sequence, to dynamically produce predefined light patterns. The designed 3D microstructures were fabricated based on the additive penetration depth of light in the photoresist. Both the projection system and the substrate kept still in the exposure process. The light intensity of the UV lamp adopted in the experiments was 104.85 mW cm^{-2}. The exposure time of each layer of the WGM resonators was adjusted according to the relationship between the cured depth and the total exposure time, which was measured by a trail fabrication of micropillars with incremental exposure time. As shown in **Figure 4.2**, the cured depth increases logarithmically with the increase of exposure time. The slope of cured-depth line can be tuned by the concentrations of absorption dye and photoinitiator.

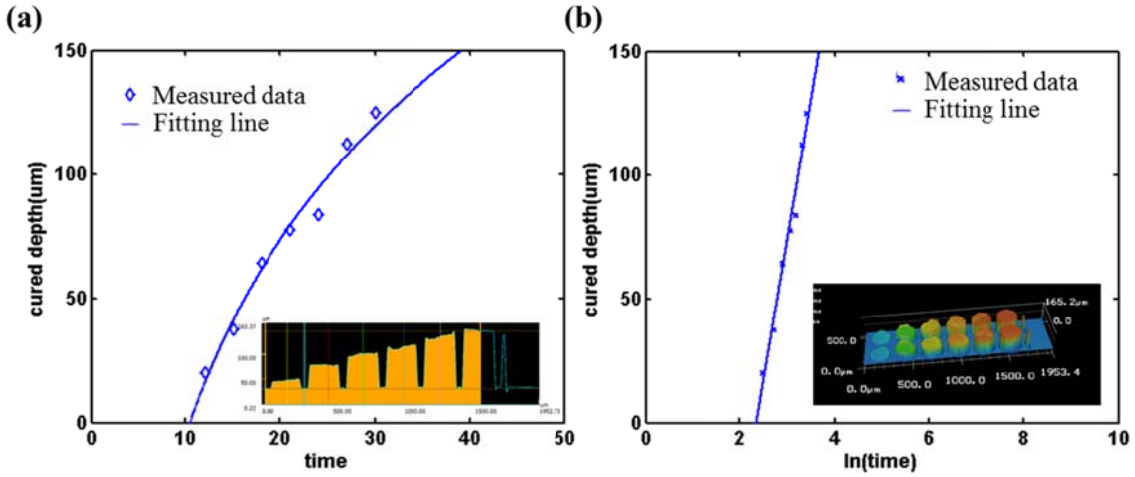

Figure 4.2 (a) Dependence of the cured depth of SU-8 micro pillars on exposure time; (b) Cured depth versus logarithm of time. The inset is the laser-scanning confocal 3D image of SU-8 micro-pillars fabricated with different exposure doses.

The time of exposure for each layer was 275 ms, and overall time of exposure for the predefined WGM resonators was 55 s. After the exposure procedure, the sample was post baked at 65 °C for 5 min and 95 °C for 10 min in sequence, and developed in propylene glycol monomethylether acetate (PGMEA) for 6 min. **Figure 4.3** shows the whole fabrication process of SU-8 WGM resonators.

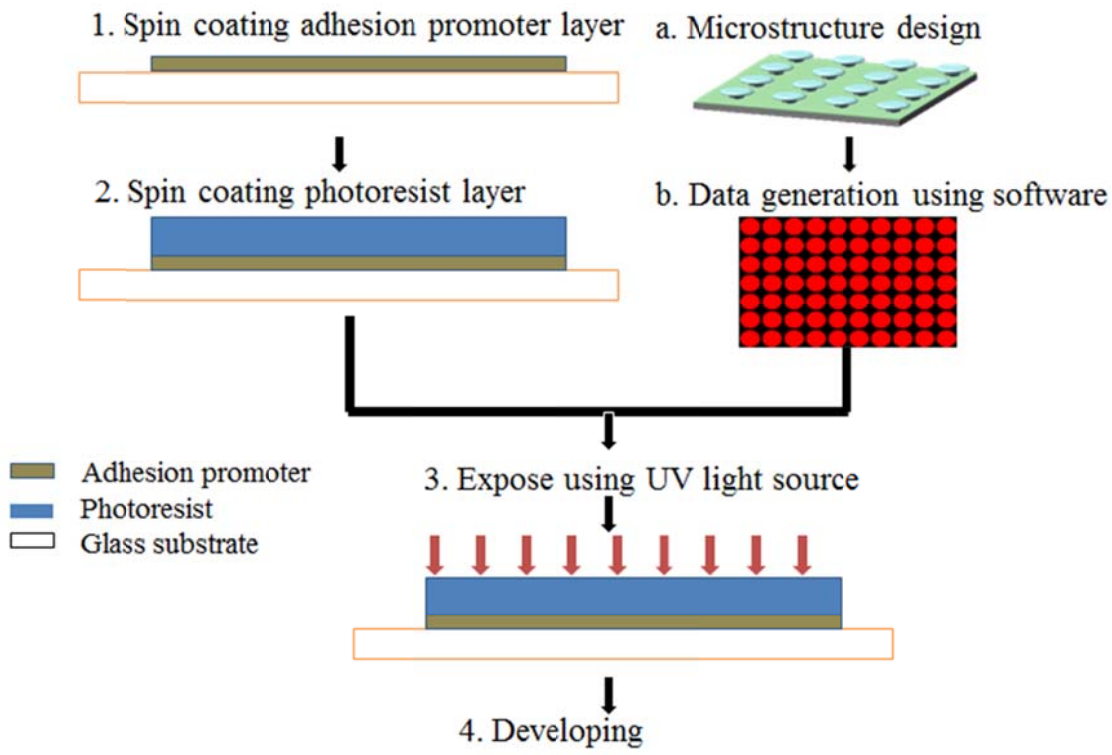

Figure 4.3 Schematic diagram of the fabrication process of the SU-8 WGM resonators.

Figure 4.4(a) shows a side-view optical microscope image of the fabricated SU-8 WGM resonators, and **Figure 4.4(b)** and 4(c) present the scanning electron microscope (SEM) images of the WGM resonators. Evidently, the suspended-disk-shape WGM resonators have smooth surface. As shown in **Figure 4.5**, the root-mean-square surface roughness of the top surface is around 5.11 nm, measured by an atomic force microscope (AFM) (MultiMode 8, Bruker, Germany). The shape of the fabricated WGM resonator is nearly the same as the designed one appeared in **Figure 4.1**. The outer diameter and height of the suspended-disk-shape WGM resonators is 460 μm and 100 μm, respectively. **Figure 4.4(c)** presents the SEM picture of

a 4x3 array of SU-8 WGM resonators fabricated by the one exposure process. The results demonstrate that the fabrication procedure is very flexible and suitable for large scale fabrication of WGM resonators. Besides, the exhibited fabrication procedure is not material specific and can be applied to most photo-crosslinkable materials.

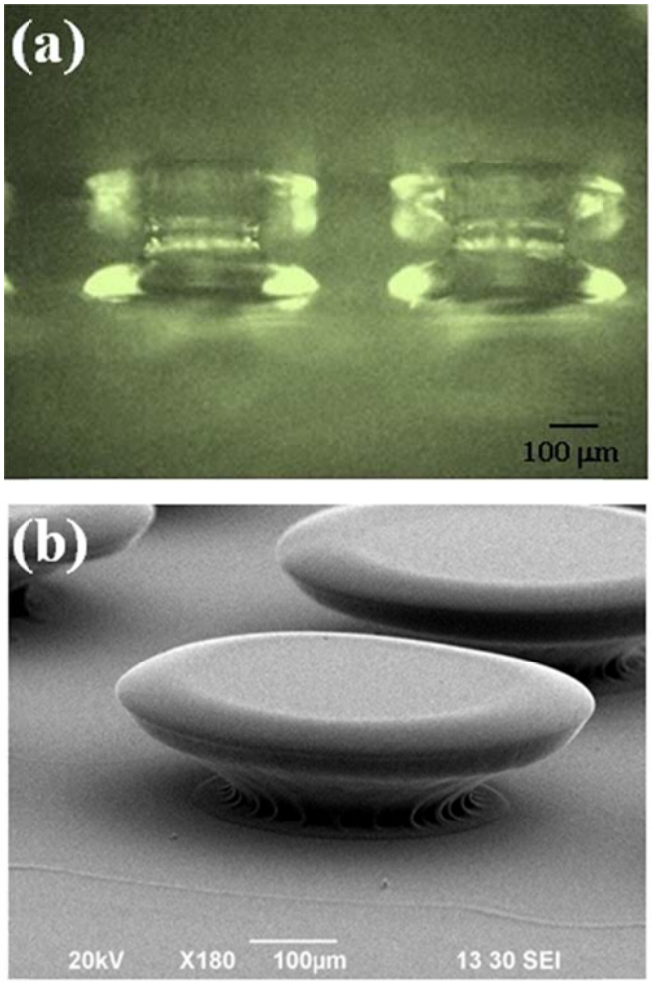

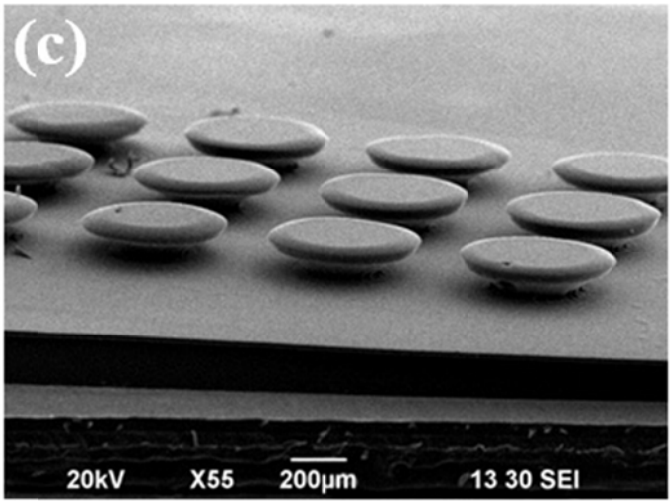

Figure 4.4 Microscope images of the fabricated SU-8 WGM resonators: (a) optical microscope image of the fabricated WGM resonators and its mirror image in the side view, (b) and (c) SEM images of a WGM resonator and a WGM resonator array, respectively.

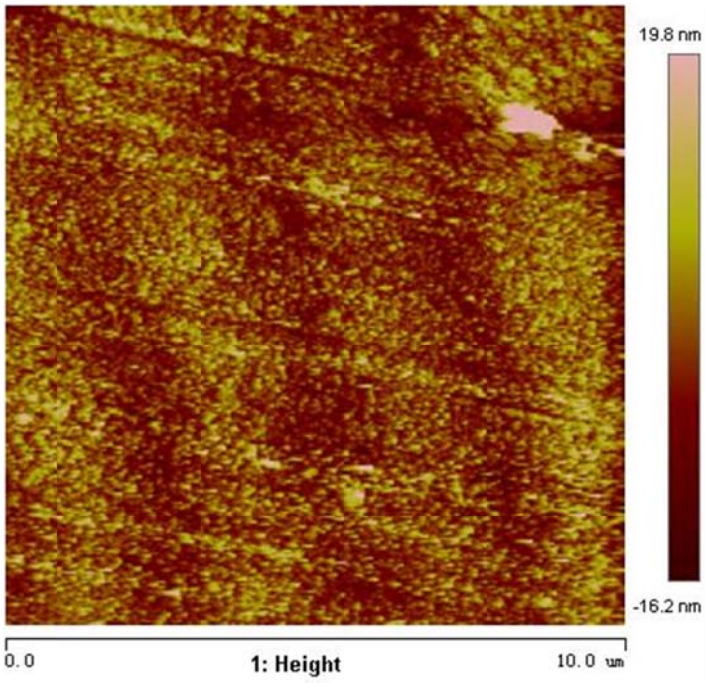

Figure 4.5 AFM image of the fabricated WGM resonator (top surface).

4.3 Simulation of the WGM resonator

The electromagnetic field in the SU-8 WGM can be depicted by time-dependent Maxwell's equations. In a source-free and insulating media, the wave equation can be rewritten as:

$$\nabla^2\mathbf{E}-\frac{n^2}{c^2}\frac{\partial^2\mathbf{E}}{\partial t^2}=0 \quad , \tag{4.1}$$

where n and c are the RI of the media and the speed of light in free space, respectively. For time-harmonic fields, where $\mathbf{E}(\boldsymbol{r}, \mathbf{t}) = \mathbf{E}(\boldsymbol{r})e^{-i\omega t}$, equation 4.1 can be rewritten as:

$$\nabla^2\mathbf{E}+\frac{n^2\omega^2}{c^2}\frac{\partial^2\mathbf{E}}{\partial t^2}=0 \quad . \tag{4.2}$$

Assume the resonance plane of the WGM resonator is placed in the (x, y) plane, the transverse electric (TE) field can be described by $\mathbf{E}(\mathbf{r}) = E(x, y)\mathbf{z}$. In this instance, the equation 4.2 turns into a scalar Helmholtz equation:

$$\nabla^2\mathbf{E}+n^2k_0^2\frac{\partial^2\mathbf{E}}{\partial t^2}=0 \quad , \tag{4.3}$$

where k_0 is the wave number in free space.

To investigate the optical field distribution and spectral properties of the suspended-disk WGM resonators, a numerical simulation based on finite element method (FEM) was adopted. Commercial software, COMSOL Multiphysics, was used to resolve the possible resonant modes and their

spatial distribution. According to the previous literature [20, 109, 110], a 2D simplified model can be applied to 3D rotationally symmetric WGM resonators to save enormous memory and time, as shown in **Figure 4.6(b)**. It should be noted that any transverse mode approximation to Maxwell's equations was not invoked in the simulation.

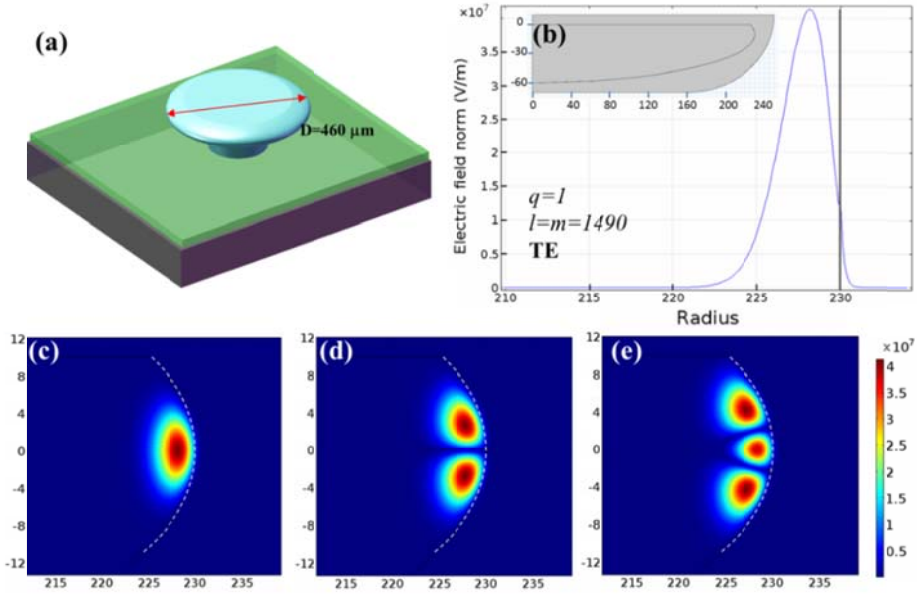

Figure 4.6 (a) Schematic illustration of a suspended-disk SU-8 WGM resonator with the diameter of 460 μm; (b) The radial intensity distribution of its fundamental mode; (c), (d), and (e) are the field distributions of WGMs at the cross section of the WGM resonator. The characteristic indexes are (*q, m, l*) = (1, 1490, 1490), (1, 1490, 1491) and (1, 1490, 1492), respectively.

By solving the scalar Helmholtz equation in a cylinder coordinate, the mode structure of the suspended-disk WGM resonator can be approximately indicated by four indices (*p, q, m, l*), where *p* stands for the polarization of

the electromagnetic field (transverse magnetic or transverse electric polarization); *q* denotes the radial order number signifying the number of maxima the radial direction; *m* indicates the azimuthal mode number showing the quantity of maxima in the equatorial plane; *l* is the polar mode number meaning the number of wavelengths packed along the periphery of the resonators.

The details of the simulation are shown in **Figure 4.6**. **Figure 4.6**(a) demonstrates the 3D model of the suspended-disk WGM resonator, and **Figure 4.6** (c)-(e) displays the intensity profile of three typical resonance modes at the wavelengths of 1500.412 nm, 1495.568 nm and 1490.994 nm, respectively. Simulation results indicate that the optical intensity field of its fundamental TE mode has 1490 maxima in the equational plane, and evanescent field leaking from the resonator to outer environment accumulate to around 0.062% energy of the entire mode.

4.4 Testing of the polymer WGM resonator

4.4.1 Coupling and testing setup

The schematic illustration of the testing system is shown in **Figure 4.7(a)**. Though various methods have been proposed to couple light into and out of WGM resonators [22, 136, 137], the optical fiber taper method is still the most efficient one. So we adopted a biconically tapered optical fiber with

waist diameter of around 2 μm to couple light into the resonator, as shown in **Figure 4.7(b)**. As there are three regions of coupling: under coupled, critically coupled, and over coupled regions, which are classified by the relationship between the intrinsic photon lifetime and the extrinsic photon lifetime; the distance between the optical fiber taper and the equational plane of the WGM resonator require very precise adjustment. Only in the critical coupling case, the WGM resonators have the maximal amount of light trapped due to the equivalence of the loss inside and outside the resonators.

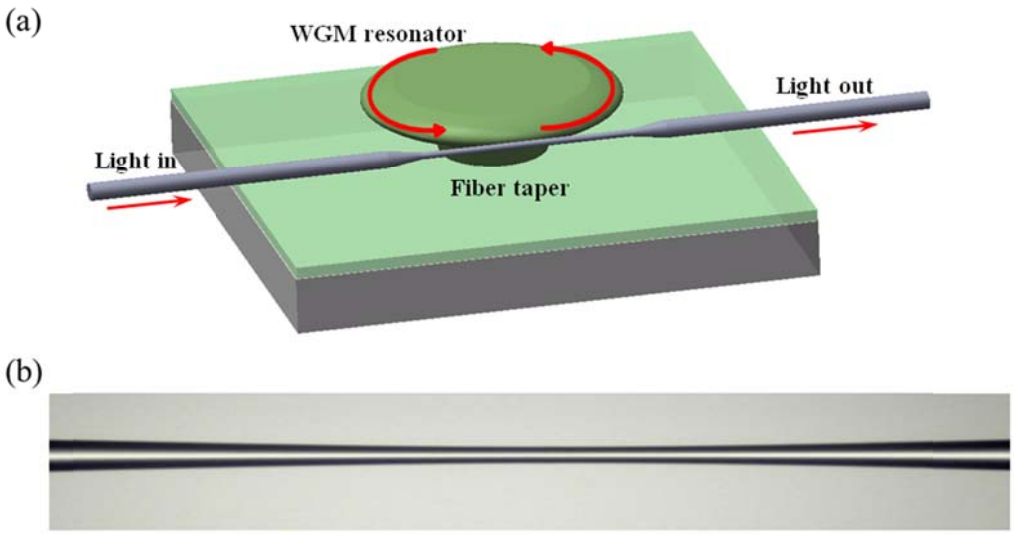

Figure 4.7 (a) schematic of the testing setup, where light from the light source is coupled to the WGM resonator through an optical fiber taper; (b) optical image of a fiber taper.

The fiber taper was fixed to a 5-axis translation stage which permits exact tuning of the distance between the fiber taper and the WGM resonator.

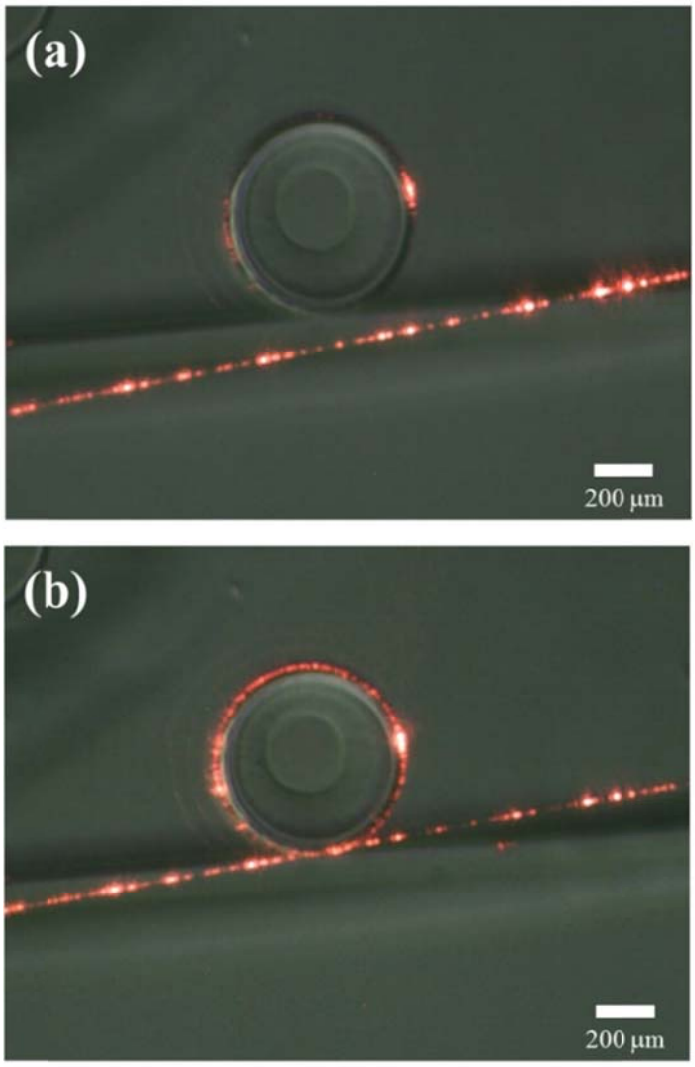

Figure 4.8 Optical microscope images of a SU-8 WGM resonator in case a 650-nm-wavelength laser beam was launched into the fiber from one side using a tapered optical fiber: (a) the WGM resonator in out of couple region; (b) the WGM resonator within couple region.

Two CCD cameras were installed in the top and left sides to monitor their relative positions. Prior to measure the transmission spectrum, a red laser of 650 nm was first employed for assistance of the alignment. **Figures 4.8(a)** and (b) show the optical microscope images of a SU-8 WGM resonator and the tapered optical fiber out of coupling region and in the coupling region,

respectively. It can be seen that WGMs can be efficiently excited with the aid of the optical fiber taper.

4.4.2 Measured transmission spectra and Q factors

After precise adjustment, an amplified spontaneous emission (ASE) light source (around 1550 nm) and an optical spectrum analyzer (OSA) with a resolution of 0.02 nm were then used to measure the transmission spectra of the WGM resonators. **Figure 4.9** indicates two measured transmission spectra of two SU-8 WGM resonators with the radiuses of 230 nm and 160 nm, respectively. Evidently, WGM resonant wavelength can be clearly noticed in the measured transmission spectra. The full width at half maximums (FWHMs) of the WGMs resonant peaks of the two resonators are measured to be 0.23 nm and 0.31 nm, and their free-space ranges (FSRs) are 1.00 nm and 1.44 nm, respectively. The measured FSRs agree well with their theoretical estimations of 1.01 and 1.47 nm which are computed by:

$$\Delta\lambda_{FSR} \approx \lambda^2 / (2\pi nR), \qquad (4.4)$$

where n is the RI of SU-8 photoresist at 1500 nm, R is the radius of the WGM resonator, and λ is the resonant wavelength. Owing to the high-order radial and azimuthal modes of the WGM resonators, subsidiary peaks were also observed in the transmission spectra, which were in agreement with the simulation results.

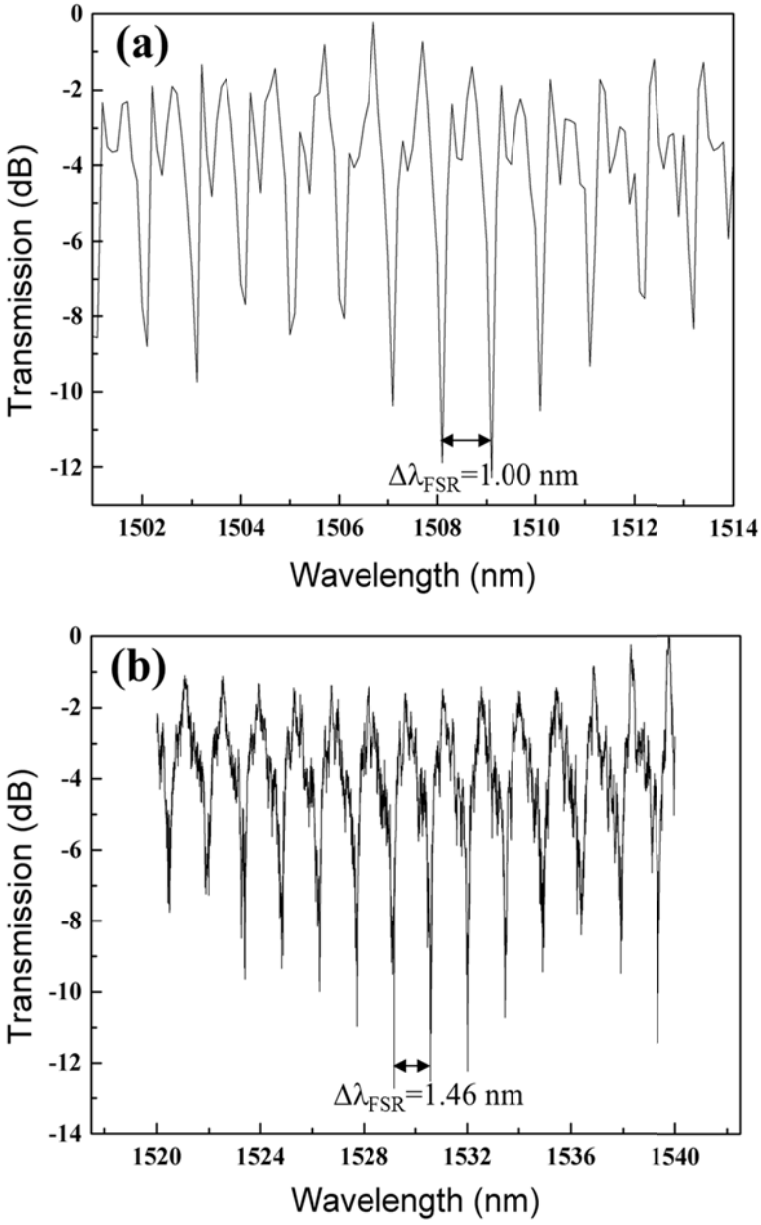

Figure 4.9 (a) transmission spectrum of the SU-8 WGM resonator with the radius of 230 μm; and (b) transmission spectrum of the SU-8 WGM resonator with radius of 160 μm.

The quality factor (Q) is a parameter that defines the damping of a resonant system. In the optical domain, the Q-factor of a WGM resonator is known as:

$$Q \approx \frac{\omega}{\Delta\omega_{FWHM}} \approx \frac{\lambda}{\Delta\lambda_{FWHM}}, \quad (4.5)$$

where λ and ω is the central wavelength and angular frequency of the measured resonance peak, and $\Delta\lambda_{FWHM}$ and $\Delta\omega_{FWHM}$ is the FWHM in wavelength units and angular frequency units of the Lorentzian-shape resonance peak, respectively. Based on the measured FWHMs of the two resonators, the calculated Q-factors of the two SU-8 WGM resonators are 6.4×10^3 and 4.9×10^3, respectively.

4.4.3 Discussions and sensing potential

The measured Q factors of the fabricated SU-8 WGM resonators are not high in comparison with some high-quality WGM resonators [24, 138]. There are several factors contributing to this result: 1) relatively low resolution of the OSA equipped in our lab. The optical resolution of the OSA in our lab is 0.02 nm, which is only one twelfth of the FWHMs of the resonant peaks in the transmission spectra. In spite of the fact that it can marginally resolve the transmission spectra of the fabricated WGM resonators, a spectrum analyser with higher resolution or a tunable laser based testing setup would be able to reveal the profile of resonant peaks more precisely; 2) mode mismatch between the tapered optical fiber and the WGM resonators. As the RI differences between the silica optical fiber and SU-8 photoresists are relatively large, the mode mismatch between the tapered optical fiber and

the WGM resonators will degrade the Q-factor of the resonators [19, 139]; 3) surface scattering caused by the surface roughness and contaminants. Other than the measurement errors, the main contributors to the Q-factor corruption of WGM resonators are known as material absorption and surface scattering [140, 141]. According to previous literature [142], the material absorption coefficient of the cured SU-8 photoresist at 1500 nm is around 2.0 dB/cm. The material-absorption limited Q value can be valued by:

$$Q = \frac{2\pi n_{eff}}{\lambda \alpha} \approx 1.43 \times 10^5 \quad (4.6)$$

,

where α and λ is the material absorption loss and resonant wavelength, respectively. So the Q factors of the fabricated SU-8 WGM resonators are mainly limited by the surface roughness-induced scattering loss. Therefore, the Q-factor of the SU-8 WGM resonators can be further improved by decreasing the surface roughness and reducing the contamination. The surface smoothness can be decreased by means of improving the fabrication resolution of the optical 3D μ-printing system and optimizing the fabrication parameters and the contamination issue can be eliminated if the whole experiment can be conducted in a high-class cleanroom.

Since the evanescent fields of the modes in the inner surface of WGM resonators reach out to the surrounding environment, the variation of the environment induced by external stimulus will result in a shift or broadening of the resonant peaks or dips of the resonant spectra. By

applying this principle, high performance microphotonic sensors can be made to detect various gases or identify single particle or virus. Besides, for some polymeric WGM resonators, the geometry deformation can also be utilized to form high-performance microphotonic sensors, the variation of the geometry will be transferred to the change in the resonant parameters, such as peak wavelength or FWHM.

4.5 Summary

In summary, we have fabricated polymer WGM resonators using optical 3D μ-printing technology. It is demonstrated that optical 3D μ-printing can fabricate SU-8 WGM resonators and resonator arrays in a short time. Optical fiber tapers were employed to couple light from an ASE source into the WGM resonators, and the measured transmission spectra were used to analysis the performance of the polymer WGM resonators. The measured results were in good agreement with the theoretical estimation, and numerical simulations using commercial software COMSOL reveal the mode profile of the supporting modes in the WGM resonators. The proposed 3D fabrication method is not limited in materials; therefore, it has great potential in fabricating WGM resonators of different polymers for the development of different novel photonic devices and sensors.

Chapter 5

Optical Fiber-Tip Pressure Sensors with In Situ μ-Printed Air Cavities

5.1 Introduction

Pressure sensors have widespread applications in biomedicine [113], civil engineering [114], automobile [115] and oil and gas industries [116]. Recently, pressure sensors based on optical fiber-tip Fabry-Pérot (FP) cavity have attracted much attention, because of its unique properties including ultra-small size, remote detection capability, electromagnetic immunity, biocompatibility and chemical inertness.

Fiber-tip FP pressure sensors can be divided into two types: sensors based on the change of cavity RI [117-119] and sensors based on the induced change of cavity length [120-122]. Optical fiber FP pressure sensors based on RI changes usually exhibit a large measurement range, up to 500 MPa, and a relatively low sensitivity in a few tens of pm MPa^{-1} [118, 123]. For optical fiber Fabry-Pérot interferometer (FPI) pressure sensors relying on the change of cavity length, their performances are determined by the materials and thicknesses of the thin diaphragms forming the FP cavities. Although a variety of thin diaphragms made of inorganic materials have been explored,

including silicon membranes [124, 125], graphene thin layer [122], silver diaphragms [121, 126], and silica membranes [127-129], the mechanical strength of these nano/micrometer-scale diaphragms is poor because of their fragile nature. Besides, some optical fiber FP pressure sensors based on thin films has limited linear detection range, usually in tens of kPa [121, 122].

Fiber-optic FPI pressure sensors typically are composed of an air-cavity FPI formed by a diaphragm of different materials attached to the fiber end. In view of the design and fabrication of the sensors, different methods are used including direct laser micromaching, wet chemical etching, electric arc fusion splicing of different kinds of fibers together, standard microfabrication techniques such as photolithography and bonding, conventional machining and assembly techniques, and thin polymer/silver/graphene diaphragm covered on the end of a hollow glass tube or other types of spacer. However, most of these fabrication processes are complicated and time-consuming.

In this Chapter, we present a fiber-tip SU-8 FP pressure sensor with a directly printed air cavity. With the own-established optical in-situ μ-printing technology, SU-8 FPIs with diaphragms of controllable thickness were printed on the end face of standard single-mode optical fiber (SMF). The FP reflection spectra of the SU-8 FPIs were measured, and the responses of the fabricated fiber-tip SU-8 FP pressure sensors to the changes of

pressure and temperature were tested.

5.2 Design and analysis of SU-8 FPI pressure sensor

5.2.1 Mechanical properties of thin SU-8 diaphragms

For FPI pressure sensors based on thin diaphragms, the diaphragms serve as the transducing elements to pressure variations. The changes of the environmental pressure will induce the deflection of the thin diaphragms. For a circular diaphragm, the induced deflection can either linearly or nonlinearly depend on the applied pressure according to the pre-strain and load as well as the materials and boundary condition [130].

Our fiber-tip pressure sensors are formed by SU-8 caps on the top face of SMFs, as shown in **Figure 5.1**. The pressure induced deflection of SU-8 diaphragm results a decrease of the cavity length between the fiber end and the SU-8 diaphragm. If the deflection is smaller than 30% of the diaphragm thickness, the deflection *d* with respect to the pressure *P* can be expressed as [131]:

$$d = \frac{3(1-\nu^2)P}{16Et^3}(R^2 - r^2)^2, \qquad (5.1)$$

where *R* is the radius of the diaphragm, *t* is the thickness, and *r* is the radial distance of the measured point, *v* is the Poisson's ratio and *E* is the Young's modulus of SU-8. If the SU-8 cap concentrically aligns on the end face of

optical fiber, the reflection of light takes place mainly in the center of at SU-8 diaphragm, i.e. *r* equals to 0.

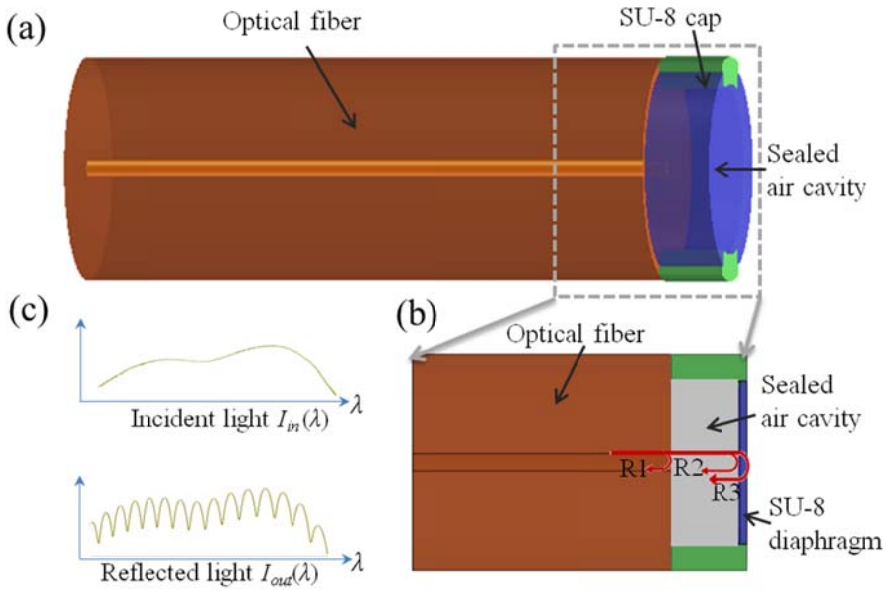

Figure 5.1 (a) Design of the fiber-tip SU-8 pressure sensor; (b) Enlarged image showing the three wave interference and the sealed air cavity; (c)schematic illustration of the incident and reflection spectrum.

The sensitivity of the diaphragm in terms of the ratio between the deflection of the diaphragm and the applied pressure can be written as:

$$\frac{d}{P} = \frac{3R^4(1-\nu^2)}{16Et^3}. \tag{5.2}$$

The properties of SU-8 as listed in **Table 5.1** [132, 133]. The Young's Modulus of the cured SU-8 photoresist is around 3.5 GPa. Therefore, based on Equation 5.2, the pressure sensitivity can be plotted as a function of the radius and the thickness of the SU-8 diaphragms, as shown in **Figure 5.2.**

Table 5.1 Mechanical and thermal properties of SU-8.

Property	Symbol	Value	unit
Young's modulus	E	2~5	GPa
Tensile strength	σ	~60	MPa
Poisson's ratio	ν	0.22	-
Thermal expansion coefficient	α	52	ppm k^{-1}

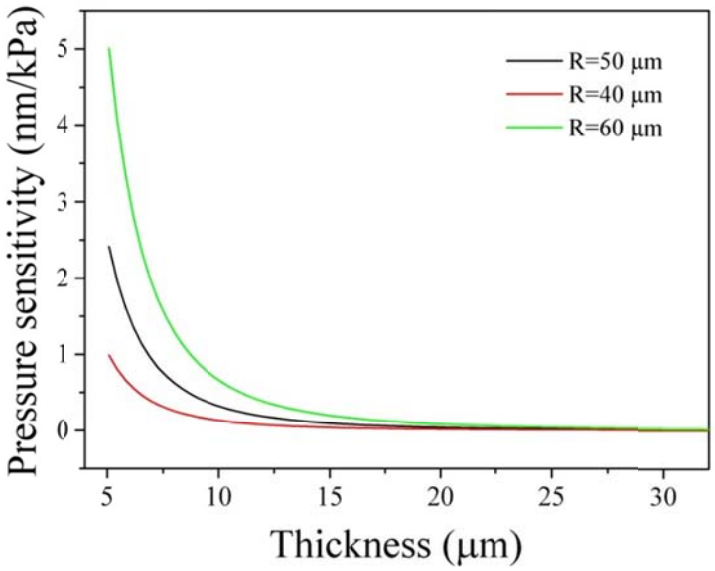

Figure 5.2 Calculated dependences of the pressure sensitivity on the thickness of the SU-8 diaphragm with different radiuses (R=50 μm, 40 μm and 60 μm).

5.2.2 Finite element analysis of SU-8 FPI pressure sensors

To show more details of the mechanical responses of the pressure sensor, the responses of the SU-8 FP pressure sensors with respect to the change of

pressure are numerically simulated by using the commercial software COMSOL Multiphysics. The thickness *t* and radius *R* of the SU-8 diaphragm are assumed to be 11 and 50 μm, respectively. When the applied pressure is 700 kPa, the maximum deflection of the SU-8 diaphragm is calculated as 0.145 μm, as shown in **Figure 5.3(a)**.

As shown in **Figure 5.3(b)**, the maximum von Mises stress of the SU-8 diaphragm is at the center of the structure. As the maximum strength of the SU-8 is 60 MPa, as given in Table 5.1, the maximum allowable pressure of the SU-8 FP pressure sensor is calculated to be ~1.67 MPa.

Figure 5.4(a) shows the simulated deflection distributions of the 11-μm thick SU-8 diaphragm under different maximum pressures. Figure 5.4(b) depicts the linear relationship between the maximum deflections of the 11-μm thick SU-8 diaphragm and the applied pressures. The calculated pressure sensitivity (ratio between the deflection of the SU-8 diaphragm and the applied pressure) of the 11-μm thick SU-8 diaphragm is 0.207 μm MPa^{-1}.

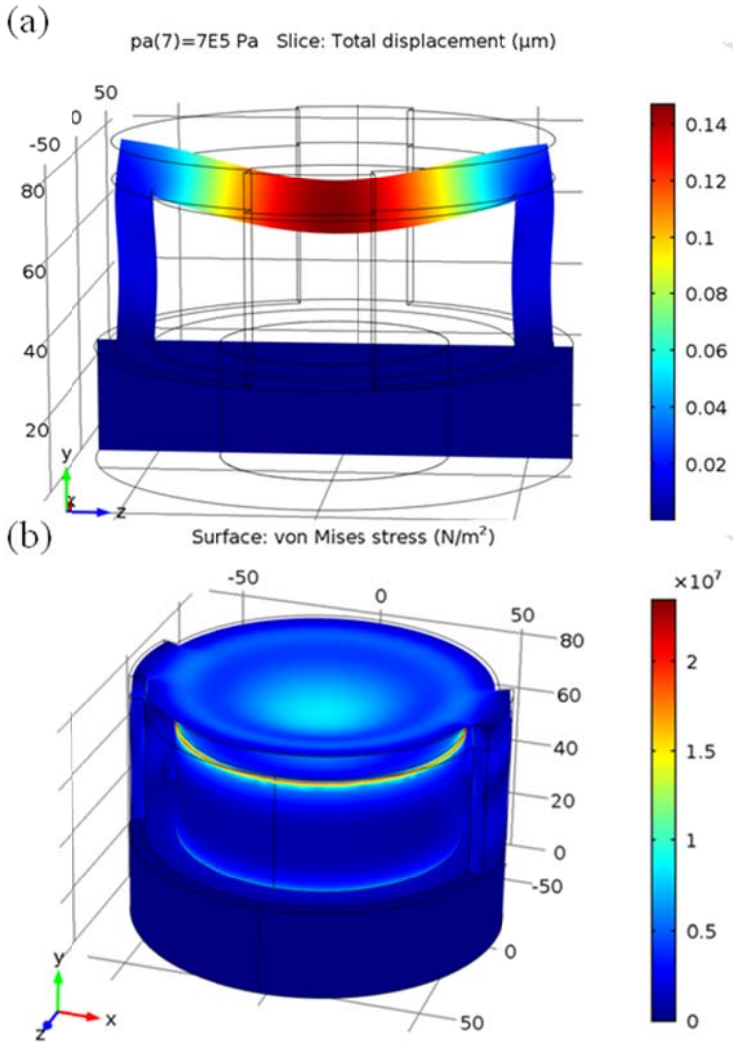

Figure 5.3 (a) Deflection and (b) von Mises stress distribution of the SU-8 diaphragm under the pressure of 0.7 MPa.

It is known that the wavelength shift $\Delta\lambda$ of a dip wavelength in the interferometric spectrum is related to the change of the air-cavity length Δd as $\Delta\lambda = \lambda \cdot \Delta d / d$. Therefore, with the Equation 5.2, the dependence of the shift of the resonant wavelength on the applied pressure sensor can be evaluated. If the length of the air cavity used in simulation is 93 μm and the resonant wavelength is around 1500 nm, the calculated shift of resonant

wavelength with respect to the applied pressure for 11-μm thick SU-8 diaphragm is 3.3 nm MPa^{-1}.

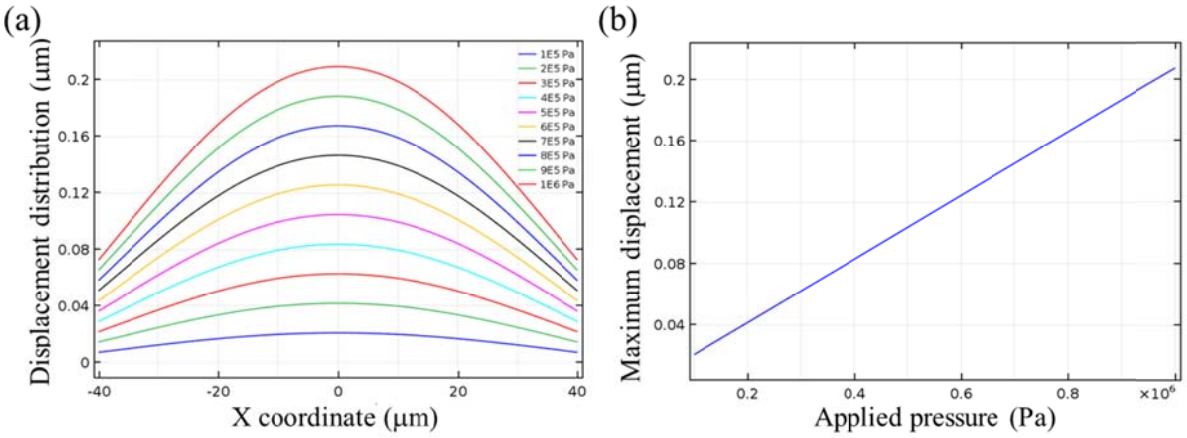

Figure 5.4 (a) Calculated deflection distributions of the 11-μm thick SU-8 diaphragm under different maximum pressures; (b) calculated maximum deflections of the 11-μm thick SU-8 diaphragm with relation to the applied pressures.

5.3 Fabrication of the fiber-tip SU-8 FPI pressure sensor

Because of its excellent mechanical stability and low absorption coefficient in the visible range, SU-8 epoxy is widely used in micro electromechanical systems and microfluidic systems to fabricate permanent structures and devices. The SU-8 epoxy used the experiments was prepared by mixing epoxy resin, photoacid generator, inhibitor and solvent. PC-2506 (Polyset Co., Ltd, USA) and tributylamine (TBA, Meryer Chemical Technology Co., Ltd.) were used as photoacid generator and inhibitor, respectively. These

components were dispersed in cyclopentanone in the weight proportion of PC-2506:TBA:SU-8:cyclopentanone = 2.5:0.014:100:233. After preparation of the photocrosslinkable SU-8 epoxy, a thin SU-8 layer was prepared on the end face of an optical fiber by a dip-coating method. Then the optical fiber was mounted by using an own-designed holder and heated at 65 °C for 15 min and 95 °C for 35 min successively to remove the solvent. It is noteworthy that the concentration of SU-8 solution can be properly adjusted if the desired thickness of the SU-8 layer need changed.

Figure 5.5(a) shows the optical in situ u-printing setup for the fabrication of the SU-8 FP pressure sensors. A two-step exposure process was adopted to fabricate the SU-8 diaphragm and sealing part sequentially, as shown in Figures 5.5(b)~(e). The 3D models of the pressure sensors were first built by using commercial CAD software Solidworks. The 3D model was then sliced into image data of 100 layers by using an own-developed add-on software. After a proper alignment, these image data was then loaded to the DMD chip sequentially for a dynamic exposure process. Due to the additive penetration property of UV light in the polymer material and the long depth of focus of the exposure setup, the designed suspended SU-8 diaphragm can be directly printed on the end face of optical fibers.

The optimized exposure light intensity and exposure time are 281 mW cm^{-2} and 58 s, respectively. After exposure, the sample was post heated at 65

°C for 10 min and 95 °C for 15 min sequentially, and then developed in PGMEA for 6 min after cooling down to room temperature. Finally, the sample was hard baked at 150 °C for 30 min to enhance its mechanical property and adhesion to optical fiber. After printing of the suspended SU-8 diaphragm, similar processes were repeated to print the sealing part so as to form a close air-cavity on the end face of the optical fiber.

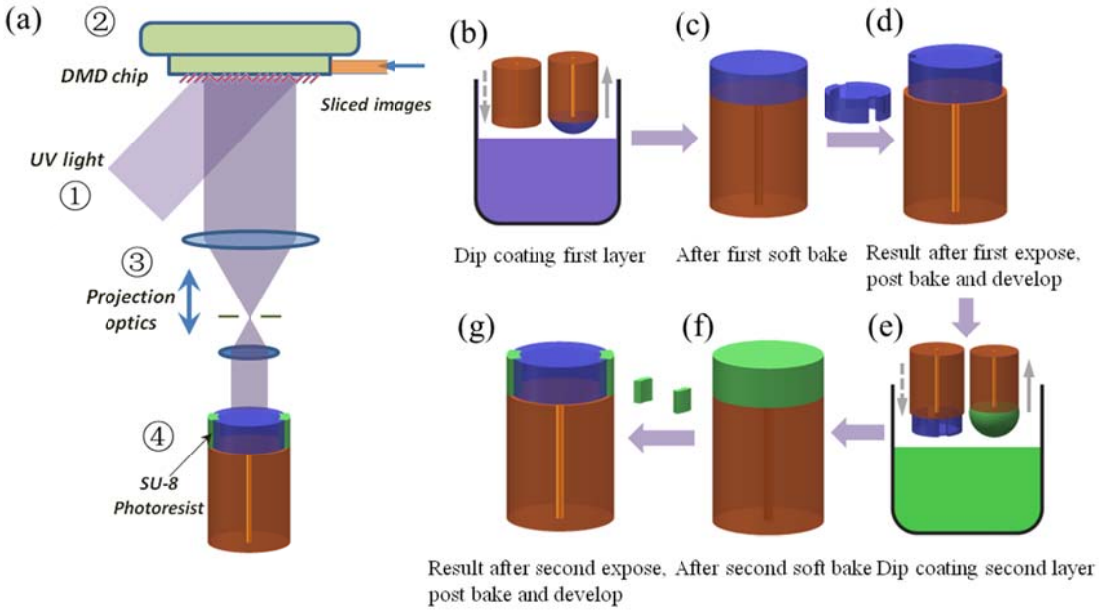

Figure 5.5 (a) Schematic diagram of fabrication process of the SU-8 FP pressure sensors using the optical in-situ μ-printing technology. (b)~(e) A two-step exposure process to fabricate the SU-8 FPI with sealed air cavity on fiber endface.

Figures 5.6(a) and (d) show the side-view optical microscope images of the fabricated open cap after first printing process. **Figures 5.6(b)** and (e) are the SEM images of the fabricated suspended SU-8 diaphragm after first

printing process. **Figures 5.6(c)** and (f) show the SEM images of the two fabricated SU-8 FP pressure sensors with sealing parts. The outer and inner radiuses of the fabricated SU-8 FPIs are 100 μm and 80 μm, respectively, the same as the designed parameters. To achieve different thickness of the SU-8 diaphragms, the thickness of the SU-8 diaphragm in the 3D model is different and thereby the exposure dose for the SU-8 diaphragm in the first exposure process can change accordingly.

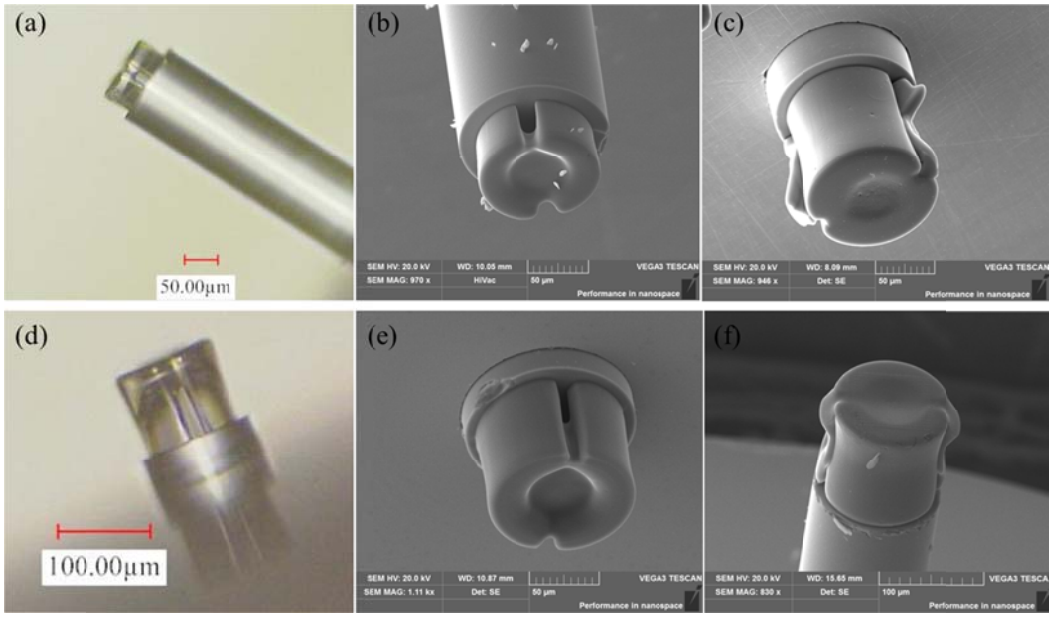

Figure 5.6 Microscope images of the two examples of the SU-8 FPIs in different steps.

5.4 Testing of fiber-tip SU-8 FPI pressure sensor

5.4.1 Spectra of the SU-8 FPI pressure sensors

Figure 5.7 shows the measured reflection spectra and their corresponding fast Fourier transform (FFT) results of two SU-8 FP pressure sensors with

different air-cavity lengths and diaphragm thicknesses. Because of the low reflectivity of the SU-8/air and silica/air interfaces, the multiple reflections between the interfaces can be ignored and the three-wave interferences can be used approximate the interferometric fringes in **Figures 5.7(a)** and (c). **Figures 5.7**(b) and (d) show the corresponding FFT results of the interferometric fringes, where the peaks indicate the effective lengths of the FP cavities formed by the three reflective surfaces (fiber end, inner and outer surfaces of the SU-8 diaphragm).

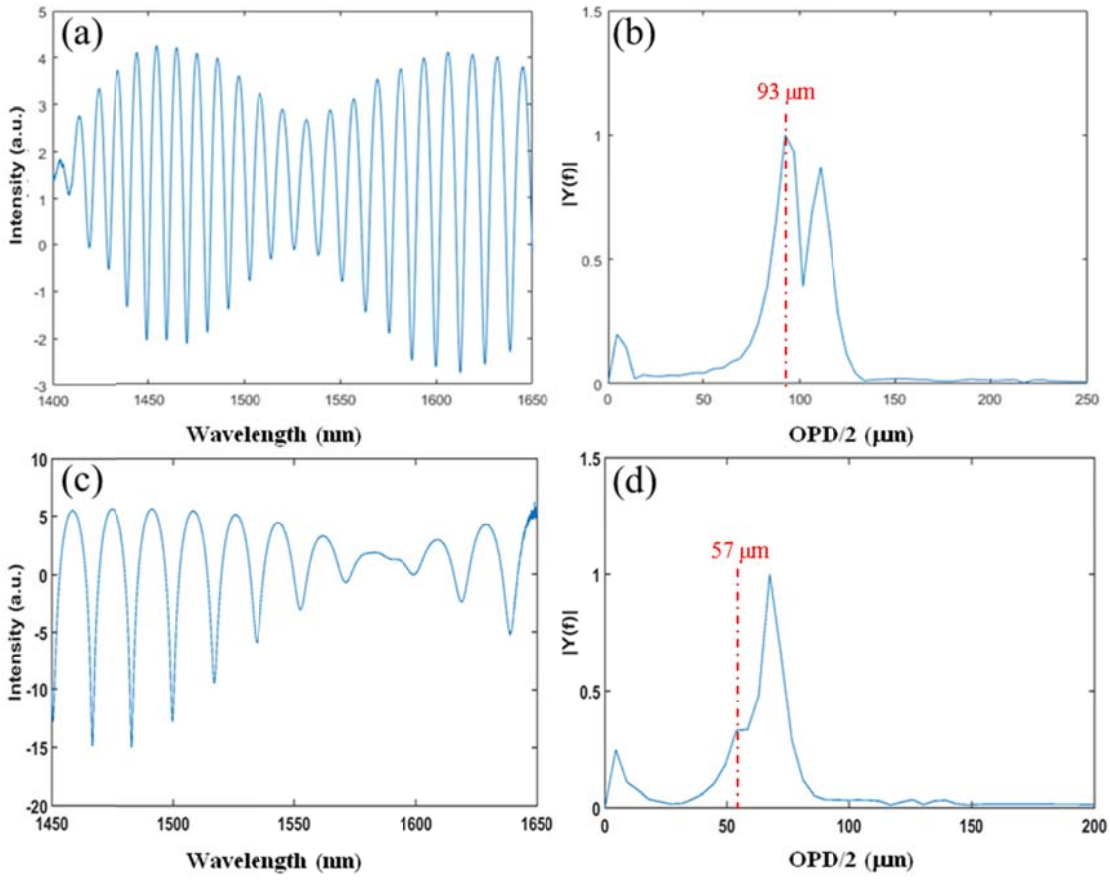

Figure 5.7 Measured reflection spectra (a, c) and their FFT results (b, d) of the SU-8 FP pressure sensors with the air cavity length the SU-8 diaphragms thickness of (a) 93 and 11 μm, (b) 57 and 8 μm, respectively.

The length of the sealed air cavity and the thickness of the SU-8 diaphragm can also be estimated by using the FSRs of the interference fringes and their envelope by:

$$L = \frac{\lambda_1 \lambda_2}{2nFSR}, \tag{5.3}$$

where λ_1 and λ_2 are the starting and ending wavelength of the calculation FSR, respectively, and n is the RI of the cavity material. The calculated length of the sealed air-cavity and the thickness of the SU-8 diaphragm are 93 and 11 μm, respectively, for the sample shown in **Figure 5.7(a)**, and 57 and 8 μm, respectively, for the sample shown in **Figure 5.7(c)**. And the calculated results agree well with the peaks shown in Figure 5.7(b) and (d).

5.4.2 Testing Results

The responses of the SU-8 FP pressure sensors to the change of pressure and temperature were tested by using a sealed gas chamber connected to a high pressure nitrogen gas cylinder, as shown in **Figure 5.8**. Due to the small thickness of the SU-8 diaphragms, the light reflected from the outer surface of the SU-8 diaphragm modulates the entire reflection spectrum with a slowly varying envelope [134]. Hence, we directly monitor the shift of the peak/valley wavelength of the reflection spectrum to interrogate the SU-8 FP pressure sensors. A commercial pressure meter was connected to the gas chamber to provide a reference. The pressure in the gas chamber was

adjusted by a valve with a step of 50 kPa from 0 kPa to 700 kPa (limited by the commercial pressure meter).

Figure 5.9(a) shows the measured response of the SU-8 FP pressure sensor, whose air cavity length and diaphragm thickness are 93 and 11 μm, respectively. With the increase of the pressure in the chamber, the wavelength of the spectral dip under monitor shows a blue shift (towards shorter wavelength). The SU-8 FP pressure sensor showed good linearity

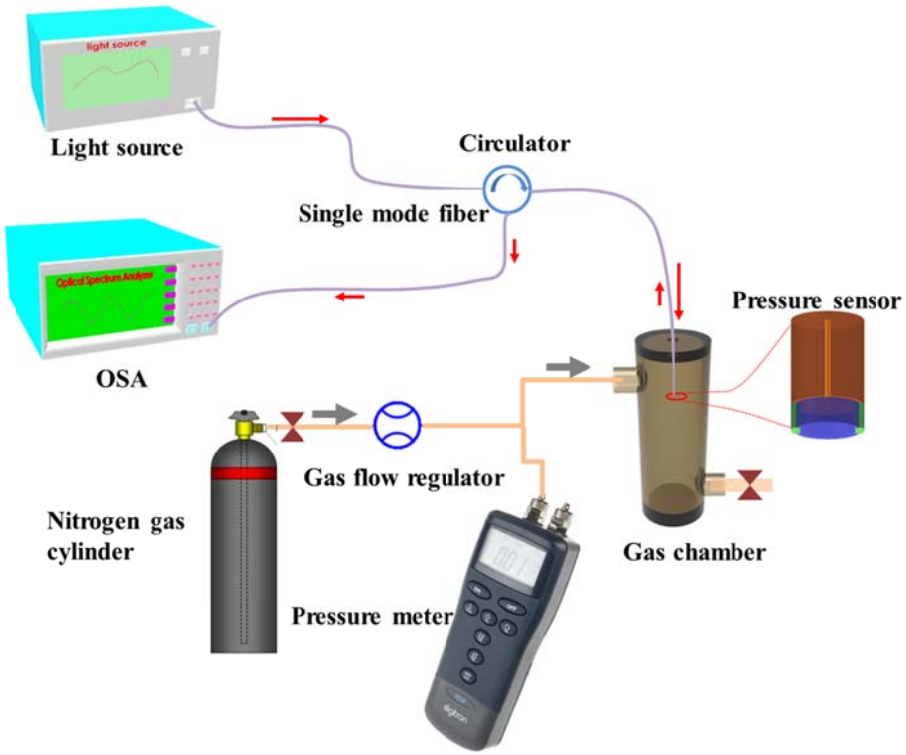

Figure 5.8 Experimental setup for the pressure measurement.

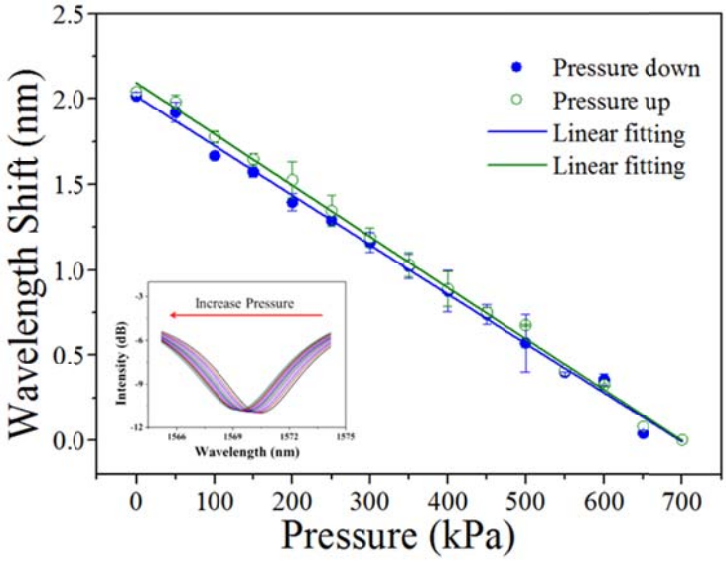

Figure 5.9 Pressure response of the SU-8 FPI pressure sensor with air cavity length of 75μm and SU-8 diaphragm thickness of 11 μm. The inlet shows the shift of the reflected spectrum when increasing pressure.

and reversibility with both increase and decrease of the applied pressure. The sensitivity of the pressure sensor is 2.93 nm MPa^{-1}, which agrees well with the simulated result, i.e. 3.3 nm MPa^{-1}. According to equation 5.3, the lower sensitivity of the fiber-tip pressure sensor is attributed to the thickness and diameter of the SU-8 diaphragm, which are around **1**1 μm and 80 μm respectively.

The temperature response of the fabricated SU-8 FP pressure sensor was also measured. As shown in **Figure 5.10**, the sensor exhibits a linear response in the range of 30 to 65ºC, and shows a temperature sensitivity of ~38 pm/ºC. Theoretically, the temperature response of the SU-8 FP pressure

sensor can be attributed to the thermal expansion of air cavity. For the FP pressure sensor mentioned above, its temperature-cross sensitivity can be calculated as ~ 12.97 kPa/ºC.

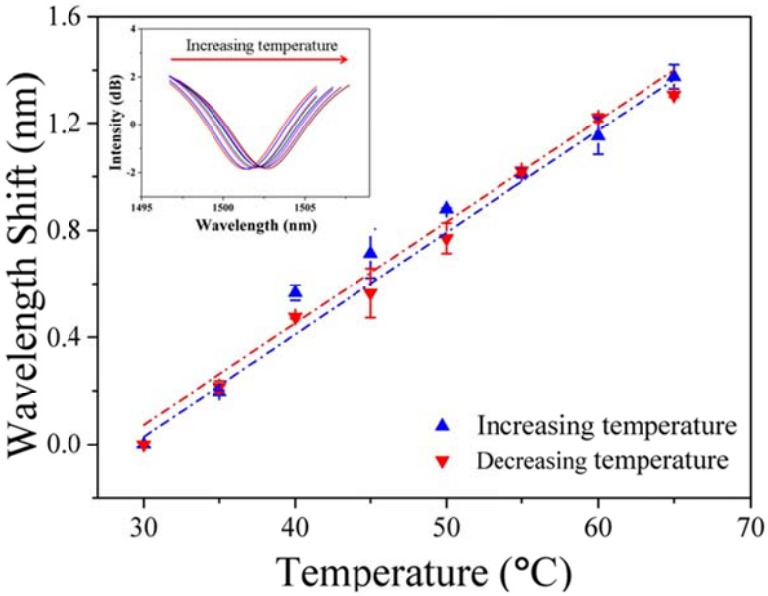

Figure 5.10 Temperature response of the fabricated SU-8 FPI pressure sensor with air cavity length of 75μm and SU-8 diaphragm thickness of 11 μm. The inlet shows the shift of the reflected spectrum when increasing temperature.

5.5 Summary

In this Chapter, we present a novel fiber-tip polymer FPI pressure sensor fabricated by using an own-developed optical in-situ μ-printing technology. The FP pressure sensors with SU-8 diaphragms of different thicknesses were fabricated and tested in the experiments. Reflection spectra with clear interference fringes were measured and analyzed to reveal the dependence of spectral features on the reflections from different interfaces. Because of the

lower Young's modulus of SU-8, the fiber-tip polymer FP pressure sensors show high sensitivity.

Chapter 6

Optical Fiber-Tip CO_2 Sensors Using a Photocrosslinkable Poly(ionic fluid)

6.1 Introduction

Carbon dioxide (CO_2) is the fifth largest gas composition in atmosphere on earth, which is a raw material for photosynthesis of plants, thus vital to lives on earth [135-137]. According to the U.S. Occupational Safety and Health Administration, a CO_2 concentration above 4 vol% has been defined as "dangerous to life and health". Besides, CO_2 sensors play a crucial role in agricultural and food industry [138-140], environment and safety monitoring [141, 142], the volcanic activity [143], vehicle exhaust detection [144], and human healthcare [145]. For example, CO_2 is not only one of the outcomes of food putrefaction but also an ordinarily employed gas for the suppression of the metabolic rates of microorganisms in food packaging applications [138, 139]. Thus, it is very desirable and necessary to monitor CO_2 concentration in agriculture and intelligent food quality control.

Until now, the most commonly used techniques for CO_2 sensing can be divided into electrochemical and optical types according to their sensing mechanisms. A large portion of the presently using CO_2 sensors, for example,

the potentiometric, amperometric, and conductometric sensors, apply electrochemical mechanism [145]. Typical potentiometric CO_2 sensors, e.g. Severinghaus CO_2 sensors, utilize a circuitous strategy for detection [146], which measures the difference in pH value caused by the sorption of CO_2 in electrolyte solutions. With great progress in microtechnologies, solid state electrolyte sensors are quickly taking over CO_2 sensors using wet electrochemical procedures. Nevertheless, solid state electrolyte sensors are generally required to be warmed at high temperature (300 °C– 800 °C) to start chemical reactions [147-150], which brings about long haul instability issues and few areas of applications.

Optical CO_2 sensors usually don't need electrical power, and show low activity to chemicals, conceivably permitting to overcome the shortcomings of electrochemical sensors for harsh conditions as well as remote detecting applications. Most commonly used optical CO_2 sensors are based on infrared detectors. Though they typically have fast response, the bulky size and high cost of the instruments limit their applications. Because of its low cost, low loss, small size and high performance, optical fibers are the most popular optical waveguides, which are promising in fabricating miniature optical CO_2 sensors. For example, Munkholm *et al.* proposed an optical fiber-tip CO_2 sensor made by depositing a polymer layer with a pH-sensitive fluorescent dye on the end face of an optical fiber [151]; Segawa *et al.* built a

fiber-tip CO_2 sensor utilizing a polymer film containing indicative dyes by means of dip-coating technology [152]. The primary disadvantages of the dye-containing polymer based CO_2 sensors are their low biocompatibility and unsatisfactory long-term performance. Moreover, due to the fluctuation of light source, the accuracy of these intensity-based optical sensors is not stable over time.

In this Chapter, we present a new type of fiber-optic CO_2 sensor by using a photocrosslinkable poly(ionic liquid), i.e. poly(1-allyl-3-vinylimidazolium bromide) (PAVB), which has strong CO_2 sorption ability. It should be noted that the synthesis and characterization of PAVB was conducted by our collaborator, Dr. Yuan Jiayin's group in Max Planck Institute of Colloids and Interfaces. To fabricate miniature fiber-optic sensors, it is imperative to pattern PAVB with size of less than 100 μm on the endfaces of optical fibers. Therefore, we adopt an optical in-situ μ-printing technique to prepare Fabry-Pérot interferometers (FPIs) based fiber-optic CO_2 sensors by in situ and directly patterning PAVB and SU-8 FPIs (≈ 60 μm in diameter) on the top face of an optical fiber, as shown in **Figure 6.1**. The microsensors show simultaneous measurement of CO_2 concentration and temperature with good sensitivity and selectivity as well as a wide dynamic operation range.

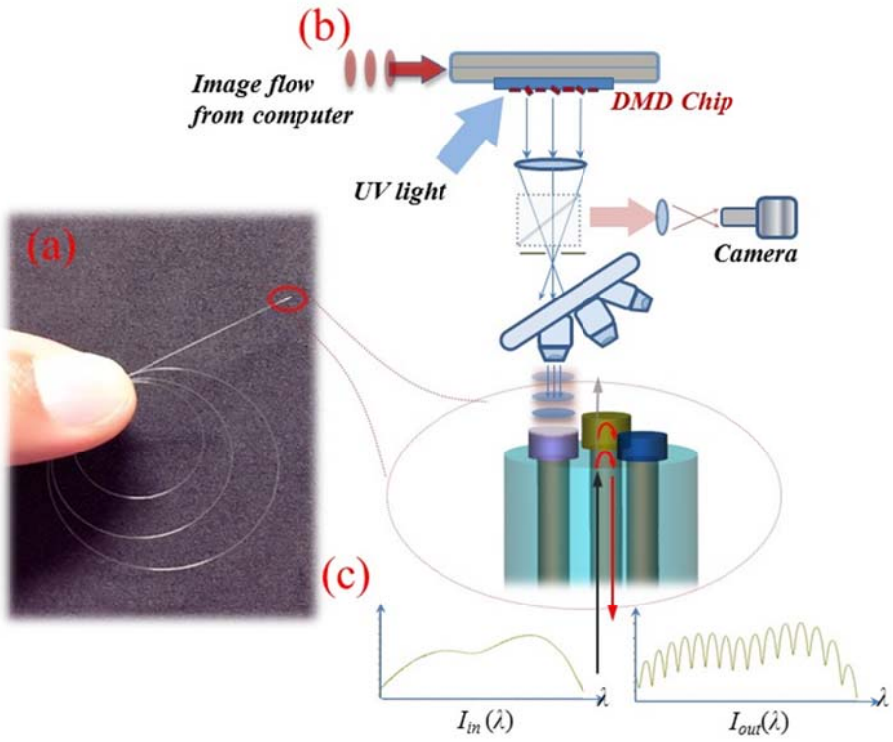

Figure 6.1 In situ printing of fiber-tip CO_2 sensors. (a) Photo of an optical fiber for the printing of fiber-tip CO_2 sensors; (b) scheme of in situ printing technology. (c) Spectra of the input probe light and the output from PAVB FPIs, which indicates the forming of FPIs on the top of fiber.

6.2 Characterization and patterning of the PAVB

6.2.1 Characterization of the PAVB

The synthesis and characterization of PAVB was conducted by our collaborator of Dr. Yuan Jiayin's group in Max Planck Institute of Colloids and Interfaces, Germany. The photo-crosslinkable PAVB was synthesized in two steps following previous method [153]. It started from the polymerization of 1-vinylimidazole in dimethylsulfoxide, and followed by

quaternization with allyl bromide to produce the photo-crosslinkable PIL.

In previous studies, PILs were found to own high CO_2 sorption capacity [154-159], and the anions contained in the PILs have some effects on their CO_2 sorption property. Thus, in our study, we characterized the CO_2 sorption property of the photo-crosslinked PAVB at 273 K using Quadrasorb and Autosorb 1-MP machines (Quantachrome Instruments). Isosteric heats of sorption of CO_2 were plotted using the AS1Win software (Quantachrome Instruments). Prior to the sorption experiments, all the samples were degassed overnight at 363 K under dynamic vacuum system. Besides, high-purity gases were utilized in all measurements.

The measured sorption and desorption isotherms are shown in **Figure 6.2**, collected through pressure increasing and dumping cycles with various highest CO_2 pressures, i.e. 0.3, 0.6, 0.9, and 1.0 bar. One can see that the sorption of CO_2 normally rises when CO_2 pressure increases. In terms of 0.3 and 0.6 bar (maximum pressure), the sorption and desorption isotherms depend nearly linearly on the CO_2 pressure, and the corresponding greatest sorptions are 1.14 and 2.15 cc g^{-1}, respectively. In both cases, hysteresis phenomena are observed, which demonstrates that the sorption of CO_2 in PAVB is a result of both physisorption and chemisorption. For maximum pressure of 0.9 and 1.0 bar, the measured greatest sorptions are 4.81 and 6.99 cc g^{-1}, respectively. Under the conditions of these higher pressures, the

hysteresis effects turn out to be more obvious and the hysteresis loops stay open when the CO_2 pressure come back to zero (after an entire pressure increasing and dumping cycle). The outcomes uncover that PAVB is a qualified functional polymer for the development of CO_2 sensors owing to its great CO_2 sorption property.

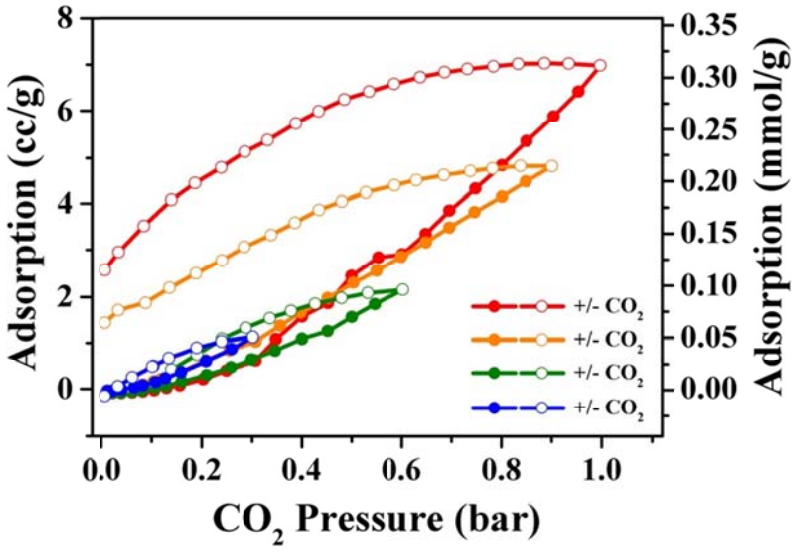

Figure 6.2 Sorption and desorption isotherms of the PAVB. The measurements were repeatedly conducted under maximum CO_2 pressures of 0.3, 0.6, 0.9 and 1.0 bar, respectively.

6.2.2 Optical patterning of the PAVB

Photocrosslinkable PAVB and photoinitiator (Irgacure 2959) were dissolved in DI water. In 2D μ-patterning tests (including the sensor fabrication process), the proportions of the PAVB and Irgacure 2959 were 40 wt% and 3 wt%, respectively, while the proportions of the PAVB and

Irgacure 2959 were 30 wt% and 5 wt%, respectively, in 3D μ-patterning experiments. Firstly, small amounts of the PAVB aqueous solution was dropped on a glass slide with spacers, and afterward a cover glass was put upon the solution. An optical μ-printing system with a UV light source (at the wavelength of 365 nm) and a digital-micromirror device (DMD, DLi4120 0.7" XGA, Texas Instruments), as shown in Figure 6.1, has been utilized to optically pattern the own-synthesized PAVB solution. The pre-designed microstructures were converted into image data and then loaded onto the DMD chip for generation of optical patterns. UV light (365 nm) penetrated the cover glass and crosslinked the PILs on the bottom side of the cover glass, forming the predesigned microstructures after developing.

Figure 6.3 shows images of the fabricated PAVB microstructures, taken with a laser scanning confocal microscope (VK-X200, KEYENCE, Japan). **Figure 6.3(a)** and **Figure 6.3(b)** are the logos of The Hong Kong Polytechnic University (PolyU) and Max Planck Institute (MPI), our collaborative partner. It can be seen that both the simple and complex 2D microstructures can be fabricated precisely in very short time (around 10 s) under a UV intensity of 96.89 mW cm^{-2}. 3D microstructures can also be fabricated using the PAVB solution. **Figure 6.3(c)** and **Figure 6.3(d)** show some fabricated PAVB micro-nozzle and micro-flower arrays, in which data

of the sliced images of the 3D models has been used for a layer-by-layer optical exposure process. As the 3D microstructures were fabricated using a layer-by-layer polymerization process, it took longer time (30 s) under a UV intensity of 160.33 mW cm^{-2}, compared with 2D patterns. Both the 2D and 3D microstructures were developed in EtOH for around 7 min. More details of the PAVB micro-flower structures are provided in **Figure 6.4**. It can be seen that the heights of the center and petal parts are 3.96 μm and 5.12 μm, respectively, and the period of the micro-flower array is 60.28 μm.

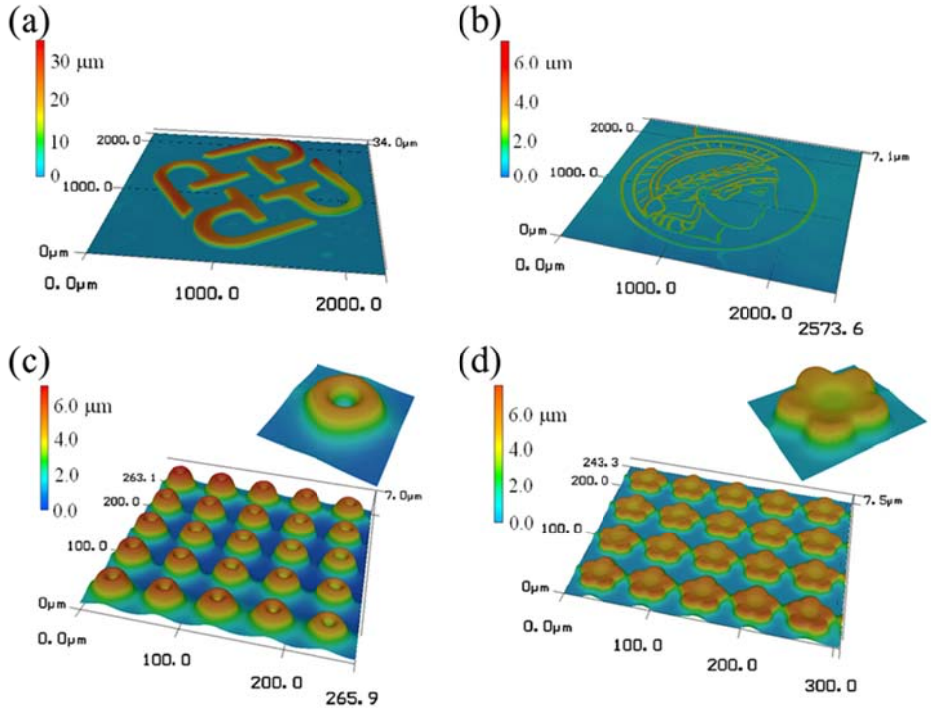

Figure 6.3 Laser scanning confocal images of PAVB microstructures. (a) PolyU logo, (b) MPI logo, (c) micro-nozzle array, and (d) micro-flower array.

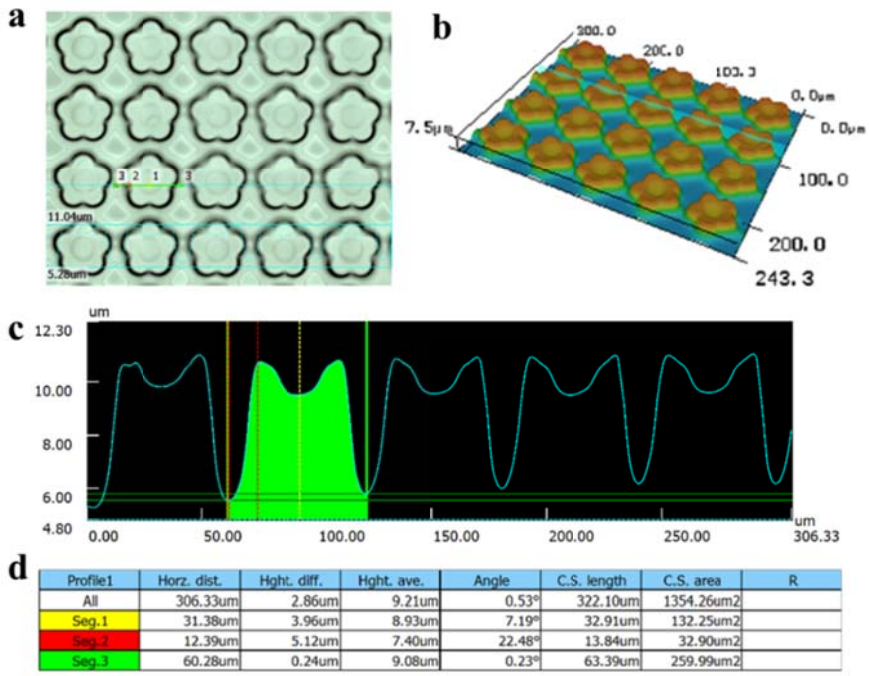

Profile1	Horz. dist.	Hght. diff.	Hght. ave.	Angle	C.S. length	C.S. area	R
All	306.33um	2.86um	9.21um	0.53°	322.10um	1354.26um2	
Seg.1	31.38um	3.96um	8.93um	7.19°	32.91um	132.25um2	
Seg.2	12.39um	5.12um	7.40um	22.48°	13.84um	32.90um2	
Seg.3	60.28um	0.24um	9.08um	0.23°	63.39um	259.99um2	

Figure 6.4 Laser scanning confocal image and its profile parameters of the fabricated PAVB microflower array.

With a deliberately designed micro-square testing pattern, the feature size of PAVB microstructures under our optical in-situ μ-printing system was measured to be 5.5 μm, as shown in **Figure 6.5**. Although the feature size is related to both the properties of the materials and the resolution of the optical in-situ μ-printing system, the feature size is limited by the soft and high-fluidity nature of the PAVB material in this case.

To fabricate PAVB FPIs, PAVB solution was deposited on the end faces of optical fibers using a dip-coating method. The light intensity and total exposure time of the optically μ-printing process were 96.89 mW cm^{-2} and 30 s, respectively.

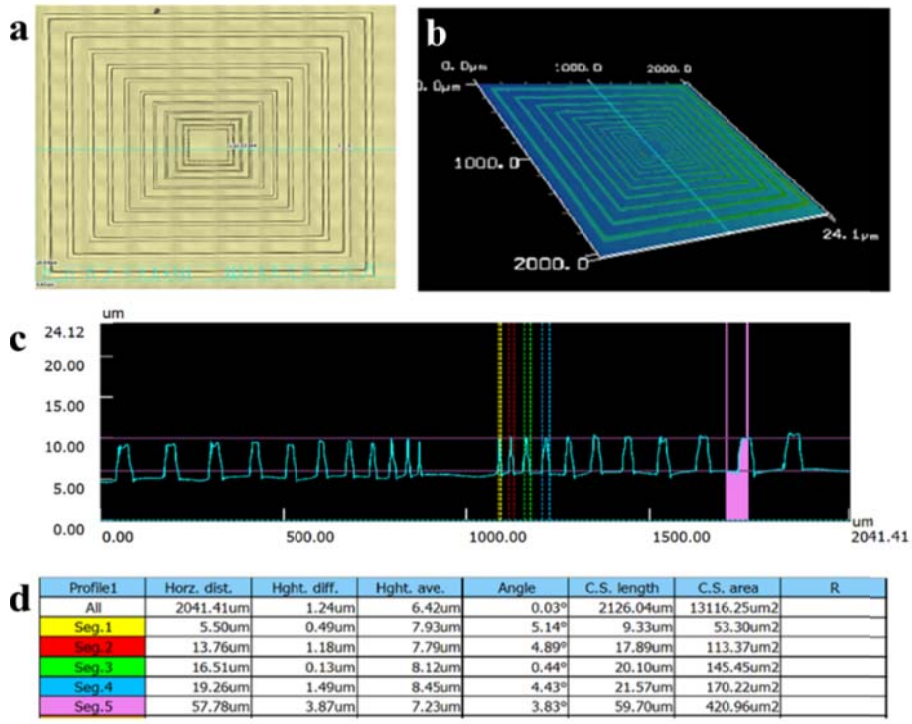

Profile1	Horz. dist.	Hght. diff.	Hght. ave.	Angle	C.S. length	C.S. area	R
All	2041.41um	1.24um	6.42um	0.03°	2126.04um	13116.25um2	
Seg.1	5.50um	0.49um	7.93um	5.14°	9.33um	53.30um2	
Seg.2	13.76um	1.18um	7.79um	4.89°	17.89um	113.37um2	
Seg.3	16.51um	0.13um	8.12um	0.44°	20.10um	145.45um2	
Seg.4	19.26um	1.49um	8.45um	4.43°	21.57um	170.22um2	
Seg.5	57.78um	3.87um	7.23um	3.83°	59.70um	420.96um2	

Figure 6.5 Laser scanning confocal image and its profile parameters of the fabricated concentric PAVB micro-squares.

6.3 *In situ* μ-printed optical fiber-top CO_2 sensors

6.3.1 *In situ* printed optical fiber-top polymer FPIs

The good processability of the PAVB has been demonstrated in previous section, which makes it a promising photolithographic material for CO_2 sensing. As the optical fiber tip is a unique and tiny platform with inherent light-guiding property [160-164], we here in situ printed PAVB on the end face of a multicore optical fiber to fabricate miniature optical fiber-tip FPI sensors. Different kinds of FPIs can be directly and in situ fabricated on the end faces of optical fibers. **Figure 6.6(a)** and **Figure 6.6(c)** show the SEM

images of polymer FPIs fabricated on a standard single-mode fiber and a multicore fiber, respectively. As we can see, the surfaces of the polymer FPIs are smooth, leading to high reflectivity of the incident light at the polymer/air interfaces. **Figure 6.6(b)** shows the measured reflection spectrum and its FFT results, where the FSR of the reflective spectrum is about 17.67 μm. After the FFT calculation and Lorentzian fitting, the length of the PAVB interferometer can be calculated to be 42.21 μm, which agrees well with the values measured in an optical microscope image.

In order to accomplish a miniature fiber-optic CO_2 sensor, we fabricated three optical interferometric sensors on the top face of a multicore optical fiber for simultaneous measurement of CO_2 and temperature. **Figure 6.6(c)** shows the false-color SEM images of fabricated miniature fiber-optic CO_2 sensors. The two longer interferometers were fabricated using the PAVB, while the shorter one was made of commercial SU-8 epoxy resin. The material proportion and fabrication conditions for the SU-8 FPI are the same as the previous work [165]. The three polymer FPIs were fabricated on the top face of a multicore fiber in two separate cycles, and the PAVB FPIs were first fabricated. Since the parameters of the two PAVB interferometers are almost the same, just one single reflection fringe of PAVB FPIs is displayed in **Figure 6.6(d)**. The FSRs of the reflection spectra of the PAVB and SU-8 interferometers fabricated on

the multicore optical fiber are 14.01 μm and 33.25 μm, and the corresponding lengths of the two interferometers are 53.78 μm and 22.08 μm, respectively. These results indicate that we can simultaneously fabricate FPIs of different materials on the top face of a multicore optical fiber to develop multifunctional sensors.

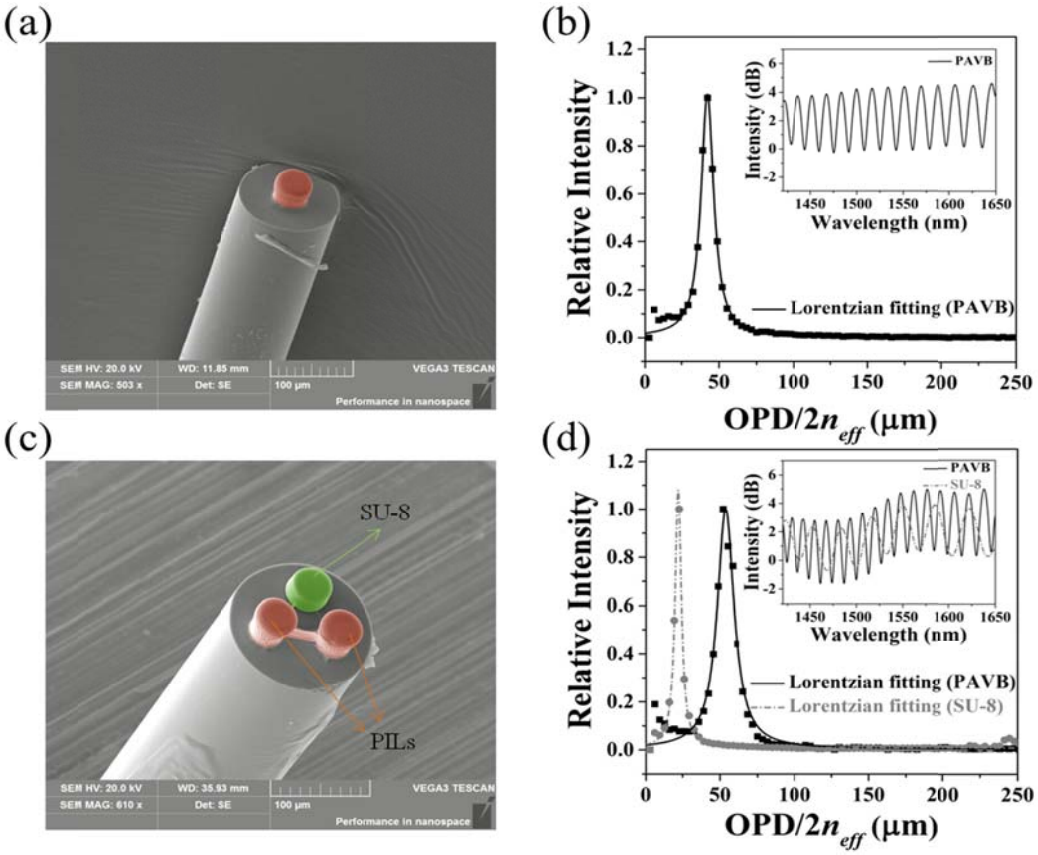

Figure 6.6 SEM images and spectral characteristics of the fabricated fiber-top polymer FPIs. (a) SEM image of the PAVB FPI sensor fabricated on a SMF. (b) Measured reflection spectrum (inset) and its corresponding FFT result. (c) SEM image of the PAVB and SU-8 FPI sensors fabricated on the end face of a multicore optical fiber. (d) Measured reflection spectrum (inset) and its corresponding FFT result.

6.3.2 Testing of the optical fiber-tip CO_2 sensors

The schematic of the experimental setup for the testing of the fiber-optic CO_2 sensor is shown in **Figure 6.7**, where a stainless-steel gas chamber was utilized to seal the fiber-optic FPI CO_2 sensor. The CO_2 gas mixtures of various concentrations were prepared by mixing pure CO_2 gas with pure nitrogen at different flow-rate proportions at atmospheric pressure through two flow regulators. The gas mixture flowed into the cylinder chamber at a fixed speed in all the tests. A multicore fiber fan-in/out device was used to couple light into and out of the multicore fiber. The reflection spectra of the fiber-optic CO_2 sensors were measured by an optical spectrum analyzer (AQ6370, YOKOGAWA, Japan) with a resolution of 0.02 nm.

It is known that the wavelength shift $\Delta\lambda$ of the interference fringe of a fiber-optic FPI is

$$\Delta\lambda = 4\pi\left(n_{eff}l\right)/\phi_b, \tag{6.1}$$

where $\Delta(n_{eff}\, l)$ and ϕ_b are the change of optical path length and the phase bias of specific interference peak or valley, respectively [53, 166-168]. FPI can convert molecular interactions between the polymer and the exposed gas into a change of RI, which will be translated to changes in the phase-matching conditions of the FP resonance. In the existence of CO_2 gas, the PAVB FPI will absorb the CO_2 molecules, both physically and chemically, which will result in an increase of the effective RI of PAVB

polymer and a red shift of the resonant wavelength in the reflection spectrum. The influence of the cavity-length change is negligible in our case upon sorption of CO_2 gas.

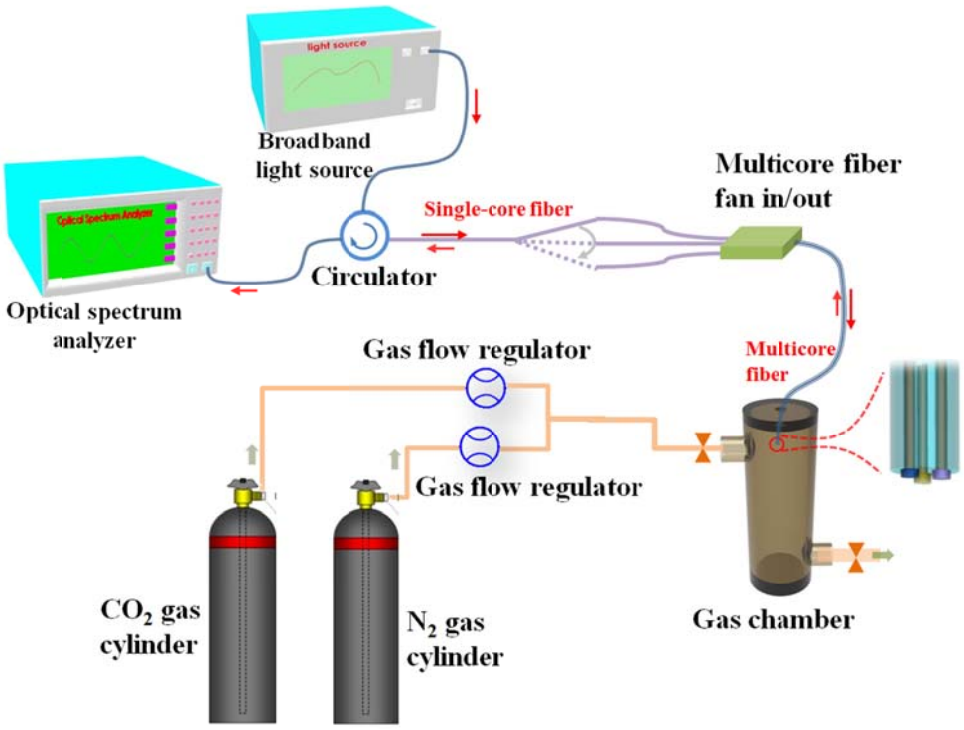

Figure 6.7 The schematic of the experimental setup for the testing of the fiber-optic CO_2 sensor.

Figure 6.8 shows the response of fiber-optic CO2 sensor to CO2 gas of different concentrations. It can be seen in Figure 6.8(a) that the peak wavelength of the PAVB FPI increases with loading CO2 gas and decreases with unloading it, while the SU-8 FPI shows almost no response. The PAVB FPI shows good reversibility with increasing and decreasing of the concentrations of CO2 gas, with a little hysteresis. The sensitivity of the sensor is 34.92 pm/vol%, according to a linear regression. Moreover, the

sensor can detect wide range concentration of CO2 gas from 0 vol% to 75 vol%, which makes it useful in many fields. The little hysteresis in the CO_2 response test is attributed to several reasons: 1) a total amount of 150 mg PAVB was used for the measurement of isotherms, while the mass of PAVB used in the fabrication of single fiber-tip FPI sensor is around 0.11 μg only; 2) PAVB was put in a camber with 100 vol% CO_2 to measure isotherms, where the concentration of CO_2 for testing of the sensors was from 0 vol% to 75 vol% only; 3) Enough long time (i.e. 10 minutes) has been used for the measurement of two adjacent points in the testing of the sensor. The dynamic response of the sensor is shown in **Figure 6.8(b)**. The results reveal that the fiber-optic polymer FP sensor has a very fast response to CO_2. The rise and fall time of the sensor's dynamic response are 6.1 min and 8.0 min, respectively. It is much faster than other PIL-based CO_2 sensors [169], owing to the micrometer-scale size of the microsensor achieved by μ-patterning technique.

As temperature is a key parameter in real applications, the temperature response of the sensor is also studied. The results in **Figure 6.9** suggest that the PAVB sensor has an obvious response to the temperature change due to its high thermooptic coefficient, while the SU-8 FPI shows a smaller sensitivity to the environmental temperature. Both the PAVB and SU-8 FPIs show a linear response to temperature change with sensitivities of

0.704 nm/°C and 0.059 nm/°C, respectively. So the SU-8 FPI can be used to calibrate the influence of environmental temperature. **Figure 6.9(b)** shows the dynamic response of the PAVB FPI sensor to the change of temperature, in which the measured dynamic rise and fall time of the sensor are 2.12 and 2.95 min, respectively.

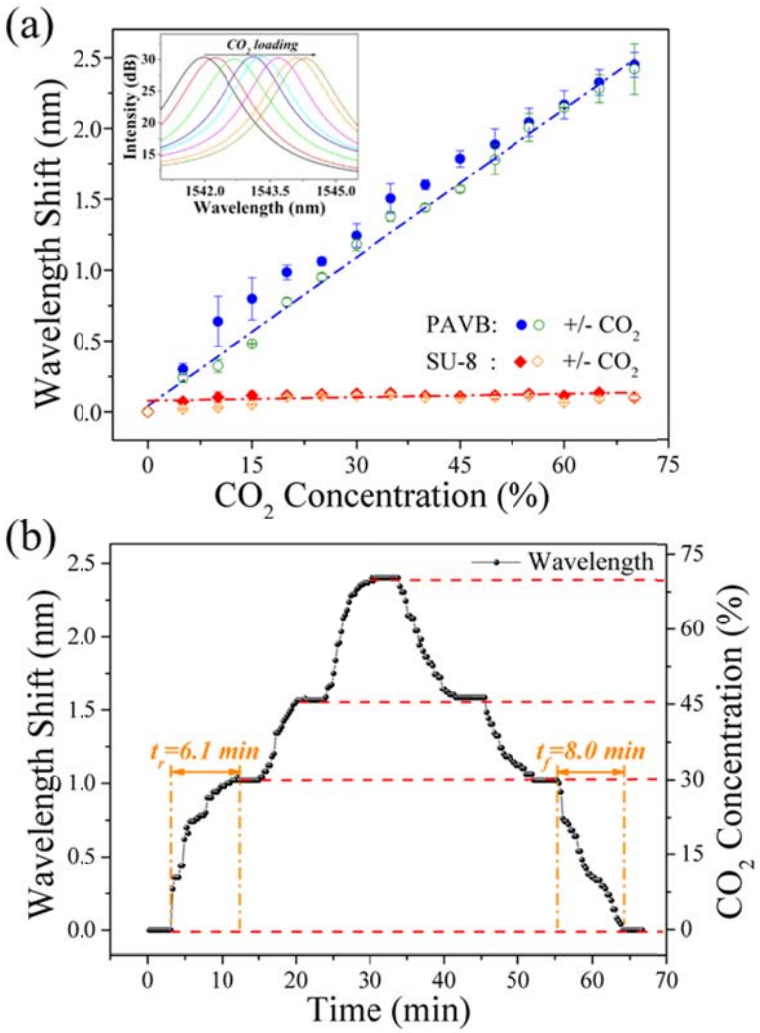

Figure 6.8 Responses of the fabricated optical fiber-tip CO_2 sensor to the change of CO_2 concentrations. (a) Reponses of the PAVB and SU-8 FPI sensors to the loading and unloading of CO_2 gas. The inset shows the shift of the spectral peak of the PAVB FPI sensor. (b) Dynamic response of the PAVB FPI sensor to the change of CO_2 concentration.

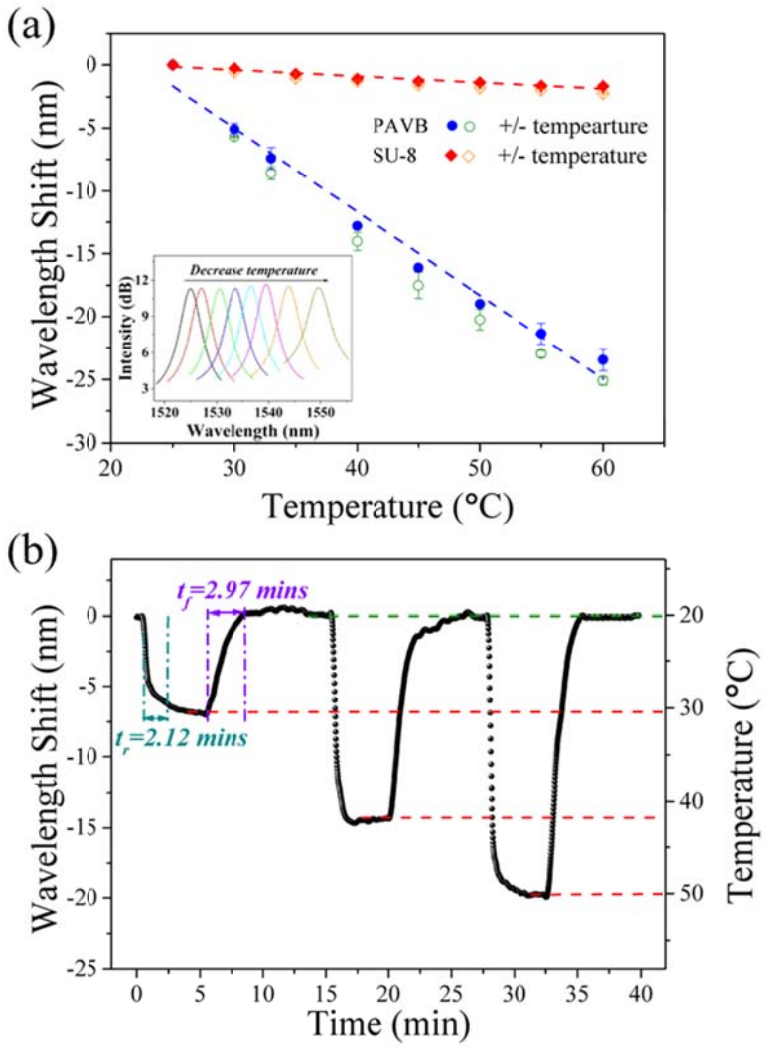

Figure 6.9 Responses of the fabricated optical fiber-tip CO_2 sensor to the change temperature. (a) Responses of the PAVB and SU-8 FPI sensors to the change of temperature. The inset shows the shift of the spectral peak of the PAVB FPI sensor. (b) Dynamic response of the PAVB FPI sensor to the change of temperature.

6.3.3 Discussion

Microengineering of functional polymer has turned into an extremely

appealing way to develop new microdevices and sensors. In this work, we developed an in situ optical μ-printing technology to process photocrosslinkable PAVB to develop a fiber-optic CO_2 sensor. It is revealed that CO_2 had larger polarizability and quadrupole momentum than other common gases in atmosphere, e.g. N_2 and O_2 [170]. As PAVB is an imidazolium-based polycation, CO_2 can be effectively polarized in PAVB. Meantime, the cation groups in PAVB and their sp3 hybridizations can be promptly rearranged into various configurations for CO_2 gas sorption [171]. Besides, CO_2 gas can weakly react with the imidazolium rings in the main chain [158]. All these interactions give PAVB an excellent CO_2 sorption capacity and selectivity. In addition, compared to other polymers containing amino groups for CO_2 detecting [172, 173], PAVB won't generate toxic carbamates.

In spite of the fact that the limit of detection (LOD) of a fiber-optic sensor normally relies upon the overall performance of both the sensor and the signal interrogation system, it is worthy of finding a rough estimation of such a limit for comparison with other sensors. It is known that the LOD can be estimated by using $LOD=3S_a/b$, where S_a is the standard deviation of the response and b is the slope of the calibration curve. As the standard deviation is calculated from the linear regression to be 9.9 pm, the LOD is estimated to be around 0.85 vol%. This value is lower than the previously

reported PIL-based CO_2 sensors [169], especially the one using PIL-wrapped single-walled carbon nanotubes (SWCNTs), whose detection limit is 50 ppb [174]. However, such a CO_2 sensor need utilized without the existence of oxygen and saturates at 50 ppm. While our optical fiber-tip CO_2 sensor has a wide detection range from 0 vol% to 75 vol%, which is highly desired for many practical applications such as coal mine safety monitoring and food quality control.

The sensing optical fiber used in our work is a seven-core optical fiber. In spite of the fact that we utilized just three cores of the optical fiber to fabricate two types of polymer FPIs for simultaneous detection of CO_2 and temperature, the previously mentioned technique can be employed to integrate more kinds of functional polymers to detect an number of parameters, for example, humidity or other gas components. Combined with the remote-control ability and small size of optical fiber, our PAVB-based fiber-optic CO_2 sensor shows great potential in the areas of healthy monitoring and intelligent food quality control.

6.4 Summary

In summary, a photo-crosslinkable PIL was synthesized and used as a negative resist to create complex patterns. Both 2D and 3D PAVB micropatterns with high resolution were rapidly fabricated by the

own-developed optical in-situ μ-printing system. With the novel optical printing technology, PAVB and SU-8 FPIs were fabricated on the end faces of miniature optical fibers for simultaneous measurement of CO_2 concentration and temperature. The PAVB based CO_2 microsensor shows very fast response, wide detection range. Thus, it shows great potential in areas of healthy monitoring, safety control in mines and intelligent food quality control.

Chapter 7

Conclusions and Future Outlook

7.1 Conclusions

In this thesis, optical μ-printing technologies have been developed to fabricate three kinds of polymer microphotonic devices, including polymer optical WGM resonators, fiber-tip pressure sensors, and fiber-tip CO_2 sensors. Compared to conventional photomask-based lithography technologies, the developed optical μ-printing technologies based on maskless exposure approach can not only offer new pathways for device design and fabrication but also significantly reduce the cost and time for prototyping and optimization (as the photomasks used in mask-based exposure technologies are usually expensive and need long lead time).

Firstly, the 3D microfabrication capability of the developed optical μ-printing technologies has been demonstrated by rapid fabrication of polymer suspended-disk WGM resonators and resonator arrays. The WGMs in the fabricated polymer resonators were excited by using optical fiber tapers. The quality factors and free spectral ranges of the fabricated resonators were calculated according to the measured transmission spectra.

The mode distributions and resonant wavelengths of the optical WGM resonators were analyzed by using software COMSOL. The polymer WGM resonators are promising in the applications such as refractive index sensing and biosensors.

Secondly, the in-situ microfabrication capacity of optical μ-printing technologies has been demonstrated by the fabrication of microscale polymer FPIs with sealed air cavities on the end faces of SMFs for pressure sensing. In the fabrication process, SU-8 suspended diaphragms were directly printed by using a dynamic optical exposure technology and then were further enclosed by a following in-situ μ-printing process to form sealed air cavities. FP interferometric fringes in the reflection spectra were recorded for pressure measurement. The sensing performance of the fiber-tip pressure microsensor was investigated using an own-developed testing setup. A 3D model was built and utilized to analyze the deformation using the structural mechanics module of commercial software COMSOL. The simulated results agree well with the measured data and reveal that the fiber-tip pressure can achieve much higher sensitivity with a thinner SU-8 diaphragm.

Finally, optical in situ μ-printing technology has been applied to process functional polymer materials, i.e. poly(1-allyl-3-vinylimidazolium bromide) (PAVB), to develop fiber-tip CO_2 sensors. The optical in situ

μ-printing technology enables to process CO_2 sensitive PAVB on the tiny surface area of optical fiber to fabricate micrometer-scale FPI microsensors. As the PAVB FPI sensors were also sensitive to the temperature of the surrounding environment, another SU-8 FPI was fabricated on the same end face of the multicore fiber as a reference temperature microsensor. The polymer microphotonic CO_2 sensors show a linear response to the change of CO_2 concentration in the range of 0 vol% to 75 vol%. Such a tiny fiber-tip CO_2 sensor is very appealing in widespread applications ranging from industrial waste gas detection to food quality control.

7.2 Future Outlook

In this thesis, three kinds of polymer microphotonic sensors, with the common advantages of rapid fabrication, miniature size and high sensitivity, have been successfully fabricated and intensively investigated.. Several outlooks for future investigation are given as follows:

1) The Q values of polymer WGM resonators can be improved from different aspects. First, the material-absorption limited Q can be further improved if another polymer material with lower absorption coefficient can be used for the WGM resonator fabrication. Second, the geometric parameters and exposure parameters can be further optimized to improve the waveguide property of the WGM resonators. Third, some

post-processing techniques, e.g. thermal reflow or post dip-coating, can be applied to further smoothen the surface of the polymer WGM resonators. Last, the potential contamination of the fabricated WGM resonators can be alleviated if the experiments are conducted in a cleanroom environment.

2) Optical fiber-tip pressure sensor with an open FP cavity can be developed to extend the measurement range of the closed-cavity optical fiber-tip pressure sensor demonstrated in Chapter 5. Owning to the limit of mechanical strength, optical fiber-tip FPI pressure sensor with closed air-cavity has limited maximum bearing pressure. One of potential solutions to the problem is to use an open-cavity optical fiber-tip pressure sensor. When the pressure of the surrounding gas or liquid increases, the RI of the gas or liquid will rise accordingly. Therefore, the resonant wavelength in the reflection spectrum of the fiber-tip FPI will shift towards the longer wavelength, which can thus be used for monitoring the pressure. The pressure sensitivity of such open-cavity optical fiber-tip pressure sensor can be expressed as:

$$\frac{d\lambda_m}{dP} = \frac{d\lambda_m}{dn} \cdot \frac{dn}{dP} = \frac{\lambda_m}{n} \cdot \frac{dn}{dP}, \tag{7.1}$$

where dn/dP is the coefficient of the RI of the gas or liquid related to its pressure, λ_m is the resonant wavelength of the FPI, n is the RI of the gas or liquid and P is the pressure.

3) More fiber-tip sensors can be developed through printing different

functional polymer materials on the end face of optical fibers. The sensing performance of the fiber-tip sensors demonstrated in Chapter 6 depends very much on the selective CO_2 sorption properties of the photocrosslinkable poly(1-allyl-3-vinylimidazolium bromide) (PAVB). Similar process can be applied to process a wide range of functional materials for sensor fabrication. For example, as a pH responsive hydrogel, poly(acrylic acid) can be used to develop pH sensor; as a thermal responsive hydrogel, poly(N-isopropyl acrylamide) can be adopted to fabricate miniature temperature sensors.

References

[1] D. Yuan, Y. Dong, Y. Liu, and T. Li, "Mach-zehnder interferometer biochemical sensor based on silicon-on-insulator rib waveguide with large cross section," Sensors **15**, 21500-21517 (2015).

[2] A. Ymeti, J. Greve, P. V. Lambeck, T. Wink, S. W. van Hövell, T. A. Beumer, R. R. Wijn, R. G. Heideman, V. Subramaniam, and J. S. Kanger, "Fast, ultrasensitive virus detection using a young interferometer sensor," Nano Letters **7**, 394-397 (2007).

[3] D. Duval, and L. M. Lechuga, "Optical waveguide biosensors," Photonics: Scientific Foundations, Technology and Applications, IV; Andrews, DL, Ed, 323-365 (2015).

[4] H. J. Watts, C. R. Lowe, and D. V. Pollard-Knight, "Optical biosensor for monitoring microbial cells," Analytical Chemistry **66**, 2465-2470 (1994).

[5] M. Zourob, S. Mohr, B. J. T. Brown, P. R. Fielden, M. B. McDonnell, and N. J. Goddard, "An integrated optical leaky waveguide sensor with electrically induced concentration system for the detection of bacteria," Lab on a Chip **5**, 1360-1365 (2005).

[6] K. D. Heylman, K. A. Knapper, E. H. Horak, M. T. Rea, S. K. Vanga, and R. H. Goldsmith, "Optical Microresonators for Sensing and

Transduction: A Materials Perspective," Advanced Materials **29** (2017).

[7] M. Weisser, G. Tovar, S. Mittler-Neher, W. Knoll, F. Brosinger, H. Freimuth, M. Lacher, and W. Ehrfeld, "Specific bio-recognition reactions observed with an integrated Mach–Zehnder interferometer," Biosensors and Bioelectronics **14**, 405-411 (1999).

[8] R. Heideman, and P. Lambeck, "Remote opto-chemical sensing with extreme sensitivity: design, fabrication and performance of a pigtailed integrated optical phase-modulated Mach–Zehnder interferometer system," Sensors and Actuators B: Chemical **61**, 100-127 (1999).

[9] B. H. Schneider, J. G. Edwards, and N. F. Hartman, "Hartman interferometer: versatile integrated optic sensor for label-free, real-time quantification of nucleic acids, proteins, and pathogens," Clinical Chemistry **43**, 1757-1763 (1997).

[10] T. Kippenberg, S. Spillane, and K. Vahala, "Kerr-nonlinearity optical parametric oscillation in an ultrahigh-Q toroid microcavity," Physical Review Letters **93**, 083904 (2004).

[11] A. A. Savchenkov, V. S. Ilchenko, A. B. Matsko, and L. Maleki, "High-order tunable filters based on a chain of coupled crystalline whispering gallery-mode resonators," IEEE Photonics Technology Letters **17**, 136-138 (2005).

[12] M. R. Foreman, J. D. Swaim, and F. Vollmer, "Whispering gallery mode sensors," Advances in Optics and Photonics **7**, 168 (2015).

[13] A. Barucci, F. Baldini, S. Berneschi, F. Cosi, A. Giannetti, G. N. Conti, S. Soria, S. Tombelli, C. Trono, D. Farnesi, S. Pelli, G. C. Righini, L. Lunelli, L. Pasquardini, and C. Pederzolli, "Whispering Gallery Modes Microresonators for Sensing and Biosensing Applications," Sensors **319**, 183-186 (2015).

[14] T. Wienhold, S. Kraemmer, S. F. Wondimu, T. Siegle, U. Bog, U. Weinzierl, S. Schmidt, H. Becker, H. Kalt, T. Mappes, S. Koeber, and C. Koos, "All-polymer photonic sensing platform based on whispering-gallery mode microgoblet lasers," Lab on a Chip **15**, 3800-3806 (2015).

[15] A. Bianchetti, A. Federico, S. Vincent, S. Subramanian, and F. Vollmer, "Refractometry-based air pressure sensing using glass microspheres as high-Q whispering-gallery mode microresonators," Optics Communications **394**, 152-156 (2017).

[16] L. Labrador-Páez, K. Soler-Carracedo, M. Hernández-Rodríguez, I. R. Martín, T. Carmon, and L. L. Martin, "Liquid whispering-gallery-mode resonator as a humidity sensor," Optics Express **25**, 1165-1172 (2017).

[17] T. Reynolds, N. Riesen, A. Meldrum, X. D. Fan, J. M. M. Hall, T. M. Monro, and A. Francois, "Fluorescent and lasing whispering gallery mode microresonators for sensing applications," Laser & Photonics Reviews **11** (2017).

[18] X. D. Wang, and O. S. Wolfbeis, "Fiber-Optic Chemical Sensors and Biosensors (2013-2015)," Analytical Chemistry **88**, 203-227 (2016).

[19] O. S. Wolfbeis, "Fiber optic chemical sensors and biosensors," Analytical Chemistry **72**, 81r-89r (2000).

[20] A. N. Oraevsky, "Whispering-gallery waves," Quantum Electronics **32**, 377-400 (2002).

[21] D. K. Armani, T. J. Kippenberg, S. M. Spillane, and K. J. Vahala, "Ultra-high-Q toroid microcavity on a chip," Nature **421**, 925-928 (2003).

[22] A. B. Matsko, and V. S. Ilchenko, "Optical resonators with whispering-gallery modes - Part I: Basics," IEEE Journal Of Selected Topics In Quantum Electronics **12**, 3-14 (2006).

[23] S. Yang, Y. Wang, and H. Sun, "Advances and Prospects for Whispering Gallery Mode Microcavities," Advanced Optical Materials **3**, 1136-1162 (2015).

[24] R. Richtmyer, "Dielectric resonators," Journal Of Applied Physics **10**, 391-398 (1939).

[25] J. C. Knight, G. Cheung, F. Jacques, and T. A. Birks, "Phase-matched excitation of whispering-gallery-mode resonances by a fiber taper," Optics Letters **22**, 1129-1131 (1997).

[26] V. A. Sychugov, V. P. Torchigin, and M. Y. Tsvetkov, "Whispering-gallery waves in optical fibres," Quantum Electronics **32**, 738-742 (2002).

[27] M. N. Zervas, G. S. Murugan, and J. S. Wilkinson, "Whispering Gallery Modes in Bottle Microresonators," Icton: 2009 11th International Conference on Transparent Optical Networks, Vols 1 and 2, 1120-1123 (2009).

[28] U. Bog, F. Brinkmann, H. Kalt, C. Koos, T. Mappes, M. Hirtz, H. Fuchs, and S. Köber, "Large‐Scale Parallel Surface Functionalization of Goblet‐type Whispering Gallery Mode Microcavity Arrays for Biosensing Applications," Small **10**, 3863-3868 (2014).

[29] T. Beck, M. Hauser, T. Grossmann, D. Floess, S. Schleede, J. Fischer, C. Vannahme, T. Mappes, and H. Kalt, "PMMA-micro goblet resonators for biosensing applications," in *Frontiers in Biological Detection: From Nanosensors to Systems III*(International Society for

Optics and Photonics, 2011), p. 78880A.

[30] C.-H. Dong, L. He, Y.-F. Xiao, V. Gaddam, S. Ozdemir, Z.-F. Han, G.-C. Guo, and L. Yang, "Fabrication of high-Q polydimethylsiloxane optical microspheres for thermal sensing," Applied Physics Letters **94**, 231119 (2009).

[31] G. Schweiger, and M. Horn, "Effect of changes in size and index of refraction on the resonance wavelength of microspheres," JOSA B **23**, 212-217 (2006).

[32] N. M. Hanumegowda, C. J. Stica, B. C. Patel, I. White, and X. Fan, "Refractometric sensors based on microsphere resonators," Applied Physics Letters **87**, 201107 (2005).

[33] S. Arnold, R. Ramjit, D. Keng, V. Kolchenko, and I. Teraoka, "MicroParticle photophysics illuminates viral bio-sensing," Faraday Discussions **137**, 65-83 (2008).

[34] A. Mazzei, S. Götzinger, L. d. S. Menezes, G. Zumofen, O. Benson, and V. Sandoghdar, "Controlled coupling of counterpropagating whispering-gallery modes by a single Rayleigh scatterer: a classical problem in a quantum optical light," Physical Review Letters **99**, 173603 (2007).

[35] J. Zhu, S. K. Ozdemir, Y.-F. Xiao, L. Li, L. He, D.-R. Chen, and L.

Yang, "On-chip single nanoparticle detection and sizing by mode splitting in an ultrahigh-Q microresonator," Nature Photonics **4**, 46-49 (2009).

[36] C. H. Dong, L. He, Y. F. Xiao, V. R. Gaddam, S. K. Ozdemir, Z. F. Han, G. C. Guo, and L. Yang, "Fabrication of high-Q polydimethylsiloxane optical microspheres for thermal sensing," Applied Physics Letters **94**, 231119 (2009).

[37] H. Wagner, H. Schmitzer, J. Lutti, P. Borri, and W. Langbein, "Effects of uniaxial pressure on polar whispering gallery modes in microspheres," Journal Of Applied Physics **113**, 243101 (2013).

[38] M. R. Foreman, and F. Vollmer, "Optical tracking of anomalous diffusion kinetics in polymer microspheres," Physical Review Letters **114**, 118001 (2015).

[39] Y. Wu, D. Y. Zhang, P. Yin, and F. Vollmer, "Ultraspecific and Highly Sensitive Nucleic Acid Detection by Integrating a DNA Catalytic Network with a Label‐Free Microcavity," Small **10**, 2067-2076 (2014).

[40] R. Bischler, M. Olszyna, M. Himmelhaus, and L. Dähne, "Development of a fully automated in-vitro diagnostics system based on low-Q whispering gallery modes in fluorescent microparticles," The

European Physical Journal Special Topics **223**, 2041-2055 (2014).

[41] X. Q. Wu, and L. M. Tong, "Optical microfibers and nanofibers," Nanophotonics **2**, 407-428 (2013).

[42] L. M. Tong, F. Zi, X. Guo, and J. Y. Lou, "Optical microfibers and nanofibers: A tutorial," Optics Communications **285**, 4641-4647 (2012).

[43] A. Camposeo, F. Di Benedetto, R. Stabile, A. A. R. Neves, R. Cingolani, and D. Pisignano, "Laser Emission from Electrospun Polymer Nanofibers," Small **5**, 562-566 (2009).

[44] F. X. Gu, H. K. Yu, P. Wang, Z. Y. Yang, and L. M. Tong, "Light-Emitting Polymer Single Nanofibers via Waveguiding Excitation," Acs Nano **4**, 5332-5338 (2010).

[45] Q. H. Song, L. Y. Liu, and L. Xu, "Lasing Action in Dye Doped Polymer Nanofiber Knot Resonator," Journal Of Lightwave Technology **27**, 4374-4376 (2009).

[46] F. X. Gu, L. Zhang, X. F. Yin, and L. M. Tong, "Polymer single-nanowire optical sensors," Nano Letters **8**, 2757-2761 (2008).

[47] P. Wang, L. Zhang, Y. N. Xia, L. M. Tong, X. Xu, and Y. B. Ying, "Polymer Nanofibers Embedded with Aligned Gold Nanorods: A New Platform for Plasmonic Studies and Optical Sensing," Nano Letters **12**, 3145-3150 (2012).

[48] B. E. Saleh, M. C. Teich, and B. E. Saleh, *Fundamentals of photonics* (Wiley New York, 1991).

[49] F. J. Arregui, Y. Liu, I. R. Matias, and R. O. Claus, "Optical fiber humidity sensor using a nano Fabry–Perot cavity formed by the ionic self-assembly method," Sensors and Actuators B: Chemical **59**, 54-59 (1999).

[50] M. Li, Y. Liu, S. L. Qu, and Y. Li, "Fiber-optic sensor tip for measuring temperature and liquid refractive index," Optical Engineering **53** (2014).

[51] W. Pulliam, P. Russler, R. Mlcak, K. Murphy, and C. Kozikowski, "Micromachined, SiC fiber optic pressure sensors for high-temperature aerospace applications," Industrial Sensing Systems **4202**, 21-30 (2000).

[52] P. Beard, and T. Mills, "Extrinsic optical-fiber ultrasound sensor using a thin polymer film as a low-finesse Fabry–Perot interferometer," Applied Optics **35**, 663-675 (1996).

[53] G. C. Hill, R. Melamud, F. E. Declercq, A. A. Davenport, I. H. Chan, P. G. Hartwell, and B. L. Pruitt, "SU-8 MEMS Fabry-Perot pressure sensor," Sensors and Actuators A: Physical **138**, 52-62 (2007).

[54] W. Chen, D. Wang, B. Xu, C. Zhao, and H. Chen, "Multimode fiber

tip Fabry-Perot cavity for highly sensitive pressure measurement," Scientific Reports **7** (2017).

[55] C. Y. Chao, W. Fung, and L. J. Guo, "Polymer microring resonators for biochemical sensing applications," IEEE Journal Of Selected Topics In Quantum Electronics **12**, 134-142 (2006).

[56] L. Wang, J. Ren, X. Han, T. Claes, X. Jian, P. Bienstman, R. Baets, M. Zhao, and G. Morthier, "A label-free optical biosensor built on a low-cost polymer platform," Ieee Photonics Journal **4**, 920-930 (2012).

[57] D. G. Girton, S. L. Kwiatkowski, G. F. Lipscomb, and R. S. Lytel, "20ghz Electrooptic Polymer Mach-Zehnder Modulator," Applied Physics Letters **58**, 1730-1732 (1991).

[58] B. Y. Shew, C. H. Kuo, Y. C. Huang, and Y. H. Tsai, "UV-LIGA interferometer biosensor based on the SU-8 optical waveguide," Sensors and Actuators A-physical **120**, 383-389 (2005).

[59] B. Shew, Y. Cheng, and Y. Tsai, "Monolithic SU-8 micro-interferometer for biochemical detections," Sensors and Actuators A: Physical **141**, 299-306 (2008).

[60] M. I. Lapsley, I.-K. Chiang, Y. B. Zheng, X. Ding, X. Mao, and T. J. Huang, "A single-layer, planar, optofluidic Mach–Zehnder interferometer for label-free detection," Lab on a Chip **11**, 1795-1800

(2011).

[61] A. Brandenburg, and R. Henninger, "Integrated optical Young interferometer," Applied Optics **33**, 5941-5947 (1994).

[62] M. Wang, J. Hiltunen, C. Liedert, L. Hakalahti, and R. Myllylä, "An integrated Young interferometer based on UV-imprinted polymer waveguides for label-free biosensing applications," Journal of the European Optical Society-Rapid Publications **7** (2012).

[63] K. E. Zinoviev, A. B. González-Guerrero, C. Domínguez, and L. M. Lechuga, "Integrated bimodal waveguide interferometric biosensor for label-free analysis," Journal Of Lightwave Technology **29**, 1926-1930 (2011).

[64] L. R. Harriott, "Limits of lithography," Proceedings Of The IEEE **89**, 366-374 (2001).

[65] H. Martinsson, T. Sandstrom, A. Bleeker, and J. D. Hintersteiner, "Current status of optical maskless lithography," Journal of Microlithography Microfabrication and Microsystems **4** (2005).

[66] B. Lee, "DMD 101: Introduction to digital micromirror device (DMD) technology," Texas Instruments, Dallas, TX, USA, Rep. no. DLPA008A (2013).

[67] L. J. Hornbeck, "Digital light processingTM for high-brightness,

high-resolution applications," in *Proc. SPIE*(1997), pp. 27-40.

[68] H. Kueck, M. Bollerott, W. Doleschal, A. Gehner, W. Grundke, D. Kunze, R. Melcher, J. Paufler, R. Seltmann, and G. Zimmer, "New system for fast submicron laser direct writing," in *Proc. SPIE*(1995), pp. 506-514.

[69] A. Bertsch, S. Zissi, J. Jezequel, S. Corbel, and J. Andre, "Microstereophotolithography using a liquid crystal display as dynamic mask-generator," Microsystem Technologies **3**, 42-47 (1997).

[70] Y. Lu, and S. Chen, "Direct write of microlens array using digital projection photopolymerization," Applied Physics Letters **92**, 041109 (2008).

[71] G. A. Cirino, S. A. Lopera, A. N. Montagnoli, R. D. Mansano, and L. G. Neto, "Microlens Array Fabricated by Gray-scale Lithography Maskless System," in *Microelectronics Technology and Devices - Sbmicro 2012*, G. Wirth, N. Morimoto, and D. Vasileska, eds. (2012), pp. 339-345.

[72] Y. Q. Gao, S. A. He, N. N. Luo, and Y. F. Rao, "Research on dynamical-gradual greyscale digital mask lithography," Journal Of Modern Optics **58**, 573-579 (2011).

[73] M. L. Gou, X. Qu, W. Zhu, M. L. Xiang, J. Yang, K. Zhang, Y. Q.

Wei, and S. C. Chen, "Bio-inspired detoxification using 3D-printed hydrogel nanocomposites," Nature Communications **5** (2014).

[74] K. Kim, W. Zhu, X. Qu, C. Aaronson, W. R. McCall, S. C. Chen, and D. J. Sirbuly, "3D Optical Printing of Piezoelectric Nanoparticle - Polymer Composite Materials," Acs Nano **8**, 9799-9806 (2014).

[75] K. J. Vahala, "Optical microcavities," Nature **424**, 839-846 (2003).

[76] S. C. Yang, Y. Wang, and H. D. Sun, "Advances and Prospects for Whispering Gallery Mode Microcavities," Advanced Optical Materials **3**, 1136-1162 (2015).

[77] S. M. Spillane, T. J. Kippenberg, and K. J. Vahala, "Ultralow-threshold Raman laser using a spherical dielectric microcavity," Nature **415**, 621-623 (2002).

[78] A. Chiasera, Y. Dumeige, P. Féron, M. Ferrari, Y. Jestin, G. Nunzi Conti, S. Pelli, S. Soria, and G. C. Righini, "Spherical whispering-gallery-mode microresonators," Laser & Photonics Reviews **4**, 457-482 (2010).

[79] D. Farnesi, A. Barucci, G. C. Righini, S. Berneschi, S. Soria, and G. Nunzi Conti, "Optical frequency conversion in silica-whispering-gallery-mode microspherical resonators," Physical Review Letters **112**, 093901 (2014).

[80] S. L. McCall, A. F. J. Levi, R. E. Slusher, S. J. Pearton, and R. A. Logan, "Whispering-gallery mode microdisk lasers," Applied Physics Letters **60**, 289 (1992).

[81] R. Chen, B. Ling, X. W. Sun, and H. D. Sun, "Room temperature excitonic whispering gallery mode lasing from high-quality hexagonal ZnO microdisks," Advanced Materials **23**, 2199-2204 (2011).

[82] F. Lou, M. Yan, L. Thylen, M. Qiu, and L. Wosinski, "Whispering gallery mode nanodisk resonator based on layered metal-dielectric waveguide," Optics Express **22**, 8490-8502 (2014).

[83] L. He, Y. F. Xiao, C. Dong, J. Zhu, V. Gaddam, and L. Yang, "Compensation of thermal refraction effect in high-Q toroidal microresonator by polydimethylsiloxane coating," Applied Physics Letters **93**, 201102 (2008).

[84] J. Su, "Label-Free Single Exosome Detection Using Frequency-Locked Microtoroid Optical Resonators," Acs Photonics **2**, 1241-1245 (2015).

[85] Z. H. Zhou, C. L. Zou, Y. Chen, Z. Shen, G. C. Guo, and C. H. Dong, "Broadband tuning of the optical and mechanical modes in hollow bottle-like microresonators," Optics Express **25**, 4046-4050 (2017).

[86] G. S. Murugan, M. N. Petrovich, Y. Jung, J. S. Wilkinson, and M. N. Zervas, "Hollow-bottle optical microresonators," Optics Express **19**, 20773-20784 (2011).

[87] R. Orghici, P. Lutzow, J. Burgmeier, J. Koch, H. Heidrich, W. Schade, N. Welschoff, and S. Waldvogel, "A microring resonator sensor for sensitive detection of 1,3,5-trinitrotoluene (TNT)," Sensors (Basel) **10**, 6788-6795 (2010).

[88] V. Zamora, P. Lutzow, M. Weiland, and D. Pergande, "Investigation of cascaded SiN microring resonators at 1.3 microm and 1.5 microm," Optics Express **21**, 27550-27557 (2013).

[89] X. Zhang, Z. Li, Y. Sun, and K. Tong, "Simulation of ZnO-coated SOI microring resonant shift response to ethanol and ammonia," Optik - International Journal for Light and Electron Optics **125**, 2752-2755 (2014).

[90] M. Sumetsky, Y. Dulashko, and R. S. Windeler, "Super free spectral range tunable optical microbubble resonator," Optics Letters **35**, 1866-1868 (2010).

[91] M. Sumetsky, Y. Dulashko, and R. S. Windeler, "Optical microbubble resonator," Optics Letters **35**, 898-900 (2010).

[92] P. F. Wang, J. Ward, Y. Yang, X. Feng, G. Brambilla, G. Farrell, and

S. N. Chormaic, "Lead-silicate glass optical microbubble resonator," Applied Physics Letters **106** (2015).

[93] V. R. Dantham, S. Holler, V. Kolchenko, Z. Wan, and S. Arnold, "Taking whispering gallery-mode single virus detection and sizing to the limit," Applied Physics Letters **101** (2012).

[94] D. Keng, X. Tan, and S. Arnold, "Whispering gallery micro-global positioning system for nanoparticle sizing in real time," Applied Physics Letters **105** (2014).

[95] F. Vollmer, and S. Arnold, "Whispering-gallery-mode biosensing: label-free detection down to single molecules," Nature Methods **5**, 591-596 (2008).

[96] F. Sedlmeir, R. Zeltner, G. Leuchs, and H. G. L. Schwefel, "High-Q MgF2 whispering gallery mode resonators for refractometric sensing in aqueous environment," Optics Express **22**, 30934-30942 (2014).

[97] M. Eryurek, Y. Karadag, N. Tasaltin, N. Kilinc, and A. Kiraz, "Optical sensor for hydrogen gas based on a palladium-coated polymer microresonator," Sensors and Actuators B-Chemical **212**, 78-83 (2015).

[98] Q. Ma, L. Huang, Z. Guo, and T. Rossmann, "Spectral shift response of optical whispering-gallery modes due to water vapor adsorption and desorption," Measurement Science and Technology **21**,

115206 (2010).

[99] M. C. Collodo, F. Sedlmeir, B. Sprenger, S. Svitlov, L. J. Wang, and H. G. L. Schwefel, "Sub-kHz lasing of a CaF2 whispering gallery mode resonator stabilized fiber ring laser," Optics Express **22** (2014).

[100] T. J. Kippenberg, S. M. Spillane, D. K. Armani, and K. J. Vahala, "Ultralow-threshold microcavity Raman laser on a microelectronic chip," Optics Letters **29**, 1224-1226 (2004).

[101] V. S. Ilchenko, A. A. Savchenkov, A. B. Matsko, and L. Maleki, "Nonlinear optics and crystalline whispering gallery mode cavities," Physical Review Letters **92** (2004).

[102] A. Schliesser, and T. J. Kippenberg, "Cavity Optomechanics with Whispering-Gallery Mode Optical Micro-Resonators," Advances in Atomic, Molecular, and Optical Physics, Vol 58 **58**, 207-323 (2010).

[103] K. Hyun Kim, G. Bahl, W. Lee, J. Liu, M. Tomes, X. Fan, and T. Carmon, "Cavity optomechanics on a microfluidic resonator with water and viscous liquids," Light: Science & Applications **2**, e110 (2013).

[104] H. Lee, T. Chen, J. Li, K. Y. Yang, S. Jeon, O. Painter, and K. J. Vahala, "Chemically etched ultrahigh-Q wedge-resonator on a silicon chip," Nature Photonics **6**, 369-373 (2012).

[105] P. Rabiei, W. H. Steier, C. Zhang, and L. R. Dalton, "Polymer

micro-ring filters and modulators," Journal Of Lightwave Technology **20**, 1968-1975 (2002).

[106] A. L. Martin, D. K. Armani, L. Yang, and K. J. Vahala, "Replica-molded high-Q polymer microresonators," Optics Letters **29**, 533-535 (2004).

[107] T. Grossmann, M. Hauser, T. Beck, C. Gohn-Kreuz, M. Karl, H. Kalt, C. Vannahme, and T. Mappes, "High-Q conical polymeric microcavities," Applied Physics Letters **96**, 013303 (2010).

[108] A. P. Zhang, X. Qu, P. Soman, K. C. Hribar, J. W. Lee, S. C. Chen, and S. L. He, "Rapid Fabrication of Complex 3D Extracellular Microenvironments by Dynamic Optical Projection Stereolithography," Advanced Materials **24**, 4266-+ (2012).

[109] H. G. L. Schwefel, A. D. Stone, and H. E. Tureci, "Polarization properties and dispersion relations for spiral resonances of a dielectric rod," Journal Of The Optical Society Of America B-optical Physics **22**, 2295-2307 (2005).

[110] M. Oxborrow, "Traceable 2-D finite-element simulation of the whispering-gallery modes of axisymmetric electromagnetic resonators," IEEE Transactions On Microwave Theory and Techniques **55**, 1209-1218 (2007).

[111] V. B. Braginsky, M. L. Gorodetsky, and V. S. Ilchenko, "Quality-Factor and Nonlinear Properties of Optical Whispering-Gallery Modes," Physics Letters A **137**, 393-397 (1989).

[112] S. M. Spillane, T. J. Kippenberg, O. J. Painter, and K. J. Vahala, "Ideality in a fiber-taper-coupled microresonator system for application to cavity quantum electrodynamics," Physical Review Letters **91** (2003).

[113] O. Tohyama, M. Kohashi, M. Sugihara, and H. Itoh, "A fiber-optic pressure microsensor for biomedical applications," Sensors and Actuators A-physical **66**, 150-154 (1998).

[114] H. N. Li, D. S. Li, and G. B. Song, "Recent applications of fiber optic sensors to health monitoring in civil engineering," Engineering Structures **26**, 1647-1657 (2004).

[115] W. J. Pulliam, P. M. Russler, and R. S. Fielder, "High-temperature high-bandwidth fiber optic MEMS pressure-sensor technology for turbine engine component testing," in *Proc. SPIE*(2002), pp. 229-238.

[116] A. D. Kersey, "Optical fiber sensors for permanent downwell monitoring applications in the oil and gas industry," Ieice Transactions On Electronics **E83c**, 400-404 (2000).

[117] W. Yuan, F. Wang, A. Savenko, D. H. Petersen, and O. Bang, "Note:

Optical fiber milled by focused ion beam and its application for Fabry-Perot refractive index sensor," Review Of Scientific Instruments **82**, 076103 (2011).

[118] G. F. Hu, and D. R. Chen, "Side-Hole Dual-Core Photonic Crystal Fiber for Hydrostatic Pressure Sensing," Journal Of Lightwave Technology **30**, 2382-2387 (2012).

[119] C. Wu, B. O. Guan, Z. Wang, and X. H. Feng, "Characterization of Pressure Response of Bragg Gratings in Grapefruit Microstructured Fibers," Journal Of Lightwave Technology **28**, 1392-1397 (2010).

[120] F. Guo, T. Fink, M. Han, L. Koester, J. Turner, and J. Huang, "High-sensitivity, high-frequency extrinsic Fabry–Perot interferometric fiber-tip sensor based on a thin silver diaphragm," Optics Letters **37**, 1505-1507 (2012).

[121] F. Xu, D. Ren, X. Shi, C. Li, W. Lu, L. Lu, L. Lu, and B. Yu, "High-sensitivity Fabry–Perot interferometric pressure sensor based on a nanothick silver diaphragm," Optics Letters **37**, 133-135 (2012).

[122] J. Ma, W. Jin, H. L. Ho, and J. Y. Dai, "High-sensitivity fiber-tip pressure sensor with graphene diaphragm," Optics Letters **37**, 2493-2495 (2012).

[123] Z. Y. Liu, M. L. V. Tse, C. Wu, D. R. Chen, C. Lu, and H. Y. Tam,

"Intermodal coupling of supermodes in a twin-core photonic crystal fiber and its application as a pressure sensor," Optics Express **20**, 21749-21757 (2012).

[124] T. Katsumata, Y. Haga, K. Minami, and M. Esashi, "Micromachined 125μm diameter ultra miniature fiber-optic pressure sensor for catheter," IEEJ Transactions on Sensors and Micromachines **120**, 58-63 (2000).

[125] D. C. Abeysinghe, S. Dasgupta, J. T. Boyd, and H. E. Jackson, "A novel MEMS pressure sensor fabricated on an optical fiber," IEEE Photonics Technology Letters **13**, 993-995 (2001).

[126] B. Liu, J. Lin, H. Liu, A. Jin, and P. Jin, "Extrinsic Fabry-Perot fiber acoustic pressure sensor based on large-area silver diaphragm," Microelectronic Engineering **166**, 50-54 (2016).

[127] K. Totsu, Y. Haga, and M. Esashi, "Ultra-miniature fiber-optic pressure sensor using white light interferometry," Journal Of Micromechanics and Microengineering **15**, 71-75 (2005).

[128] D. Donlagic, and E. Cibula, "All-fiber high-sensitivity pressure sensor with SiO2 diaphragm," Optics Letters **30**, 2071-2073 (2005).

[129] Y. Z. Zhu, and A. B. Wang, "Miniature fiber-optic pressure sensor," IEEE Photonics Technology Letters **17**, 447-449 (2005).

[130] U. Komaragiri, and M. R. Begley, "The mechanical response of freestanding circular elastic films under point and pressure loads," Journal Of Applied Mechanics-transactions Of The Asme **72**, 203-212 (2005).

[131] W. C. Young, and R. G. Budynas, *Roark's formulas for stress and strain* (McGraw-Hill New York, 2002).

[132] F. Chollet, "SU-8: Thick Photo-Resist for MEMS," (2013), http://memscyclopedia.org/su8.html, Accessed 15 Sep, 2017.

[133] MicroChem Corporation, "SU-8 Permanent Photoresists," (2011), http://www.microchem.com/pdf/SU-8-table-of-properties.pdf, Accessed Sep 16, 2017.

[134] Y. Z. Zhu, K. L. Cooper, G. R. Pickrell, and A. Wang, "High-temperature fiber-tip pressure sensor," Journal Of Lightwave Technology **24**, 861-869 (2006).

[135] J. W. Raich, and W. H. Schlesinger, "The global carbon dioxide flux in soil respiration and its relationship to vegetation and climate," Tellus Series B-chemical and Physical Meteorology **44**, 81-99 (1992).

[136] J. W. Raich, and C. S. Potter, "Global patterns of carbon dioxide emissions from soils," Global Biogeochemical Cycles **9**, 23-36 (1995).

[137] R. Andres, and T. Boden, "Global, regional, and national CO2

emissions," Trends 93: A Compendium of Data on Global Change, 505-584 (1994).

[138] S. Neethirajan, M. S. Freund, D. S. Jayas, C. Shafai, D. J. Thomson, and N. D. G. White, "Development of carbon dioxide (CO2) sensor for grain quality monitoring," Biosystems Engineering **106**, 395-404 (2010).

[139] S. Neethirajan, D. S. Jayas, and S. Sadistap, "Carbon Dioxide (CO2) Sensors for the Agri-food Industry—A Review," Food and Bioprocess Technology **2**, 115-121 (2008).

[140] P. Puligundla, J. Jung, and S. Ko, "Carbon dioxide sensors for intelligent food packaging applications," Food Control **25**, 328-333 (2012).

[141] Y. Liu, Y. H. Tang, N. N. Barashkov, I. S. Irgibaeva, J. W. Y. Lam, R. R. Hu, D. Birimzhanova, Y. Yu, and B. Z. Tang, "Fluorescent Chemosensor for Detection and Quantitation of Carbon Dioxide Gas," Journal Of The American Chemical Society **132**, 13951-13953 (2010).

[142] Z. Guo, N. R. Song, J. H. Moon, M. Kim, E. J. Jun, J. Choi, J. Y. Lee, C. W. Bielawski, J. L. Sessler, and J. Yoon, "A Benzobisimidazolium-Based Fluorescent and Colorimetric Chemosensor for CO2," Journal Of The American Chemical Society

134, 17846-17849 (2012).

[143] Q. Xu, S. Lee, Y. Cho, M. H. Kim, J. Bouffard, and J. Yoon, "Polydiacetylene-Based Colorimetric and Fluorescent Chemosensor for the Detection of Carbon Dioxide," Journal Of The American Chemical Society **135**, 17751-17754 (2013).

[144] D. J. Wales, J. Grand, V. P. Ting, R. D. Burke, K. J. Edler, C. R. Bowen, S. Mintova, and A. D. Burrows, "Gas sensing using porous materials for automotive applications," Chemical Society Reviews **44**, 4290-4321 (2015).

[145] K. Behera, S. Pandey, A. Kadyan, and S. Pandey, "Ionic Liquid-Based Optical and Electrochemical Carbon Dioxide Sensors," Sensors **15**, 29813 (2015).

[146] J. W. Severinghaus, and A. F. Bradley, "Electrodes for blood pO2 and pCO2 determination," Journal Of Applied Physiology **13**, 515-520 (1958).

[147] T. Ishihara, K. Kometani, M. Hashida, and Y. Takita, "Application of mixed oxide capacitor to the selective carbon dioxide sensor I. Measurement of carbon dioxide sensing characteristics," Journal Of The Electrochemical Society **138**, 173-176 (1991).

[148] D.-D. Lee, S.-D. Choi, and K.-W. Lee, "Carbon dioxide sensor

using NASICON prepared by the sol-gel method," Sensors and Actuators B: Chemical **25**, 607-609 (1995).

[149] G. G. Mandayo, F. González, I. Rivas, I. Ayerdi, and J. Herrán, "BaTiO3–CuO sputtered thin film for carbon dioxide detection," Sensors and Actuators B: Chemical **118**, 305-310 (2006).

[150] Q. Zhu, F. Qiu, Y. Quan, Y. Sun, S. Liu, and Z. Zou, "Solid-electrolyte NASICON thick film CO 2 sensor prepared on small-volume ceramic tube substrate," Materials Chemistry and Physics **91**, 338-342 (2005).

[151] C. Munkholm, D. R. Walt, and F. P. Milanovich, "A fiber-optic sensor for CO2 measurement," Talanta **35**, 109-112 (1988).

[152] H. Segawa, E. Ohnishi, Y. Arai, and K. Yoshida, "Sensitivity of fiber-optic carbon dioxide sensors utilizing indicator dye," Sensors and Actuators B: Chemical **94**, 276-281 (2003).

[153] J. Yuan, A. G. Márquez, J. Reinacher, C. Giordano, J. Janek, and M. Antonietti, "Nitrogen-doped carbon fibers and membranes by carbonization of electrospun poly (ionic liquid) s," Polymer Chemistry **2**, 1654-1657 (2011).

[154] J. Tang, H. Tang, W. Sun, H. Plancher, M. Radosz, and Y. Shen, "Poly(ionic liquid)s: a new material with enhanced and fast CO2

absorption," Chemical Communications, 3325-3327 (2005).

[155] J. Tang, H. Tang, W. Sun, M. Radosz, and Y. Shen, "Low-pressure CO2 sorption in ammonium-based poly(ionic liquid)s," Polymer **46**, 12460-12467 (2005).

[156] P. G. Mineo, L. Livoti, M. Giannetto, A. Gulino, S. Lo Schiavo, and P. Cardiano, "Very fast CO2 response and hydrophobic properties of novel poly(ionic liquid)s," Journal Of Materials Chemistry **19**, 8861 (2009).

[157] J. Yuan, and M. Antonietti, "Poly(ionic liquid)s: Polymers expanding classical property profiles," Polymer **52**, 1469-1482 (2011).

[158] W. Fang, Z. Luo, and J. Jiang, "CO2 capture in poly(ionic liquid) membranes: atomistic insight into the role of anions," Physical Chemistry Chemical Physics **15**, 651-658 (2013).

[159] J. Yuan, D. Mecerreyes, and M. Antonietti, "Poly(ionic liquid)s: An update," Progress In Polymer Science **38**, 1009-1036 (2013).

[160] G. Cojoc, C. Liberale, P. Candeloro, F. Gentile, G. Das, F. De Angelis, and E. Di Fabrizio, "Optical micro-structures fabricated on top of optical fibers by means of two-photon photopolymerization," Microelectronic Engineering **87**, 876-879 (2010).

[161] H. E. Williams, D. J. Freppon, S. M. Kuebler, R. C. Rumpf, and M.

A. Melino, "Fabrication of three-dimensional micro-photonic structures on the tip of optical fibers using SU-8," Optics Express **19**, 22910-22922 (2011).

[162] G. Kostovski, P. R. Stoddart, and A. Mitchell, "The Optical Fiber Tip: An Inherently Light‐Coupled Microscopic Platform for Micro‐ and Nanotechnologies," Advanced Materials **26**, 3798-3820 (2014).

[163] M. Vanek, J. Vanis, Y. Baravets, F. Todorov, J. Ctyroky, and P. Honzatko, "High-power fiber laser with a polarizing diffraction grating milled on the facet of an optical fiber," Optics Express **24**, 30225-30233 (2016).

[164] T. Gissibl, S. Thiele, A. Herkommer, and H. Giessen, "Sub-micrometre accurate free-form optics by three-dimensional printing on single-mode fibres," Nature Communications **7** (2016).

[165] J. Wu, X. Guo, A. P. Zhang, and H. Y. Tam, "Rapid 3D μ-printing of polymer optical whispering-gallery mode resonators," Optics Express **23**, 29708-29714 (2015).

[166] P. Morris, A. Hurrell, A. Shaw, E. Zhang, and P. Beard, "A Fabry-Perot fiber-optic ultrasonic hydrophone for the simultaneous measurement of temperature and acoustic pressure," Journal Of The Acoustical Society Of America **125**, 3611-3622 (2009).

[167] A. Sun, X. G. Qiao, Z. A. Jia, M. Li, and D. Z. Zhao, "Study of simultaneous measurement of temperature and pressure using double fiber Bragg gratings with polymer package," Optical Engineering **44** (2005).

[168] W. P. Chen, D. N. Wang, B. Xu, C. L. Zhao, and H. F. Chen, "Multimode fiber tip Fabry-Perot cavity for highly sensitive pressure measurement," Scientific Reports **7** (2017).

[169] C. Willa, J. Yuan, M. Niederberger, and D. Koziej, "When Nanoparticles Meet Poly(Ionic Liquid)s: Chemoresistive CO2 Sensing at Room Temperature," Advanced Functional Materials **25**, 2537-2542 (2015).

[170] J. L. Anthony, J. L. Anderson, E. J. Maginn, and J. F. Brennecke, "Anion effects on gas solubility in ionic liquids," Journal Of Physical Chemistry B **109**, 6366-6374 (2005).

[171] S. Supasitmongkol, and P. Styring, "High CO2 solubility in ionic liquids and a tetraalkylammonium-based poly(ionic liquid)," Energy & Environmental Science **3**, 1961-1972 (2010).

[172] T. C. Doan, J. Baggerman, R. Ramaneti, H. D. Tong, A. T. Marcelis, and C. J. van Rijn, "Carbon dioxide detection with polyethylenimine blended with polyelectrolytes," Sensors and Actuators B: Chemical **201**,

452-459 (2014).

[173] T. C. Doan, R. Ramaneti, J. Baggerman, J. F. van der Bent, A. T. Marcelis, H. D. Tong, and C. J. van Rijn, "Carbon dioxide sensing with sulfonated polyaniline," Sensors and Actuators B: Chemical **168**, 123-130 (2012).

[174] Y. Li, G. Li, X. Wang, Z. Zhu, H. Ma, T. Zhang, and J. Jin, "Poly(ionic liquid)-wrapped single-walled carbon nanotubes for sub-ppb detection of CO2," Chem Commun (Camb) **48**, 8222-8224 (2012).